Spring 2020

Measurement of the Photon Beam Asymmetry in $\gamma P \rightarrow K^{+}\Sigma^{0}$ at E_{γ} = 8.5 GeV with GlueX

Nilanga Indrajie Wickramaarachchi
Old Dominion University, nwick001@odu.edu

MEASUREMENT OF THE PHOTON BEAM ASYMMETRY IN $\gamma P \to K^+\Sigma^0$ AT $E_\gamma = 8.5$ GEV WITH GLUEX

by

Nilanga Indrajie Wickramaarachchi
M.S. May 2017, Old Dominion University

A Dissertation Submitted to the Faculty of
Old Dominion University in Partial Fulfillment of the
Requirements for the Degree of

DOCTOR OF PHILOSOPHY

PHYSICS

OLD DOMINION UNIVERSITY
May 2020

Approved by:

Moskov Amaryan (Director)

Anatoly Radyushkin (Member)

Stephen Bueltmann (Member)

Alexander Gurevich (Member)

Alvin Holder (Member)

ABSTRACT

MEASUREMENT OF THE PHOTON BEAM ASYMMETRY IN $\gamma P \to K^+\Sigma^0$ AT $E_\gamma = 8.5$ GEV WITH GLUEX

Nilanga Indrajie Wickramaarachchi
Old Dominion University, 2020
Director: Dr. Moskov Amaryan

In this work the photon beam asymmetry Σ for the reaction $\gamma p \to K^+\Sigma^0(1193)$ is measured using the GlueX experiment in Hall D at Jefferson Lab. The analysis used data that were collected using a linearly polarized photon beam in the energy range (8.2 - 8.8) GeV incident on a liquid hydrogen target. The beam asymmetries are measured as a function of the Mandelstam variable t and as a single value for the low u region. These are the first exclusive measurements of the photon beam asymmetry Σ in this reaction at energies above the baryon resonance region. For the t-channel, results are close to unity and show that the reaction is dominated by the natural-parity exchange of the $K^*(892)$ Regge trajectory as predicted by theoretical models. A value of $\Sigma = 0.410 \pm 0.090$ is obtained for the u-channel and suggests the exchange of both $\Sigma(J = 1/2)$ and $Y^*(J = 3/2)$ trajectory contributions to the production of $K^+\Sigma^0$.

ACKNOWLEDGMENTS

I would first like to express my gratitude to my supervisor Dr. Moskov Amaryan for giving me the opportunity to work on this analysis. I am thankful for his support and guidance throughout my graduate research. I would also like to thank Dr. Anatoly Radyushkin, Dr. Stephen Bueltmann, Dr. Alexander Gurevich and Dr. Alvin Holder for kindly agreeing to serve on my dissertation committee. I'm also grateful to Dr. Charles Hyde for the support he gave during this work as the Chair of the Physics Department at Old Dominion University.

I would like to specially thank everyone of the Hall D at Jefferson Lab including the group leader Eugene Chudakov for their extreme dedication during the experiment. I am grateful to the GlueX collaboration for all the comments made regarding the analysis and specially like to thank Mark Dalton, Alexander Austregesilo and Naomi Jarvis for their review which made many improvements to the analysis. I am also grateful to Dr. Justin Stevens and Simon Taylor for their suggestions and support throughout my research work. I would also like to thank Marouen Baalouch for giving me advice and guidance to be familiar with the analysis work when I was new to the research area.

I am very grateful to my parents, Wickramaarachchi Siriwardane and Leelawathie Meegahakotuwa for their support and love which helped me to focus on my research work. I am also thankful to my brother, Thilina Wickramaarachchi for his support during my time as a graduate student.

TABLE OF CONTENTS

Page

LIST OF TABLES

LIST OF FIGURES

CHAPTER 1

INTRODUCTION

The state $K^+\Sigma^0$ belongs to the so-called KY final states which have a kaon (a pseudoscalar meson) and a hyperon Y with one strange quark. Photoproduction is an interesting reaction to generate these states since there are no strange quarks initially in the system therefore a strange (s) anti-strange ($\bar{s}$) quark pair should be formed to conserve the strangeness. Polarization observables extracted using these reactions would be helpful to understand the production mechanisms dominating such processes. The work of this thesis is done using data from the GlueX experiment for photoproduction from a proton target: $\gamma p \to K^+\Sigma^0$.

The Σ^0 has a mean lifetime of $(7.4 \pm 0.7) \times 10^{-20}$ s and instantaneously decays to $\Lambda^0\gamma$. The branching fraction for this decay mode is 100%.

High statistics measurements of differential cross sections and polarization observables for the reaction $\gamma p \to K^+\Sigma^0$ have been done by collaborations like CLAS [1, 2], SAPHIR [3], GRAAL [4] and LEPS [5] at lower energies. A list of these measurements can be found in the SAID database [6]. The highest beam energy measurements for differential cross section and polarized-photon asymmetry for $\gamma p \to K^+(\Lambda, \Sigma^0)$ have been made by SLAC at 16 GeV [7] and the individual asymmetries for $K^+\Lambda$ and $K^+\Sigma^0$ have been only determined based on cross section measurements.

Figure 1 shows Feynman diagrams for the different channels that can contribute to the reaction $\gamma p \to K^+\Sigma^0$. The s, t and u-Mandelstam variables for the reaction are defined as:

$$s = (p_\gamma + p_T)^2, \tag{1}$$

$$t = (p_\gamma - p_K)^2, \tag{2}$$

$$u = (p_T - p_K)^2, \tag{3}$$

where p_γ, p_T and p_K are four-momenta of the incoming photon beam, the target proton and the produced K^+ meson respectively. For the lower photon beam energies, s-channel contribution is expected to dominate the production mechanism where the proton gets excited in the intermediate state. At higher energies above the resonance region (≥ 4 GeV) the t- and u-channel exchanges contribute to the production with the exchange of K^+ or K^{*+} for the

t-channel and baryons like Λ, Σ and Y^* for the u-channel respectively. In the case where the incoming photon beam is polarized, the study of beam asymmetry allows us to determine which type of exchange is happening during the reaction.

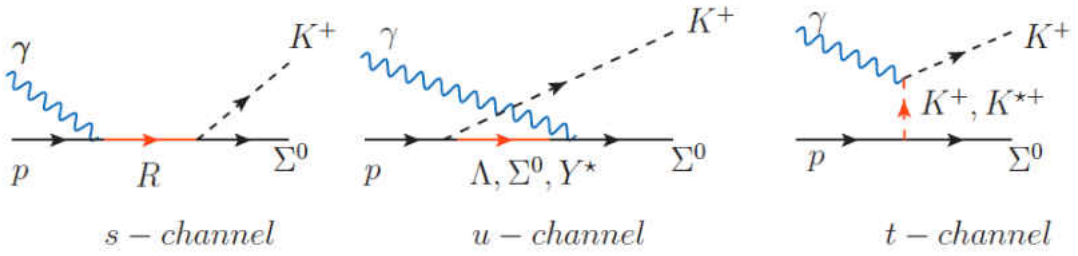

FIG. 1: Different channels contributing to the reaction $\gamma p \to K^+\Sigma^0$.

1.1 STRUCTURE OF THE THESIS

The structure of the thesis is organized as follows. Chapter 2 gives an overview of the theory. Starting with the standard model and then the quark model, a brief description is given about Regge theory and helicity amplitudes.

An overview of the detector components used in the GlueX experiment is presented in Chapter 3.

The data analysis primarily focusing on the event selection and the MC simulation is described in Chapter 4.

Chapters 5 and 6 explain how the beam asymmetry has been extracted and outlines studies to estimate different sources of systematic uncertainties.

Chapter 7 is devoted to comparison of experimental data with the model predictions and explains physics conclusions obtained from this comparison.

CHAPTER 2

THEORY

2.1 THE STANDARD MODEL

In the standard model, the fundamental particles of matter are divided into two categories. They are fermions that have half-integer spin and bosons with integer spins. Fermions obey Fermi-Dirac statistics while bosons obey Bose-Einstein statistics. The interactions between particles are considered to come through four fundamental forces: the strong, the electromagnetic, the weak and the gravitational force. Although the gravity is the much easier force to be observed in the world, in the high-energy physics, it is considered to be negligible.

Fermions are further divided into two types: quarks and leptons which have spin 1/2. Quarks carry fractional electric charge and six types of them are observed: up (u), down (d), charm (c), strange (s), top (t) and bottom (b). These are known as quarks of different flavors. Similarly there are six types of leptons: electron (e^-), muon (μ^-), tau (τ^-) and their corresponding neutrinos (ν_e, ν_μ and ν_τ). Neutrinos don't have electric charge. Furthermore each quark and lepton has its anti-particle which has opposite electric charge and the same mass. Figure 2 shows the fundamental particles of the standard model.

Quarks can not be observed as individual free states. They combine to form hadrons which can be either mesons or baryons depending on how the quarks and (or) anti-quarks are combined. A quark anti-quark pair forms a meson which in turn has spin 0 or 1 making them bosons. A baryon is a combination of three valence quarks (qqq). The proton (uud) and neutron (ddu) are examples of baryons. Baryons have half-integer spins and therefore are fermions. One of the important feature about quarks is that only they can carry the color charge, the Quantum Chromo Dynamics (QCD) equivalent of the electric charge. Because of this, only quarks are involved in the strong interactions. Hadrons are formed as color-neutral states. For this criteria to be satisfied anti-quarks are assumed to have anti-colors.

Leptons can interact via electromagnetic or weak forces depending on whether they are charged or not. Neutrinos are mainly found in radioactive decays like β decay of atomic nuclei or hadrons.

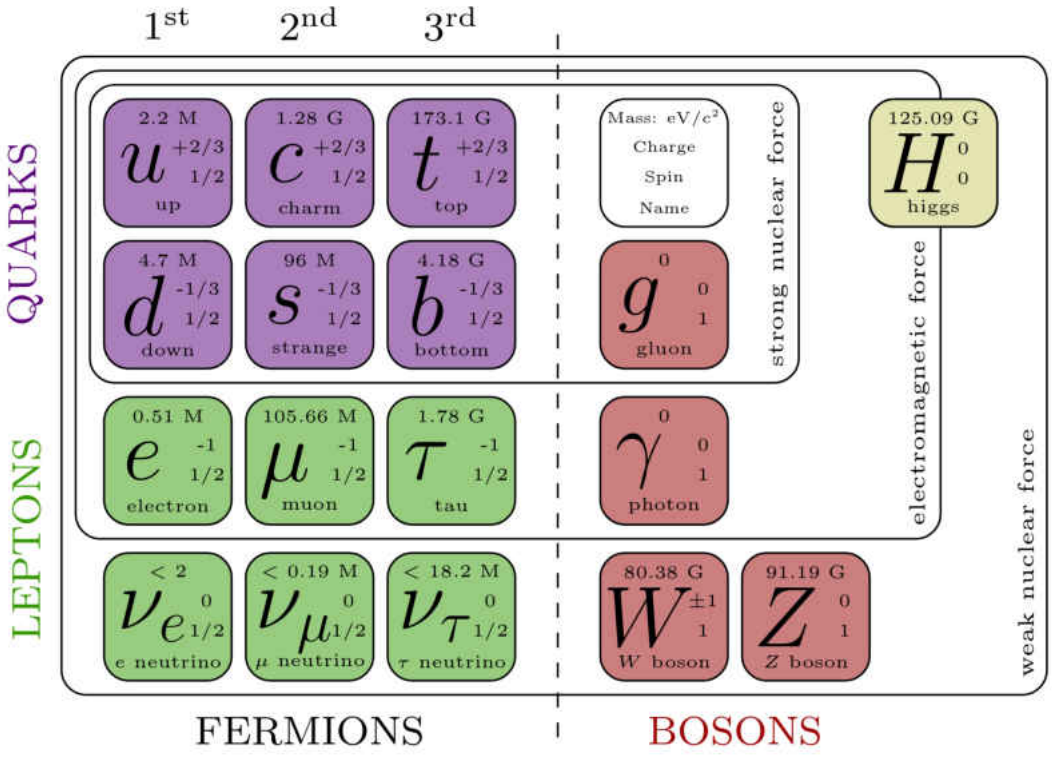

FIG. 2: Fundamental particles in the Standard Model. Quarks and leptons are arranged as columns corresponding to their generations.

Quarks and leptons are further classified as three generations. The u- and d-quarks and the electron and electron-neutrino are considered as the first generation. The c- and s-quarks and μ and ν_μ form the second generation while the t- and b-quarks and τ and ν_τ form the third generation. When going from lower to higher generation, particle masses increase by orders of magnitude. Because of their lower masses, hadrons made out from u, d and s quarks are the ones that are extensively studied in experiments.

The four forces are considered to occur through exchange of particles called gauge-bosons between the interacting fermions. These mediators of forces have spin 1 so making them types of bosons. Each force can be described by an associated Quantum Field Theory (QFT). Quantum Electrodynamics (QED) explains the electromagnetic force between two charged particles via the exchange of a virtual photon. In the QCD, force between two quarks is described to occur through the exchange of a gluon. Both photon and gluon are massless. Contrary to these gauge bosons, the weak force is exchanged by massive W and

Z bosons. Weak charged-current interaction is mediated by the W^+ and W^- bosons while the weak neutral-current interaction is mediated by the neutral Z boson. Weak interactions are unique in a sense that they can change the flavor of a quark from one to another. For example, a neutron can decay to a proton by the β^- decay and a down quark in the neutron changes to an up quark with the emission of a W^- boson. The electroweak theory unifies electromagnetic and weak interactions.

Additionally there is a scalar boson (boson with spin 0) called Higgs boson which is considered to give masses to the particles that interacts with the so-called Higgs field. The Higgs boson was discovered by the ATLAS and CMS experiments at the Large Hadron Collider (LHC) in 2012. It has a mass of approximately 125 GeV.

2.2 THE QUARK MODEL

The quark model is based on the work by Murray Gell-Mann [8, 9], Yuval Ne'eman [10] and George Zweig [11]. It's a classification scheme where hadrons are made out of quarks and (or) antiquarks.

In quantum mechanics, for each symmetry of the Hamiltonian, we can find a conserved observable quantity. Mathematically, this deals with a unitary operator $\hat{U}$ which commutes with the Hamiltonian, i.e. $[\hat{H},\hat{U}] = 0$. This unitary operator can be associated with a Hermitian generator $\hat{G}$ which also commutes with the Hamiltonian and has real eigenvalues. This can be used to model hadrons with a symmetry group consideration.

It was proposed by Heisenberg that the nuclear force is approximately charge independent and neutron and proton can be considered as two states of the nucleon. The concept of isospin was introduced and the proton and neutron were assumed to have a total isospin $I = 1/2$ and third component of isospin $I_3 = 1/2$ and $I_3 = -1/2$ respectively. Similar to the spin-states of an electron this can be written as,

$$p = \begin{pmatrix} 1 \\ 0 \end{pmatrix} \quad n = \begin{pmatrix} 0 \\ 1 \end{pmatrix} \tag{4}$$

Assuming up, down quark masses to be same, the strong interaction can be incorporated with a u,d flavor symmetry. Following the way proton and neutron was written in isospin

space, then the u and d quarks are written as states in flavor space,

$$u = \begin{pmatrix} 1 \\ 0 \end{pmatrix} \quad d = \begin{pmatrix} 0 \\ 1 \end{pmatrix} \tag{5}$$

In group theory terms, this allows to find the generators of the unitary operator which makes the QCD interaction to be invariant under transformation in u,d flavor space as,

$$\hat{U} = exp(i\alpha_i \hat{G}_i) \tag{6}$$

where α_i is an infinitesimal transformation. Three of the generators form a special unitary SU(2) group and the Pauli spin-matrices given below are chosen that gives conserved observables.

$$\sigma_1 = \begin{pmatrix} 0 & 1 \\ 1 & 0 \end{pmatrix} \quad \sigma_2 = \begin{pmatrix} 0 & -i \\ i & 0 \end{pmatrix} \quad \sigma_3 = \begin{pmatrix} 1 & 0 \\ 0 & -1 \end{pmatrix} \tag{7}$$

The isospin components can be written using Pauli matrices as,

$$\hat{T}_i = \frac{1}{2}\hat{\sigma}_i \tag{8}$$

The total isospin is defined as $\hat{T^2} = \hat{T_1^2} + \hat{T_2^2} + \hat{T_3^2}$ and commutes with each of the isospin component. This allows to write u and d quarks as states $\phi(I, I_3)$ since the eigenvalue equation is given by,

$$\hat{T^2}\phi(I, I_3) = I(I+1)\phi(I, I_3) \tag{9}$$

The up and down quarks are written in terms of isospin as,

$$u = \begin{pmatrix} 1 \\ 0 \end{pmatrix} = \phi\Big(\frac{1}{2}, +\frac{1}{2}\Big) \quad \text{and } d = \begin{pmatrix} 0 \\ 1 \end{pmatrix} = \phi\Big(\frac{1}{2}, -\frac{1}{2}\Big) \tag{10}$$

Then, combinations of two quark states can be formed by u and d quarks considering the rules of adding I and I_3. Adding another u or d quark allows to make 8 possible combinations *uuu*, *uud*, *udu*, *udd*, *duu*, *dud*, *ddu* and *ddd*. The flavor wavefunctions of these states can be found using isospin arguments and isospin ladder operators for u and d quarks. This

gives a $I = \frac{3}{2}$ quadruplet and two $I = \frac{1}{2}$ doublets. This can be written using SU(2) group representation as,

$$2 \otimes 2 \otimes 2 = 4 \oplus 2 \oplus 2 \tag{11}$$

with the three quark combinations are represented as isospin doublets. Similarly, spin wavefunctions can be constructed for three quarks and will have the same form since isospin and spin are analogous. The total wavefunction of three quark bound state has extra terms for color and spatial wavefunctions, but it can be found that the product of flavor and spin wavefunctions should be symmetric for the case with zero orbital angular momentum, i.e. $L = 0$. This comes from the fact that the total wavefunction should be antisymmetric under interchange of any two quarks.

The up and down antiquarks ($\bar{u}$ and $\bar{d}$) are written as a doublet in the following way so that they transform the same way as the quarks. This gives two SU(2) doublets for quarks and antiquarks as,

$$q = \begin{pmatrix} u \\ d \end{pmatrix} \quad \bar{q} = \begin{pmatrix} -\bar{d} \\ \bar{u} \end{pmatrix} \tag{12}$$

Using this isospin representation, four states of mesons can be formed by up and down quarks and antiquarks. Written as states of $\phi(I, I_3)$ they are, [12]

$$\begin{aligned} \phi(1,-1) &= d\bar{u} \\ \phi(1,0) &= \frac{1}{\sqrt{2}}(u\bar{u} - d\bar{d}) \\ \phi(1,+1) &= -u\bar{d} \\ \phi(0,0) &= \frac{1}{\sqrt{2}}(u\bar{u} + d\bar{d}) \end{aligned} \tag{13}$$

So, this gives an isospin-1 triplet and an isospin-0 singlet and represented as,

$$2 \otimes \bar{2} = 3 \oplus 1 \tag{14}$$

Extending this procedure to include the s quark, an SU(3) representation can be developed to associate a uds flavor symmetry of the Hamiltonian. This is only approximate, as the strange quark mass is much higher than masses of u, d quarks but this difference is small compared to binding energies of hadrons. The u,d and s quarks are reprented in SU(3)

reprentation as,

$$u = \begin{pmatrix} 1 \\ 0 \\ 0 \end{pmatrix} \quad d = \begin{pmatrix} 0 \\ 1 \\ 0 \end{pmatrix} \quad s = \begin{pmatrix} 0 \\ 0 \\ 1 \end{pmatrix} \tag{15}$$

There are eight generators in SU(3) symmetry called Gell-Mann matrices defined as,

$$\hat{T}_i = \frac{1}{2}\lambda_i \tag{16}$$

Only two of them ($\hat{T}_3$ and $\hat{T}_8$) commute. Therefore, in SU(3), hadrons are descibed in terms of the third component of isospin (I_3) and hypercharge (Y) with operators,

$$\hat{T}_3 = \frac{1}{2}\lambda_3 \ , \ \hat{Y} = \frac{1}{\sqrt{3}}\lambda_8 \tag{17}$$

Similar to the case of SU(2), the addition of I_3 and Y components of quarks leads to formation of hadrons. The corresponding ladder operators are used to determine the flavor wavefunctions. A quark (u,d or s) and an antiquark is combined to give nine possible combinations which are decomposed into an octet and a singlet as,

$$3 \otimes \bar{3} = 8 \oplus 1 \tag{18}$$

The singlet state is a linear combination of $u\bar{u}$, $d\bar{d}$ and $s\bar{s}$ and its flavor wavefunction is written as,

$$\psi_s = \frac{1}{\sqrt{3}}(u\bar{u} + d\bar{d} + s\bar{s}) \tag{19}$$

A hadron state is usually represented by its quantum numbers as J^{PC}. Here, $J = L + S$ is the total angular momentum found by adding orbital and spin angular momenta quantum numbers. P and C are called parity and charge conjugation and they can be found by $P = (-1)^{L+1}$ and $C = (-1)^{L+S}$ respectively. The $L = 0$ meson states are the simplest case and are called light mesons. Since the $q\bar{q}$ pair can give spin $S = 0$ or $S = 1$, this gives a nonet with $J = 0$ pseudoscalar mesons and another nonet with $J = 1$ vector mesons. They have parities of -1. Figures 3 and 4 show the corresponding mesons and Table 1 represents the J^{PC} assignments for mesons with $L < 2$.

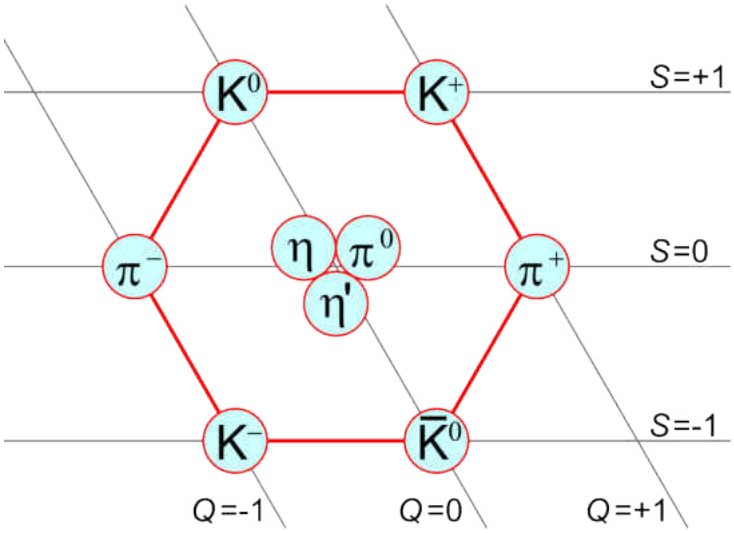

FIG. 3: Nonet of pseudoscalar mesons. S and Q indicate the strangeness and the electric charge of the mesons.

The combination of three quarks gives total of 27 flavor states in SU(3) representation. These baryons are decomposed to a symmetric decuplet, two mixed symmetry octets and an antisymmetric singlet state as,

$$3 \otimes 3 \otimes 3 = 10 \oplus 8 \oplus 8 \oplus 1 \tag{20}$$

Figures 5 and 6 show the observed octet and decuplet of $L = 0$ light baryons.

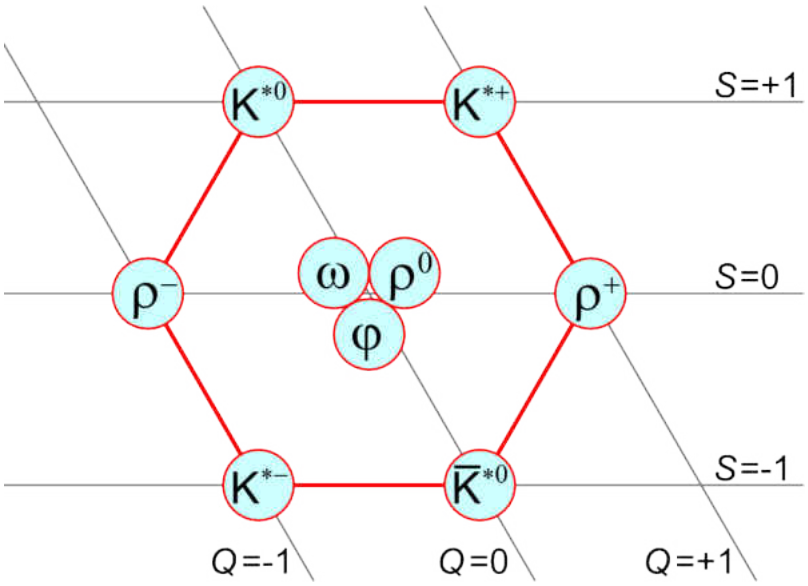

FIG. 4: Nonet of vector mesons. S and Q indicate the strangeness and the electric charge of the mesons.

L	S	J	P	C	J^{PC}	Type	Examples
0	0	0	-	+	0^{-+}	Pseudoscalar	π, η, η', K
0	1	1	-	-	1^{--}	Vector	ρ, ω, ϕ, K^*
1	0	1	+	-	1^{+-}	Pseudovector	b_1, h_1, h_1', K_1
1	1	0	+	+	0^{++}	Scalar	a_0, f_0, f_0', K_0^*
1	1	1	+	+	1^{++}	Axial Vector	a_1, f_1, f_1', K_1
1	1	2	+	+	2^{++}	Tensor	a_2, f_2, f_2', K_2^*

TABLE 1: J^{PC} assignments for mesons.

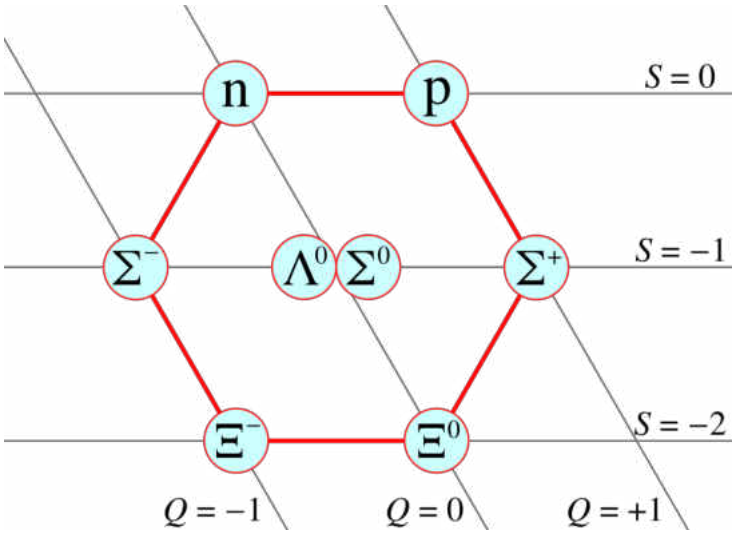

FIG. 5: Observed octet of baryons. S and Q indicate the strangeness and the electric charge of the baryons.

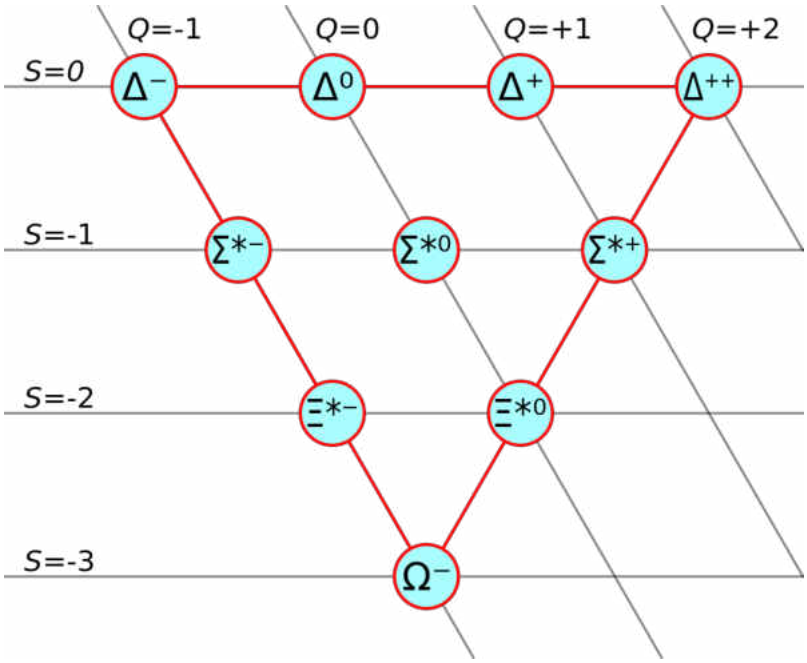

FIG. 6: Observed decuplet of baryons. S and Q indicate the strangeness and the electric charge of the baryons.

2.3 THE REGGE MODEL

In the Regge model the scattering amplitude of a two particle collision is written as a function of a complex angular momentum variable. It was proposed as an alternative approach to the quantum mechanical treatment of potential scattering. At high energies the poles of the scattering amplitude correspond to the exchange of the Regge trajectories. A Regge trajectory consists of a family of resonances with identical internal quantum numbers but different total angular momenta J. Members of such a family are related approximately by the linear relation $J_i = \alpha(m_i^2)$ between their total angular momenta and squared masses [13]. Regge trajectories for $K(494)$ and $K^*(892)$ families and Λ,Σ and $\Sigma^\star$ families are shown in Figs. 7 and 8 respectively.

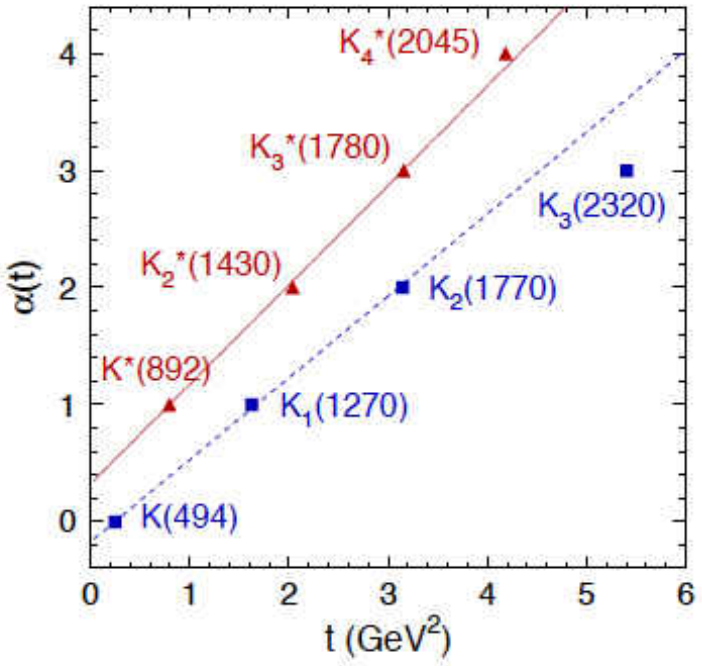

FIG. 7: Chew-Frautschi plots for the $K(494)$ and $K^*(892)$ trajectories [14].

The amplitude for $\gamma p \to KY$ reaction is written considering the exchange of entire Regge trajectories rather than a finite selection of individual particles. For the forward scattering angles, K^* trajectories are exchanged in the t-channel while Y^* trajectories are exchanged in the u-channel for backward scattering angles.

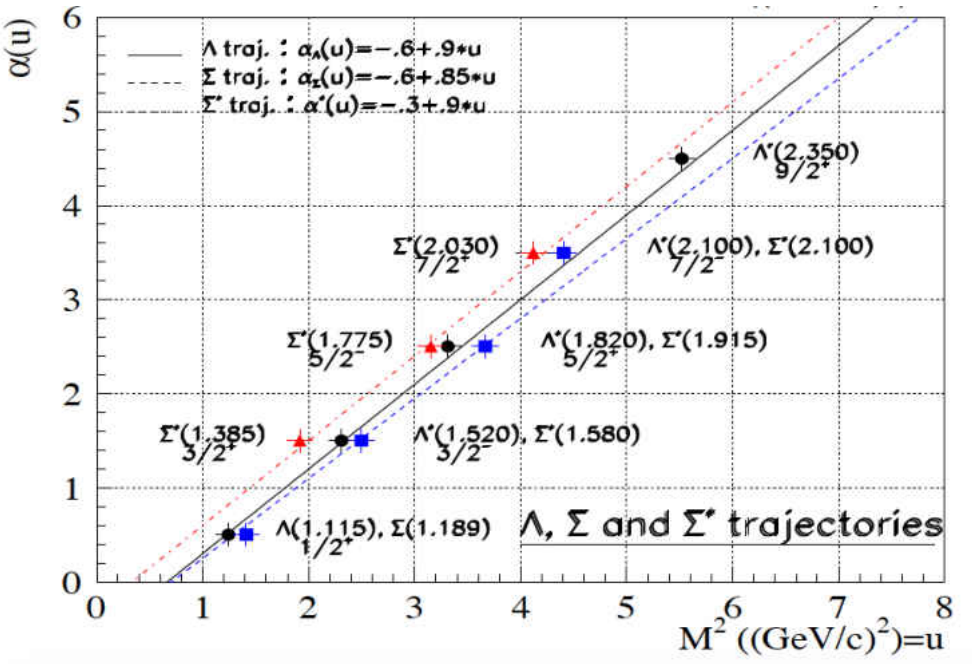

FIG. 8: Chew-Frautschi plots for the Λ,Σ and $\Sigma^\star$ trajectories [15].

A linear meson trajectory has the following form,

$$\alpha_X(t) = \alpha_{X,0} + \alpha'_X(t - m_X^2) \tag{21}$$

where m_X and $\alpha_{X,0}$ are the mass and spin of the lightest member in the trajectory. The slope of the trajectory is given by α'_X.

The amplitude can then be written by replacing the Feynman propagator with the Regge propagator:

$$\frac{1}{t - m_X^2} \to \mathcal{P}^X_{Regge}[s, \alpha_X(t)]. \tag{22}$$

Then the Regge amplitude is presented as

$$\mathcal{M}^X_{Regge}(s,t) = \mathcal{P}^X_{Regge}[s, \alpha_X(t)] \times \beta_X(s,t), \tag{23}$$

where $\beta_X(s,t)$ is the residue of the original Feynman amplitude calculated from the interaction Lagrangians at the γKX and pXY vertices in the reaction $p(\gamma, K)Y$ with X exchange particle.

Following this method, the general Regge propagator can be formed as shown in the Ref. [14].

$$P^X_{Regge}(s,t) = \frac{(\frac{s}{s_0})^{\alpha_X(t)-\alpha_{X,0}}}{\sin(\pi\alpha_X(t))} \left\{ \begin{matrix} 1 \\ e^{-i\pi\alpha_X(t)} \end{matrix} \right\} \frac{\pi\alpha'_X}{\Gamma(1+\alpha_X(t)-\alpha_{X,0})} \tag{24}$$

where s_0 is a scale factor fixed at 1 GeV^2.

For fixed s, $|P^X_{Regge}(s,t=0)|$ increases with decreasing $|\alpha_X(0)-\alpha_{X,0}| = \alpha'_X m_X^2$. Slopes α'_X for all meson trajectories are nearly the same, therefore trajectories with lowest mass first member of the corresponding family are expected to dominate the exchange. Because of this, for the $\gamma p \to KY$ channel, $K(494)$ and $K^*(892)$ exchanges dominate.

2.4 RPR MODEL

In this model, a contribution from the resonance region is added to the Regge part of the amplitude to generate the "Regge-Plus-Resonance" model. Figure 9 shows the RPR amplitude for $\gamma p \to KY$ process in the forward-angle region. According to this the kaon trajectories are exchanged in the t-channel and individual baryon resonances are also contributing in the s-channel. For photon energies greater than about 4 GeV, the s-channel contributions vanish by construction and only the Regge part of the amplitude is considered.

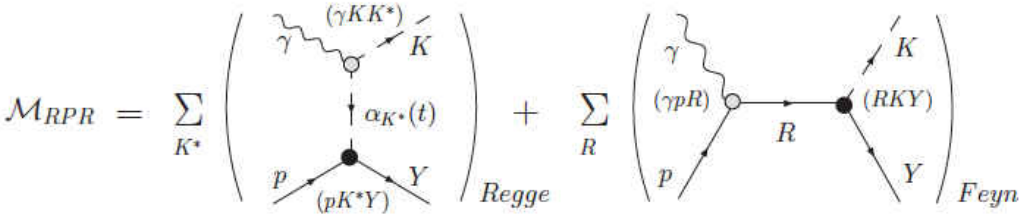

FIG. 9: General forward-angle RPR amplitude for the $\gamma p \to KY$ process [14].

Using Eqn. 24, Regge propagators for $K(494)$ and $K^*(892)$ exchange can be written. When the interaction Lagrangian for $\gamma p \to K^+\Sigma^0$ process is used, the high energy amplitude contains only three parameters related to the coupling constants

$$g_{K^+\Sigma^0 p}\,, G^{v,t}_{K^{*+}(892)} = \frac{e g^{v,t}_{K^{*+}(892)\Sigma^0 p}}{4\pi}\,\kappa_{K^+K^{*+}(892)}. \tag{25}$$

Here, $g^{v,t}_{K^{*+}(892)\Sigma^0 p}$ are the strong vector and tensor couplings to the $K^{*+}(892)$ vector meson trajectory. Additionally, the phase of the trajectory is chosen to be constant or rotating. These parameters are used in the RPR model to predict the values for polarization observables, in particular the t-dependence of beam asymmetry.

2.5 HELICITY AMPLITUDES

The helicity of a particle is defined as the projection of its spin $\vec{s}$ along the direction of linear momentum $\vec{p}$:

$$H = \frac{\vec{s}\cdot\vec{p}}{|\vec{s}\cdot\vec{p}|} \tag{26}$$

Depending on whether the spin and momentum vectors are aligned in the same direction or in opposite directions, the helicity can be positive or negative respectively.

The photoproduction amplitude can be written in terms of functions which are related to the helicities of incoming and outgoing particles. These functions are called "helicity amplitudes" and provide information about the exchange mechanisms during the process. For a photoproduction of a spin zero meson and a nucleon, these have the amplitude written in general form f_{abcd} where a,b,c and d are the helicities of the incoming photon, target proton, produced spin zero meson and the nucleon.

In 1964, P. Stichel developed a theorem relating the photoproduction amplitude for $\gamma + N \to \pi + N$ channel and the parity of the exchange particle π_j [16]. In brief, the theory goes as follows.

Let $\vec{k}$ and $\vec{q}$ be the momenta of the incoming photon and the outgoing pion in the center of mass system for the process $\gamma + N \to \pi + N$. In the Coloumb gauge we have the transversality condition $\vec{\epsilon}\cdot\vec{k} = 0$ where $\vec{\epsilon}$ is the polarization vector of the photon. Then the differential cross section maybe written as [17]:

$$\frac{d\sigma}{d\Omega} = \frac{q}{k}|X_f\ F\ X_i|^2\,, \tag{27}$$

where the photoproduction amplitude F is a 2×2 matrix in spin space and X_i and X_f are the Pauli spinors for the initial and final nucleon spin states. The general form of F is written as:

$$F = i\ \sin\ \phi\ [C_1\ (\vec{\sigma}\cdot\hat{k}) + C_2\ (\vec{\sigma}\cdot\hat{n}\times\hat{k})] + \cos\ \phi\ [C_3 + i\ (\vec{\sigma}\cdot\hat{n})\ C_4]\,, \tag{28}$$

where ϕ is an angle which describes the orientation of $\vec{\epsilon}$ in a plane orthogonal to $\hat{k}$:

$$\vec{\epsilon} = -\cos\ \phi\ \hat{n} + \sin\ \phi\ (\hat{n}\times\hat{k}) \tag{29}$$

with $\hat{n} \equiv \hat{k} \times \hat{q}$. The $\vec{\sigma}$ are the Pauli spin matrices and the C_i are functions of Mandelstam variables s and t.

When summed over the nucleon spin states, Eqn. 27 gives,

$$\frac{\overline{d\sigma}}{d\Omega} = \frac{q}{k}[\sin^2\phi\ (|C_1|^2 + |C_2|^2) + \cos^2\phi\ (|C_3|^2 + |C_4|^2)] \tag{30}$$

The Stichel theorem says,

"Provided that to the amplitude $F(\phi)$ for $\gamma + N \to \pi + N$ only exchange of particles or particle-systems with total angular momenta j and either parity $\pi_j = (-1)^{j+1}$ or $\pi_j = (-1)^j$ in the crossed channel $\gamma + \pi \to N + \bar{N}$ contributes, then the ϕ-dependence of $F(\phi)$ at high energies s and small momentum transfer t becomes:

a) $F(\phi) \sim \sin\phi$ for $\pi_j = (-1)^{j+1}$ resp.

b) $F(\phi) \sim \cos\phi$ for $\pi_j = (-1)^j$ " [16].

The theorem has been proved by writing functions C_i in terms of helicity amplitudes and considering which amplitudes are non-vanishing for the cases $\pi_j = (-1)^{j+1}$ (unnatural parity) and $\pi_j = (-1)^j$ (natural parity). The theorem can be extended to complex angular momenta in the case that π_j denotes a Regge trajectory exchanged in the t-channel.

Stichel theorem can also be used for the reaction $\gamma p \to K^+\Sigma^0$ and in Ref. [18] a relation between the photon beam asymmetry Σ and exchanged parity is given. There a set of s-channel helicity amplitudes with definite parity in the t-channel are defined to leading order in s as:

$$\begin{aligned} f_1 &= f_{1+,0+}, \\ f_2 &= f_{1+,0-}, \\ f_3 &= f_{1-,0+}, \\ f_4 &= f_{1-,0-}, \end{aligned} \tag{31}$$

Then the following combinations can be formed:

$$\begin{aligned} f_1^{\pm} &= \frac{1}{2}(f_1 \pm f_4), \\ f_2^{\pm} &= \frac{1}{2}(f_2 \mp f_3), \end{aligned} \tag{32}$$

where the superscript $+(-)$ indicates natural (unnatural) parity exchange in the t-channel.

The polarized photon asymmetry is given by

$$\begin{aligned} \Sigma &= \left[\frac{d\sigma_\perp}{dt} - \frac{d\sigma_\parallel}{dt}\right] \Big/ \left[\frac{d\sigma_\perp}{dt} + \frac{d\sigma_\parallel}{dt}\right] \\ &= \frac{(|f_1^+|^2 + |f_2^+|^2 - |f_1^-|^2 - |f_2^-|^2)}{(|f_1^+|^2 + |f_2^+|^2 + |f_1^-|^2 + |f_2^-|^2)}, \end{aligned} \tag{33}$$

where $\frac{d\sigma_\perp}{dt}$ ($\frac{d\sigma_\parallel}{dt}$) is for the cross section with a photon beam polarized perpendicular (parallel) to the reaction plane.

Using a linearly polarized photon beam allows us to study about the type of parity exchanged in the t-channel. Since beam asymmetry Σ is a measure of the difference between contributions from perpendicular and parallel polarized photons to the cross section, it can be used to distinguish the relative contribution of natural and unnatural parity exchange.

CHAPTER 3

GLUEX SPECTROMETER

The GlueX spectrometer is located in Hall D at the Thomas Jefferson National Accelerator Facility (JLab) in Newport News, Virginia. The Continuous Electron Beam Accelerator Facility (CEBAF) (shown in Fig. 10) in JLab provides a continuous wave 12 GeV electron beam to Hall D. A high frequency laser is used in the CEBAF to produce electrons. The laser is incident on a GaAs photocathode and produce a highly polarized electron beam. The electron bursts are distributed as evenly spaced beam bunches (pulses) and accelerated by superconducting radiofrequency (RF) cavities before reaching the experimental halls [19]. The Nb RF cavities produce standing electromagnetic waves which are matched with the phase and frequency of the electron bunch. The cavities are designed with an accelerating frequency of 1497 MHz. The electron beam produced should match this frequency but to operate four halls simultaneously four lower frequency lasers are used providing 4 distinct electron beams to the halls A, B, C and D. The electron beams are accelerated due to the gradient from the standing waves in the cavities and run through the accelerating sections in the CEBAF up to five passes. Each pass provides energy of 2.2 GeV to the electron beam. Halls A, B and C receives the electron beam after 1-5 passes through the accelerator. A 249.5 MHz electron beam is delivered to Hall D and arrives the hall after 5.5 passes through the accelerator. This gives the potential to have a 12 GeV electron beam delivered to the Hall D and in turn allows to be used for many physics interests.

The electron beam hits a diamond radiator and produces a linearly polarized photon beam. The photon beam then reaches a liquid hydrogen target and produces many particles and showers after the interaction. The GlueX detector is a nearly 4π hermetic detector and allows to identify all the particles in the final state of the reaction. The GlueX spectrometer consists of many detector components as shown in Fig. 11 and each of the major components are briefly described in this chapter.

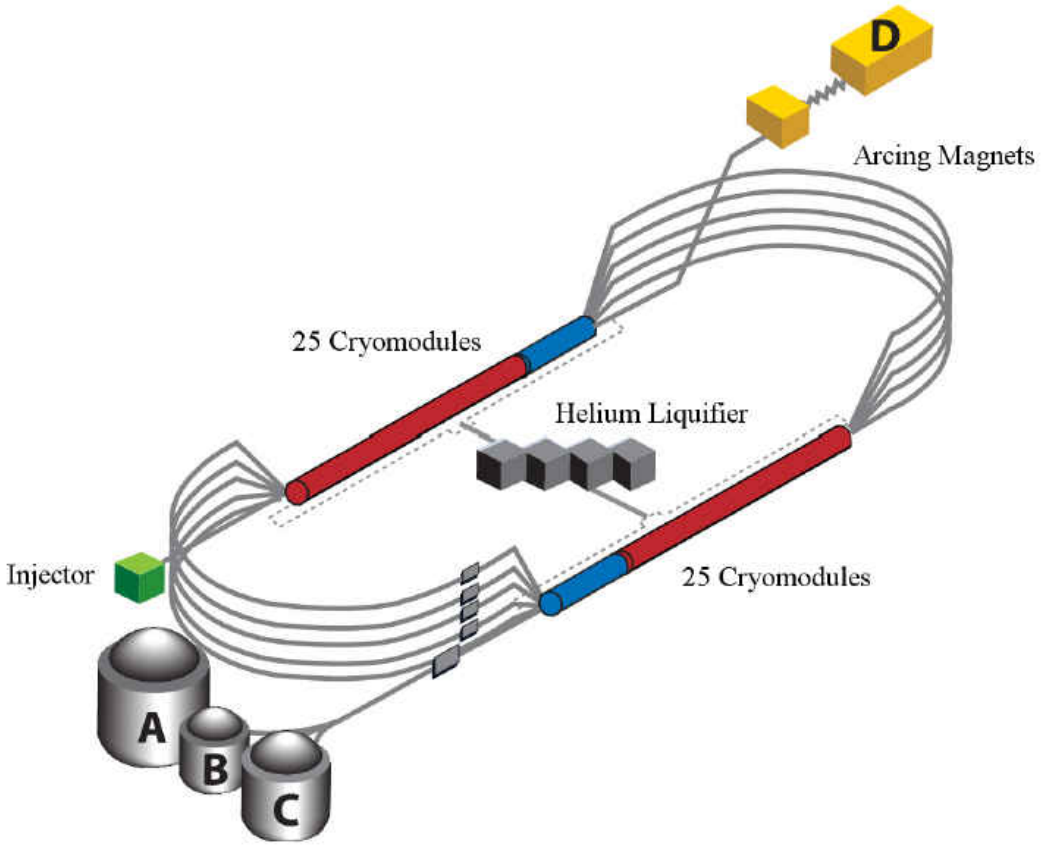

FIG. 10: CEBAF at the Jefferson Lab. Figure from Ref. [20].

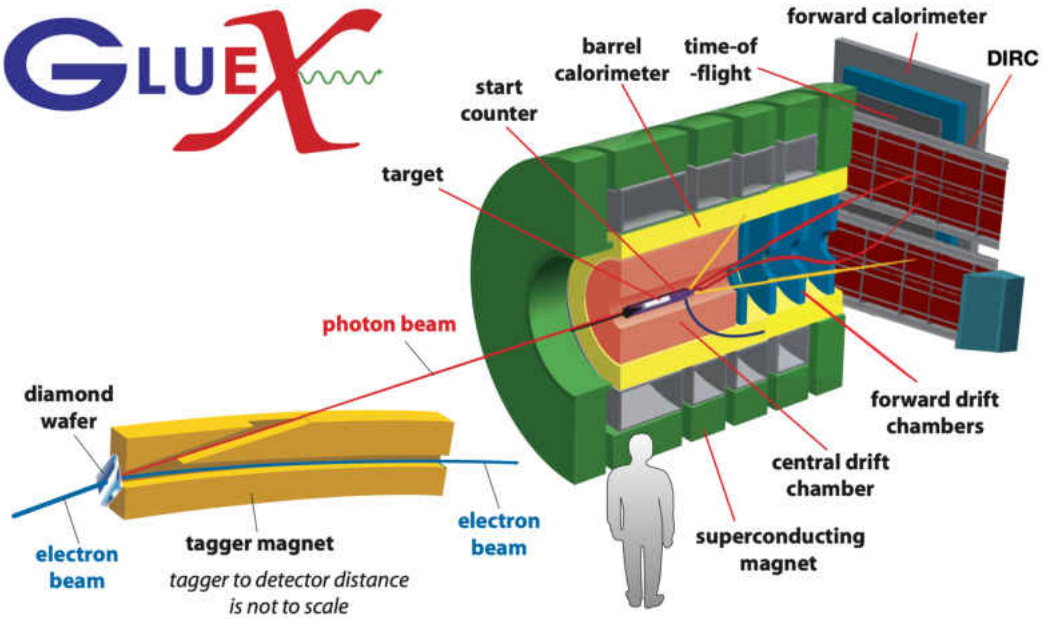

FIG. 11: The GlueX spectrometer.

3.1 BEAMLINE

The GlueX beamline consists of components that are used to create a linearly polarized photon beam and to measure the energy, polarization and the flux of the photon beam. The main components of the beamline are shown in Fig. 12.

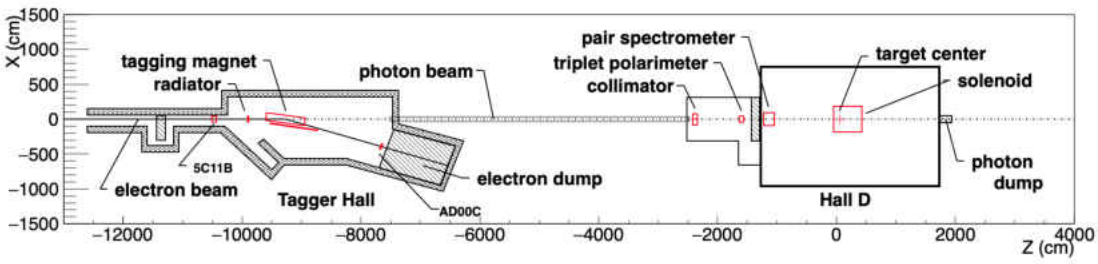

FIG. 12: Schematic of the GlueX beamline components and the spectrometer. Figure from Ref. [21].

3.1.1 DIAMOND RADIATOR

The 12 GeV electron beam from CEBAF enters the Tagger Hall that houses the radiator and the photon tagging system. The electron beam is incident on a thin (58 μm) diamond wafer and produces a photon beam. The photon beam is created using the coherent Bremsstrahlung technique [22, 23]. The electron beam transfers momentum to a struck nucleus in the diamond radiator and forms a continuum of momentum transfer and the momentum values are averaged to give the incoherent component of the Bremsstrahlung process. The coherent component is obtained by allowing the momentum transfer to match with the reciprocal lattice vectors of the diamond. A goniometer device is used to hold the diamond radiator in order to align it precisely to achieve the desired coherent photon beam spectrum. The coherent spectra occurs at certain energy ranges of the photon beam but the nominal GlueX configuration uses the main coherent peak set around 9 GeV.

3.1.2 PHOTON TAGGING SYSTEM

The GlueX photon tagging system primarily consists of dipole magnets and two scintillation detectors called Tagger Hodoscope (TAGH) and Tagger Microscope (TAGM). The energy of the photon (E_γ) is "tagged" by measuring the energy of the scattered electron (E_e) from the diamond radiator and using the precisely known incoming electron beam energy (E_0). It can be written as $E_\gamma = E_0 - E_e$. Figure 13 shows a schematic of the photon tagging system.

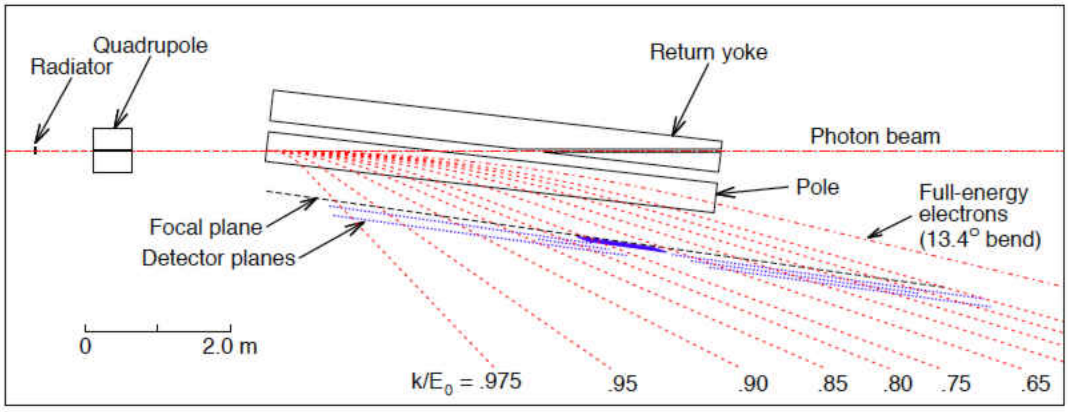

FIG. 13: Schematic of the photon tagging system. Red dotted lines indicate the scattered electron trajectories and k/E_0 is the ratio of the photon and incoming electron beam energy. Blue dotted lines indicate the three layers of hodoscope counters. Blue shaded region indicates the TAGM active volume. Figure from Ref. [21].

The scattered electrons are deflected by the tagger magnet which is a dipole magnet. When the electrons have only small amount of energy lost due to the Bremsstrahlung process, or are not interacted with the radiator, they are deflected by 13.4° into the electron beam dump. The electrons that lose more than 25% of the initial energy are deflected by the magnet and detected in TAGH or TAGM which lie on the focal plane on the magnet. Depending on the energy the scattered electrons are deflected by smaller or larger angles and go through the scintillating fiber bundles of TAGH or TAGM and read out by photomultipliers (PMTs). Those having large energies are bent less and those with smaller energies bend more. The tagger microscope detects scattered electrons with energies between 3.0 and 3.6 GeV and as a result tags the coherent photons between 8.4 and 9.0 GeV. It has counters that provide width of 9.1 MeV to 11.2 MeV and has a 0.1% energy resolution and timing resolution of 200 ps. The tagger hodoscope detects scattered electrons with energies from 0.22 GeV to

9.0 GeV and tags the photons from 3.0 GeV to 11.7 GeV. It has coarse counters with 8.5 MeV to 30 MeV energy width.

3.1.3 COLLIMATORS

The active collimator is located before the primary collimator. It consists of a large tungsten plate divided into two radial rings and four quadrants. The active collimator is used to monitor the photon beam position. The deviations of the beam from the nominal position are detected by studying the induced currents on the tungsten plates from particle showers caused by the photons.

The primary collimator is used to increase the fraction of linearly polarized photons delivered to the target. It is located 75m downstream of the radiator and is shielded by lead. It is used with a 3.4 mm or 5.0 mm aperture. The coherent part of the photon spectrum produced from the diamond radiator has the maximum polarization and has a lower angular spread compared to the incoherent part. The coherent spectrum is usually spread within 25 μrad from the beam direction. Additionally there is a secondary collimator and a sweeping magnet after the primary collimator. These are used to prevent the secondary photons and charged particles produced in the primary collimator being delivered any further.

3.1.4 TRIPLET POLARIMETER

The triplet polarimeter (TPOL) is used to determine the degree of polarization of the photon beam after the collimation. The TPOL works based on the "triplet photoproduction" process [24, 25] where the photon beam interacts with an atomic electron in a Be target foil in front of a Silicon Strip Detector (SSD). A high energy e^+e^- pair is produced and the atomic electron recoils with enough momentum to leave the atom. The recoil e^- is detected by the SSD which contains 32 azimuthal sectors and 24 concentric rings. By measuring the azimuthal angular distribution of the recoil e^-, the degree of polarization of the photon beam can be found. The cross section for triplet photoproduction is given by,

$$\sigma_t = \sigma_0[1 - P\Sigma \cos(2\phi)]\,, \tag{34}$$

where σ_0 is the unpolarized cross section, P is the polarization of the photon beam, Σ the beam asymmetry for the process and ϕ the azimuthal angle of the recoil e^- from the polarzation plane of the incident photon beam. Σ is calculated using QED [26]. Recoil electrons passing through the Be converter can also produce δ-rays so instead of triplet beam asymmetry Σ, the TPOL measures the analyzing power Σ_A which is a combination

of triplet production and δ-ray production. By fitting the yield of azimuthal distribution of recoil e^- with

$$f(\phi) = A[1 - B\,\cos(2\phi)] = \sigma_0[1 - P\Sigma_A\,\cos(2\phi)], \tag{35}$$

P can be found as B/Σ_A. The analyzing power for different photon beam energies can be found by simulation [26].

In Fig. 14 the beam polarization is shown for different diamond orientations as a function of the incoming photon beam energy. Table 2 shows the corresponding polarization values for each diamond orientation. They are obtained from polarimeter measurements [26].

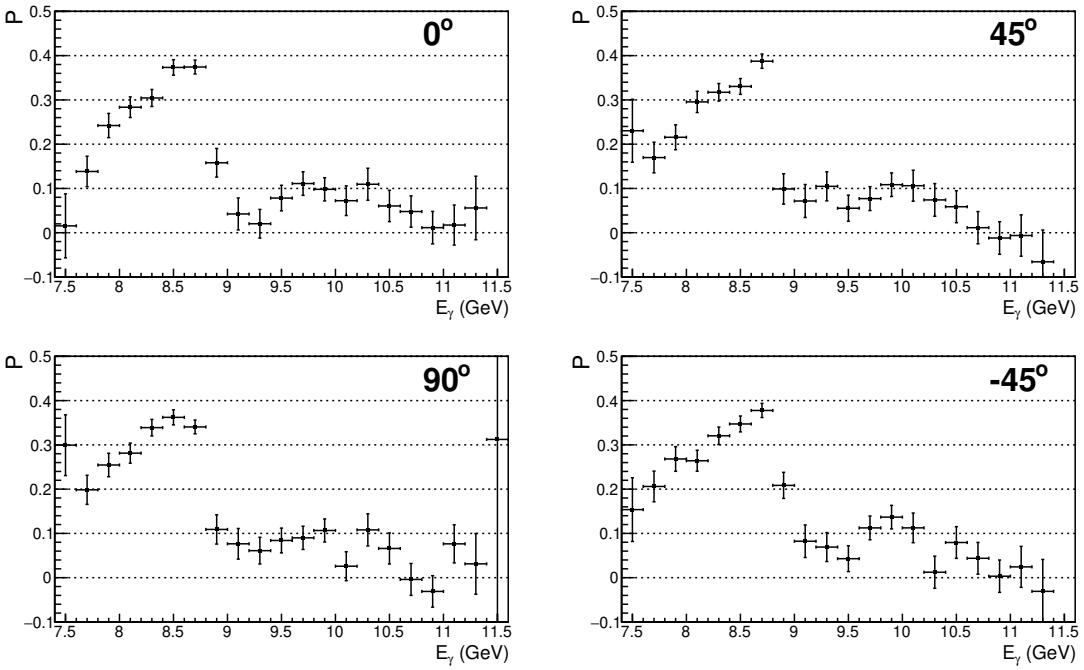

FIG. 14: Photon beam polarization as a function of the beam energy for different diamond orientations, as measured by the triplet polarimeter.

Diamond orientation	Polarization	Statistical uncertainty
0°	0.3536	0.0100
45°	0.3484	0.0102
90°	0.3472	0.0098
-45°	0.3513	0.0102

TABLE 2: Photon beam polarization for different diamond orientations from TPOL measurements.

3.1.5 PAIR SPECTROMETER

The Pair Spectrometer (PS) is used to measure the energy and the flux of photons after the collimation and also provides identification of the electron beam bunch corresponding to events with a coincidence hit in PS and TAGH/TAGM. The incoming beam photon produces a e^+e^- pair after interacting with the Be foil in front of the TPOL. This lepton pair is bent by a dipole magnet and detected by two scintillator detectors: a high-resolution hodoscope (PS) and a course hodoscope (PSC) as shown in Fig. 15. The high-resolution hodoscope reads out the light signals using Silicon Photomultipliers (SiPMs). Light from the PSC counters is read out by PMTs. Each detector has two arms positioned symmetrically with respect to the photon beamline and covers a momentum range between 3.0 GeV/c and 6.2 GeV/c of the lepton pair. This allows to reconstruct photons between energy 6.0 GeV to 12.4 GeV. PSC trigger helps to reduce the background originating from interactions of leptons in the magnet. PS hodoscope has energy resolution of about 25 MeV. PSC counters have timing resolution of about 120 ps. The pair spectrometer can also be used for energy calibration of the TAGH and TAGM.

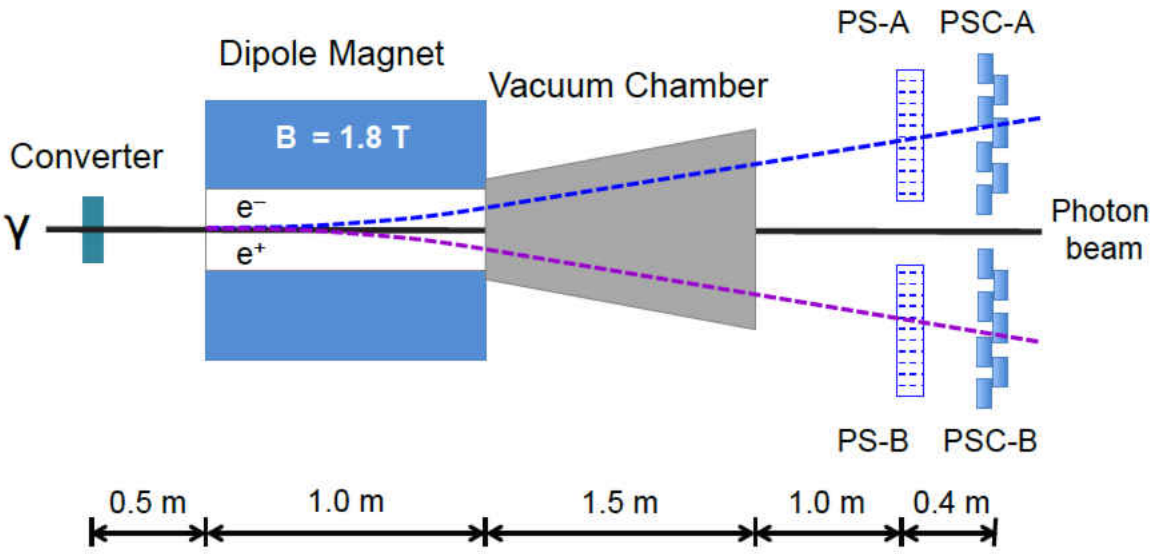

FIG. 15: Schematic of the pair spectrometer [27]. The blue and purple dashed lines indicate the trajectories of e^- and e^+ after being bent by the dipole magnet. PS and PSC indicate the high-resolution hodoscope and the coarse hodoscope.

3.2 MAIN SPECTROMETER

The GlueX main spectometer is shown in Fig. 16. The photon beam is incident on a liquid hydrogen target housed in a superconducting solenoid magnet. It provides a 2 T magnetic field and contains the start counter, central and forward drift chambers and the barrel calorimeter. The start counter is used to measure primary interaction time. Drift chambers detect charged particles while the barrel calorimeter is for detection of neutral showers. The forward calorimeter (FCAL) provides detection for forward photons and the time-of-flight is used for particle identification.

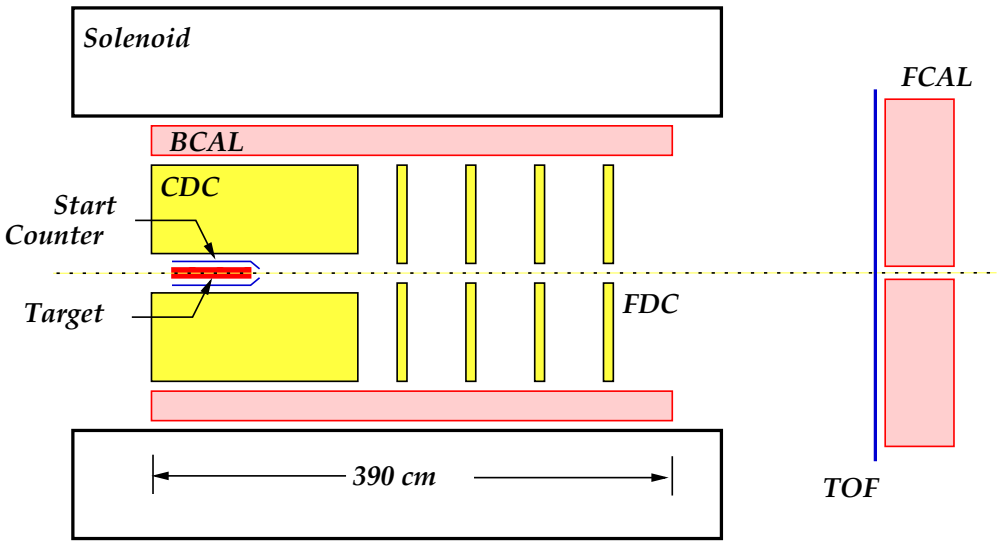

FIG. 16: Schematic of the main GlueX spectrometer.

3.2.1 LIQUID HYDROGEN TARGET

Figure 17 shows a schematic of the GlueX target. It's a cryogenic target and consists of a kapton cell containing liquid hydrogen (LH_2). The target is unpolarized and 30 cm long and has a diameter around 2 cm. The target is kept at a temperature and pressure around 20 K and 19 psi.

3.2.2 START COUNTER

The Start Counter (ST) surrounds the 30 cm long liquid hydrogen target and provides $\sim 90\%$ of 4π solid angle coverage relative to the target center (Fig. 18.) The start counter

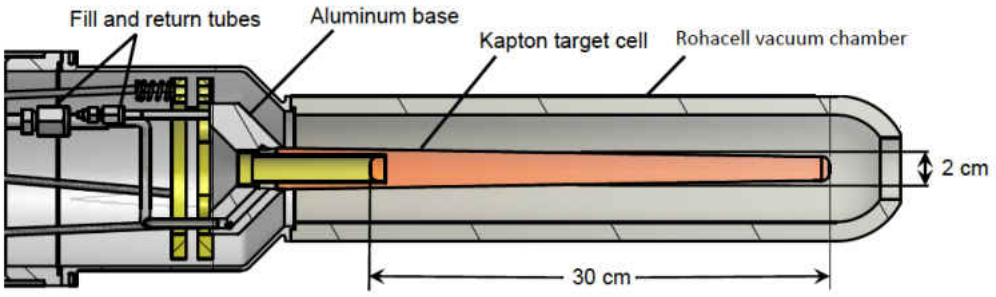

FIG. 17: Schematic of the GlueX liquid hydrogen target. Figure from Ref. [28].

consists of an array of 30 scintillator paddles. These are arranged in a cylindrical shape and have pointed ends bending towards the beamline at the downstream end. Light sensing is done by SiPM detectors which are not affected by the 2 T magnetic field produced by the GlueX solenoid magnet. The ST is primarily used for the identification of the photon beam bunch associated with the primary interaction with the target. The time of the interaction is compared with the RF beam bunch timing to select the main beam bunch. The ST operates at tagged photon rates of up to $10^8\,\gamma/\mathrm{s}$. The start counter has an average measured timing resolution of 550 ps (FWHM) which considerably surpasses its design resolution of 825 ps (FWHM) [29]. The ST also can be used in particle identification by comparing hit times of particles in other sub detectors with the measured ST time.

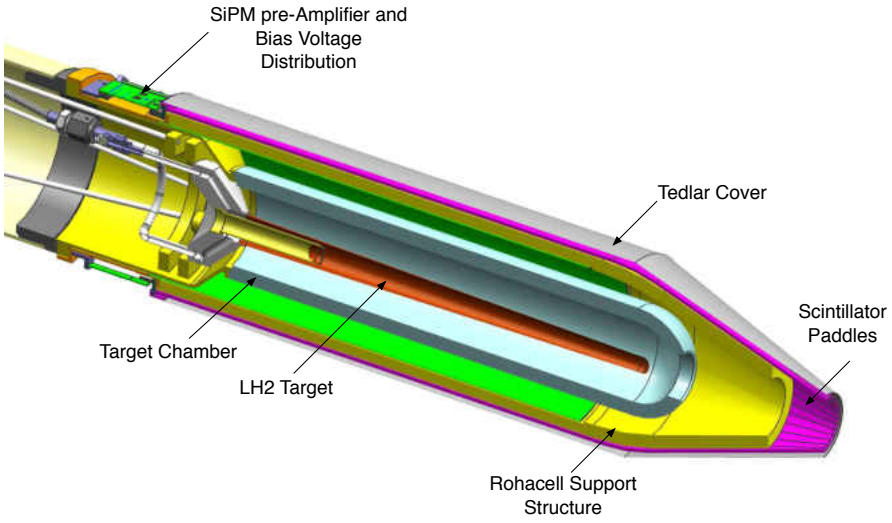

FIG. 18: Start counter surrounding the LH_2 target. The beam direction is from left to right down the central axis of the ST. Figure from Ref. [29].

3.2.3 TIME OF FLIGHT DETECTOR

The Time-of-flight (TOF) detector is located about 5.5 m downstream from the target. It consists of an array of scintillator paddles aligned perpendicular to each other as shown in Fig. 19. Most of the paddles are 252 cm long and 6 cm wide with a thickness of 2.54 cm. There is a 12 $\times$ 12 cm^2 square hole in the center of the TOF that matches the beam hole in the forward calorimeter to allow photon beam to travel to the beam dump. The TOF covers polar angles from 0.6° to 13° and has a timing resolution of around 100 ps. It is used for the particle identification for forward going charged particles. There are PMTs to read out energy and time of those particles that have hits in the TOF. Flight time of a particle is taken as the difference between measured arrival time in the TOF and the time of the corresponding RF beam bunch. Figure 20 shows the relativistic velocity β measured using the TOF vs momentum for different charged particles. As can be seen from the bands on the plot, it allows to separate proton from other lighter particles up to 3 GeV/c in the momentum. Pion-kaon separation is possible only up to around 2 GeV/c as the kaon band tends to merge with the pion and positron bands for higher momenta.

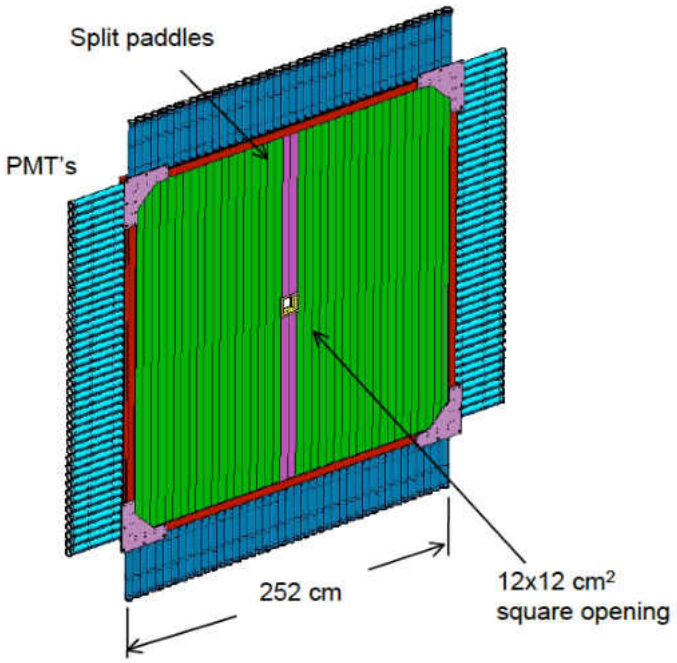

FIG. 19: Design of the GlueX TOF wall. Figure from Ref. [30].

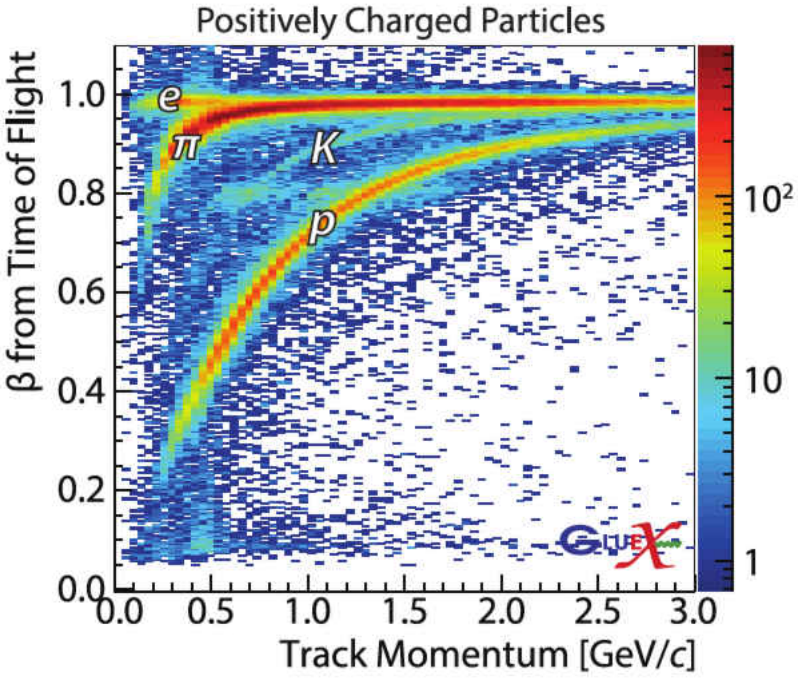

FIG. 20: Relativistic velocity β measured using TOF vs momentum for positively charged particles. Positron, pion, kaon and proton bands are labelled as e, π, K and p respectively. The horizontal band around $\beta \approx 0.8$ is due to an accidentally-tagged photon beam bunch. Figure from Ref. [30].

3.2.4 CENTRAL DRIFT CHAMBER

The Central Drift Chamber (CDC) is a cylindrical straw-tube drift chamber surrounding the target and the start counter. The CDC is primarily used to track charge particles in the polar angle range 6° to 168° and has the optimum coverage for polar angles between 29° and 132°. The CDC consists of 3522 straws that are 1.5 m long and 1.6 cm in diameter. Each tube has a gold-plate tungsten wire of 20 μm diameter as the anode. The straw tube walls are made of several layers of kapton with a innermost layer of aluminum forming the cathode. A 50:50 mixture of argon and CO_2 gases flows through the straws. A charged particle travelling through a straw ionizes the gas and electrons drift towards the anode while ions drift towards the cathode. The CDC measures the drift time that is the time the ionization electron generated closest to the wire takes to reach the wire. This is measured using high-resolution flash Analog-to-Digital Converters (fADCs). The drift time is converted into a

distance from the wire and using the information from adjacent straw tubes charged particle tracks can be reconstructed. The straw tubes are arranged as 12 layers of axial (along the beam direction) and 16 layers of stereo (with a $\pm 6^{\circ}$ offset from axial) orientations as shown in Fig. 21. The offset of stereo layers improves the reconstruction of a tracks z-position. The CDC provides position measurements with a resolution in z of 2mm and 150 μm resolution in the $r\phi$ plane.

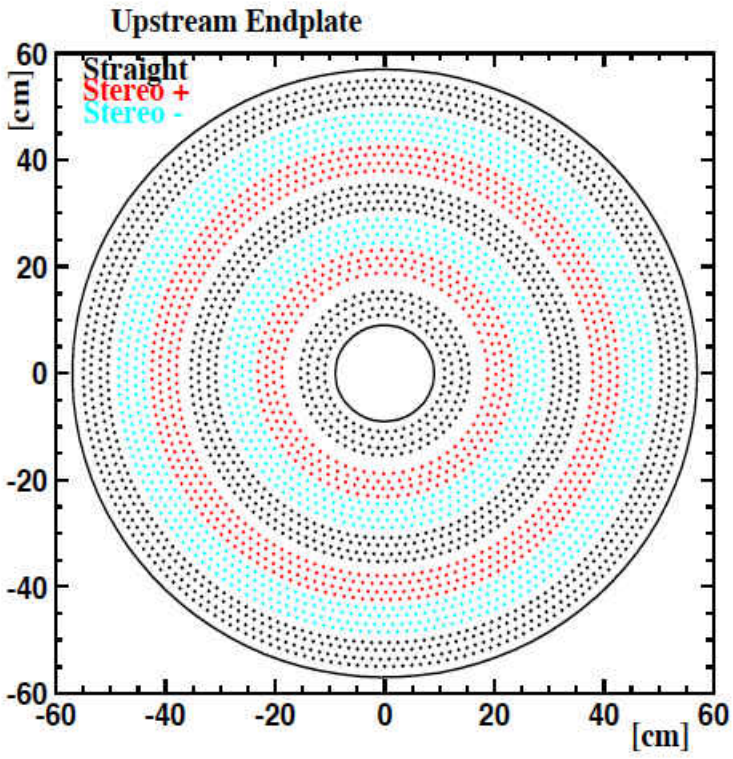

FIG. 21: Drawing of the CDC straw positions. Black dots represent axial straws, red and blue dots represent stereo straws that are offset by $\pm 6^{\circ}$ respectively. Figure from Ref. [31].

The CDC also provides a method of particle identification. For this the fADC is used to measure dE/dx, the amount of energy lost by the charged particle per unit distance in the gas. Figure 22 shows a plot of CDC dE/dx vs momentum for positively charged particles and it shows a clear separation of curved proton band from the horizontal band of other lighter particles for momenta below 1 GeV/c.

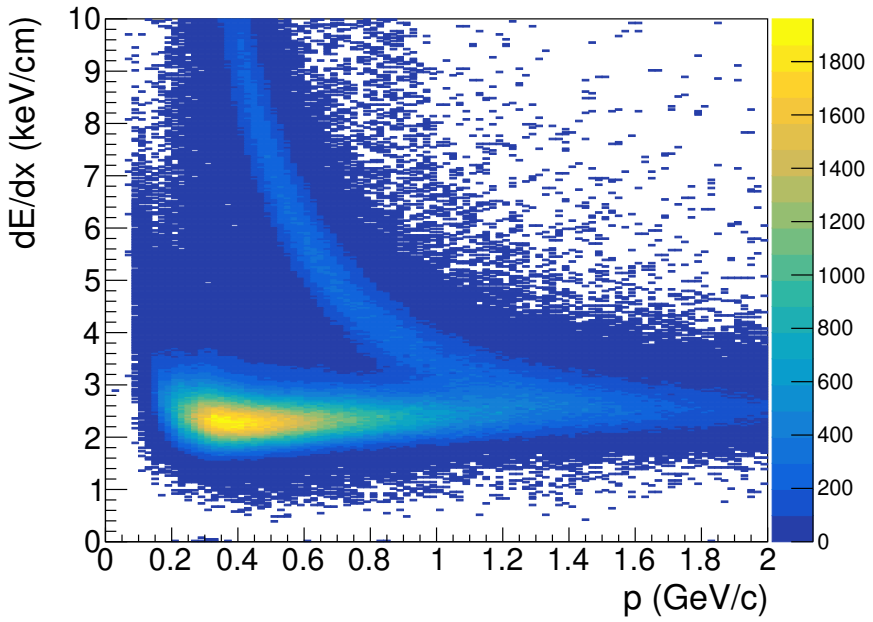

FIG. 22: Energy loss dE/dx in the CDC as a function of proton momentum. The curved band is for the proton candidates while the horizontal band is for lighter charged particles such as e^+, π^+ and K^+.

3.2.5 FORWARD DRIFT CHAMBER

The Forward Drift Chamber (FDC) system is located downstream of the CDC and within the solenoid magnet. It is used for the track reconstruction of forward going charged particles in the polar angle range from 1° to 20°. The FDC consists of 24 planar drift chambers of 1m diameter. These are grouped into 4 identical packages each containing 6 chambers. Each chamber contains of 1 "U" and 1 "V" plane of cathode wire strips and a plane of anode wires between the two cathode planes as shown in Fig. 23. The two cathode strip planes are oriented at ±75° with respect to the anode wires. Each chamber is rotated by 60° relative to the previous one.

A gas mixture of CO_2 and Ar with ratio of 40:60 is filled in a chamber and the ionization of the gas by traversing charged particles is used for the track reconstruction process. The two cathode strip planes provide reconstruction of the avalanche/hit position along the wire. The drift times from the anode wires are used to reconstruct the hit position perpendicular to the wire. Each chamber thus provides a three-dimensional space point of the track. By combining the information from the chambers the track can be reconstructed. The FDC can

reconstruct tracks with a position resolution better than the design resolution of 200 μm.

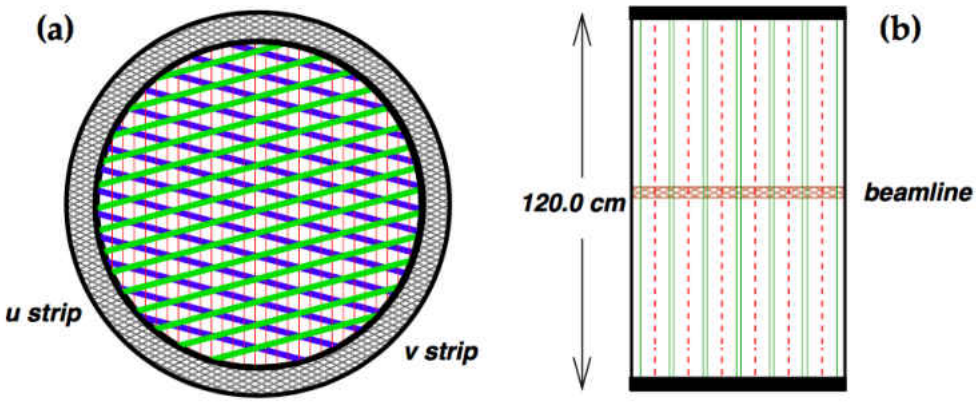

FIG. 23: (a) Front view of an FDC package. Anode wires are shown as red vertical lines. The thick green lines represent the u-strips and the thick blue lines represent the v-strips. The cathode strip planes are oriented at $\pm 75^\circ$ with respect to the anode wires. (b) Side view of a six-chamber package. The red-dashed lines represent the anode wires and the solid-green lines represent the cathode planes. Figure from Ref. [32].

3.2.6 BARREL CALORIMETER

The barrel calorimeter (BCAL) is an electromagnetic calorimeter located within the solenoid magnet surrounding CDC and FDC. It's cylindrically shaped with a length of 390 cm and inner and outer radii of 65 cm and 90 cm respectively. The BCAL can detect photon showers with energies between 0.05 GeV and few GeV. It has angular coverage of $11^\circ - 126^\circ$ in polar angle and $0^\circ - 360^\circ$ in azimuthal angle. The BCAL is made as a lead-scintillating fiber matrix. The 0.5 mm thick grooved lead sheets produce electromagnetic showers while the 1.0 mm diameter scintillating fibers collect the light. The fibers run parallel to the cylindrical axis. The particle showers deposit energy in the fibers. The fibers re-emit light with an amount that is directly proportional to the energy deposited.

Figure 24 shows the geometry of the BCAL and readout segmentation. The BCAL contains 48 trapezoidal modules with a single module having 4 layers that are radially oriented. The containment of showers is a function of the angle of the photon incidence. It is 15.3 radiation lengths for particles entering normal to the BCAL face and 67 radiation lengths for 14° incidence. At the each end of a module, the light guides collect the light from the

fibers and transport to silicon photomultipliers (SiPMs). The SiPMs have the advantage of being insensitive to the magnetic field.

Each of an upstream and downstream end of a BCAL module contains 40 SiPMs so there are 3840 SiPMs in total. The SiPMs within a layer are arranged such that there are 16 readout channels at a single end of a module resulting in a total of 1536 readout channels. The elecronic signal from a SiPM is delivered to a flash ADC (fADC). These readouts provide information about the energy, position and timing of the corresponding shower. In general, the showers can be produced by photons or charged tracks. The position information from the calorimeter hits are compared with the charged track information from drift chambers to find out if the showers are caused by the charged particles. The energy resolution of the BCAL is found to be $\sigma_E/E = 5.2\%\sqrt{E(\text{GeV})} \oplus 3.6\%$. The timing resolution of BCAL is $\sigma = 150$ ps at 1 GeV.

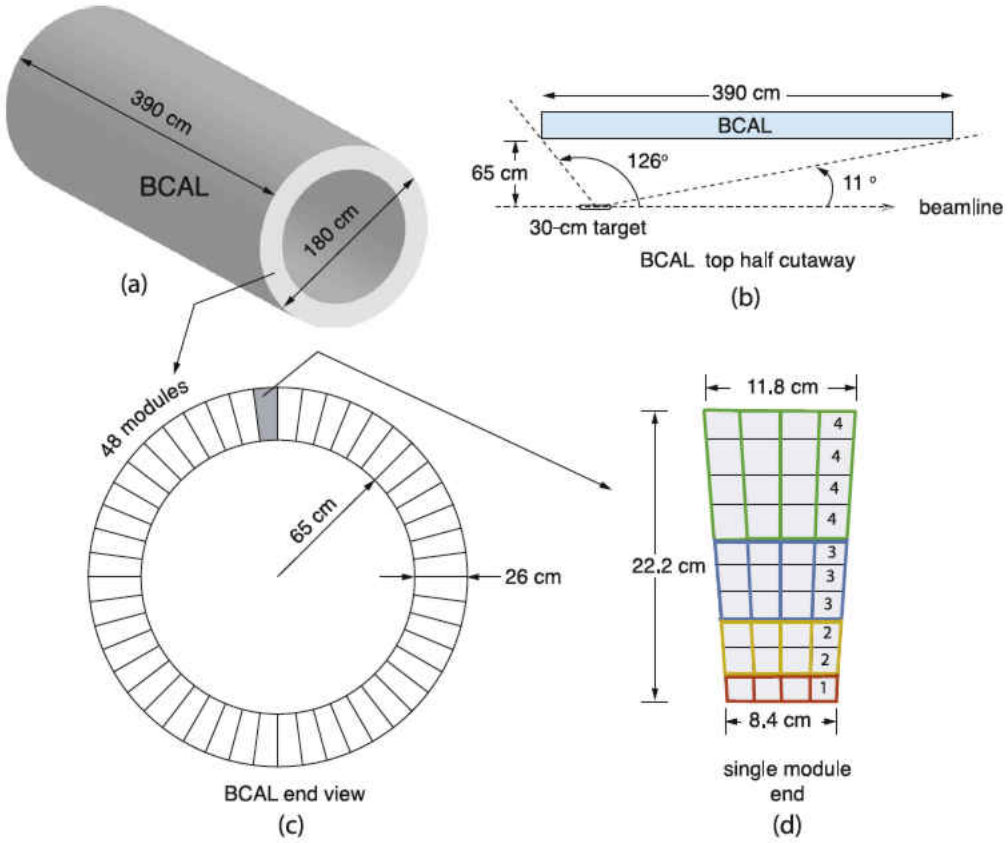

FIG. 24: (a) Schematic view showing dimensions of the BCAL. (b) Top-half cutaway of a BCAL module showing its polar angle coverage and position with respect to the hydrogen target. (c) End view of the BCAL showing 48 azimuthal modules. (d) End view of a single module showing the 40 SiPMs and the layer-wise orientation producing the 16 readout channels. Figure from Ref. [33].

3.2.7 FORWARD CALORIMETER

The forward calorimeter (FCAL) is located 5.6 m downstream from the GlueX target. It can detect photon showers in the energy range 100 MeV to 5 GeV and has a polar angle coverage of $\theta < 12^{\circ}$ [34]. The FCAL contains 2800 lead-glass blocks stacked in a circular array that has a radius of 1.2 m as shown in Fig. 25. The PMTs attached to lead-glass blocks detect the Cherenkov light emitted from the charged particles in the electromagnetic showers caused by the particles traveling through the blocks. The amount of light produced depends on the energy deposited by the initial particle. This can be caused by a charged particle or a neutral shower and is distinguished by matching calorimeter hits to charged tracks. Usually a shower will deposit energy in multiple blocks so they are grouped as clusters during the shower reconstruction process. Using the cluster information the energy, position and timing of the incident particle can be determined. The photon energy resolution of FCAL is found to be $\sigma_E/E = 5.931\%\sqrt{E(\mathrm{GeV})} \oplus 3.656\%$ from the studies of reconstruction of the $\pi^0 \to \gamma\gamma$ decay as shown in Fig. 26.

The FCAL also provides a method for separating electrons from charged hadrons. The E/p ratio of energy deposited in the calorimeter and the momentum of the charged track matched to that shower can be used for this purpose. Figure 27 shows an example plot of E/p versus the track polar angle and the electrons have values close to 1 because of their lighter mass compared to the charged hadrons.

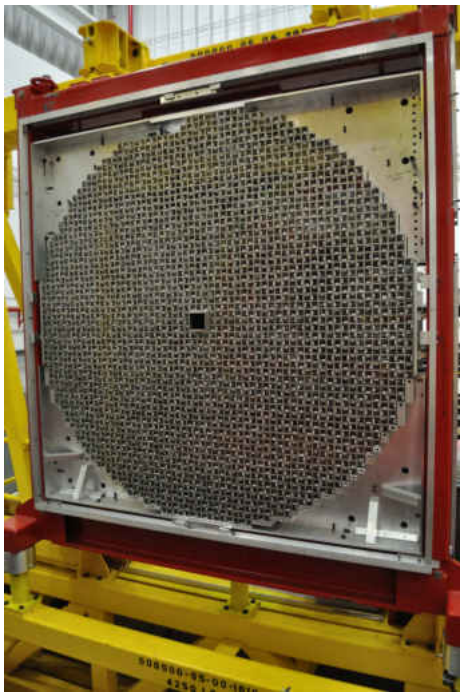

FIG. 25: View of front face of the FCAL [35].

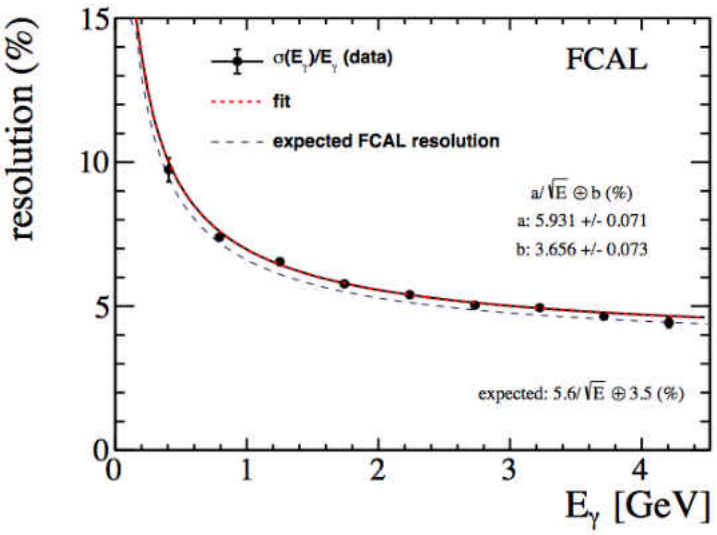

FIG. 26: Photon energy resolution in FCAL. Figure from Ref. [36].

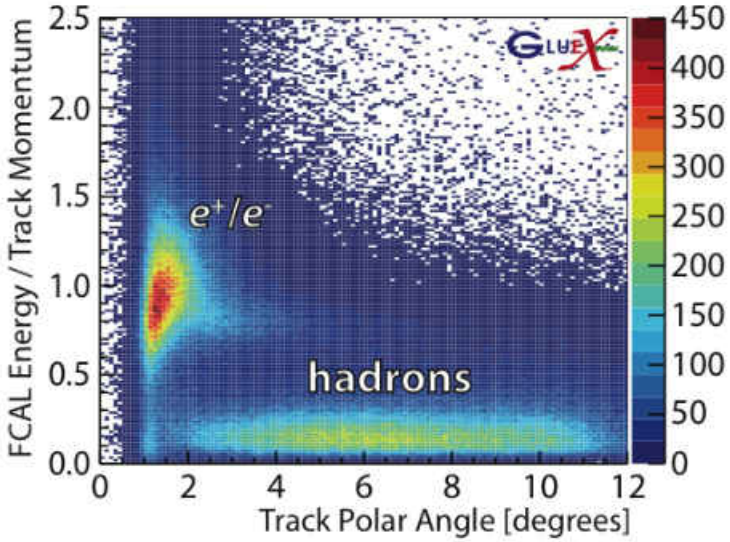

FIG. 27: Ratio of energy measured by the FCAL and the momentum of the charged track versus polar angle of the track. Figure from Ref. [37].

CHAPTER 4

DATA ANALYSIS

4.1 SPRING 2017 DATASET

In this analysis the beam asymmetry was measured with the data collected from the GlueX experiment during spring of 2017. The CEBAF provided a 11.6 GeV electron beam into Hall D. The data used corresponds to the first run period with physics data production and is about 20% of the GlueX phase I data set. Figure 28 shows a brief overview of the run conditions relevant to this data which is available in Ref. [38].

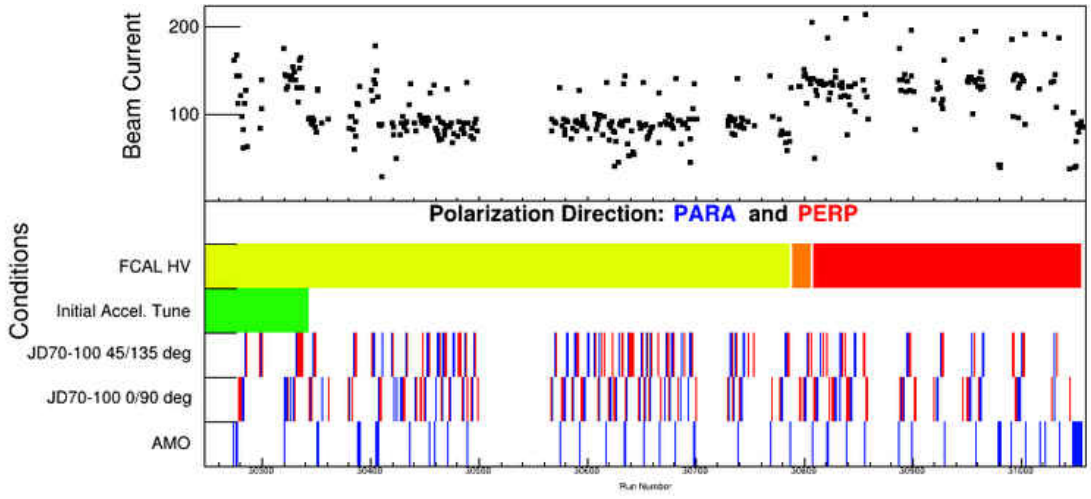

FIG. 28: Summary of the beam current and the detector conditions for spring 2017 GlueX data as a function of run number.

The analysis was done with the data taken with JD70-100 58μm thickness diamond radiator. The data corresponds to a total luminosity of 20.8 pb^{-1} in the photon beam energy range 8.2 to 8.8 GeV. The trigger signal was generated for events that deposited sufficient energy in FCAL and BCAL.

Two sets of polarization directions of beam were used in this analysis. One set contains $\phi = 0°$ as PARA and $\phi = 90°$ as PERP where ϕ denotes the polarization plane of the beam with respect to the lab floor. The other set is $\phi = -45°$ as PARA and $\phi = 45°$ as PERP.

The complete list of runs that was approved for physics analysis purposes for each diamond orientation is given in Appendix A.

The ROOT [39] trees used in this work were generated with the REST version 03 of 2017 data. The REST files consists of special format of files that are produced from the raw data of the runs after calibrations and monitoring and by the use of GlueX reconstruction code. These files were then converted to tree format to use with ROOT for physics analysis and the channel specific files were created in the analysis launch version 26.

4.2 EVENT SELECTION

The selection of $\gamma p \to K^+\Sigma^0$ was performed using the standard analysis software framework [40], using the standard JANA plugin, ReactionFilter. It produced ROOT trees containing the particle combinations for the channel. Then, using the DSelector software [41], these TTrees were analyzed.

The following standard cuts were used by the analysis library.

- Number of extra charged tracks ≤ 3
- Number of photons ≤ 15
- Event timing: 4 beam bunches before and after primary bunch (-18.036 ns $< t_{vertex} - t_{RF} <$ 18.036 ns)
- Particle timing cuts (Table 3)
- Standard CDC dE/dx cuts [42]
- Cut around Λ mass $M_{\pi^- p}$ = 1.0 - 1.2 GeV/c^2

Additionally, a cut on BCAL energy $>$ 50 MeV was used to keep events having low energy final photons.

Samples of $K^+\Sigma^0$ and $K^+\Lambda$ Monte-Carlo (MC) events were generated using genr8 software and they were compared with real data after detector simulation and reconstruction to study the validity of cuts applied and the sources of background. Parameters used for MC simulation are given in Appendix B.

4.2.1 PLUGIN REQUIREMENTS

In the ReactionFilter plugin, candidate particles were selected to match the reaction under study. This is known as a “combo” or a “combination”. It was required to have at

least one tagged beam photon, two reconstructed positively charged tracks (K^+ and proton), one negatively charged track (π^-) and a neutral shower (γ) in calorimeters.

The reaction tag 1_14__1_11_18__B4_M18 was used for the ReactionFilter plugin. The output TTree was called "gkplamb__B4_M18_Tree" according to the final state particles it had. So, the reaction was reconstructed as two steps.

1. $\gamma p \rightarrow \gamma K^+ \Lambda$

2. $\Lambda \rightarrow \pi^- p$

The $\pi^- p$ mass spectrum was not constrained just to the Λ mass region (with the use of M18 flag) in order to study if there's any background under the Λ peak.

A kinematic fit was applied satisfying 4-momentum conservation and constraining the event vertex. Then, two charged tracks for the particles coming from Λ decay were required to come from a secondary vertex. At the plugin level, the kinematic fit was required to converge (Confidence Level > 0).

The resulting reconstructed event was required to have a missing mass squared, $MM^2 = (p_i - p_f)^2$, be of magnitude less than 0.1 $(\mathrm{GeV}/c^2)^2$, where

$$p_i - p_f = (p_\gamma^{beam} + p_{proton}^{target}) - (p_\gamma + p_{K^+} + p_{\pi^-} + p_{proton}) \tag{36}$$

where p_γ^{beam}, p_{proton}^{target}, p_γ, p_{K^+}, p_{π^-} and p_{proton} are the 4-momentum of the tagged beam photon, target proton at rest, measured final state photon, measured final state tracks of kaon, pion and proton respectively.

Two cuts were applied for particle identification (PID). The first cut applied is on dE/dx in order to distinguish between the final state proton and other positively charged particles. Although the reaction doesn't have any π^+ or e^+on it, a positively charged track in the combination can satisfy four hypotheses (K^+,π^+,e^+ and proton). The energy deposited in the drift chambers by charged tracks can be used to distinguish these. The cut applied is $\mathrm{dE/dx} > e^{(-4.0\times x+2.25)}+1.0$ [42] and is effective for particle momenta ≤ 1.0 GeV/c. Figure 29 shows the energy loss dE/dx as a function of proton momentum after the cut.

The second cut used for particle identification is for particle timing. For each candidate particle, track flight time from the track vertex to each detector was calculated assuming the mass of the hypothesis. Then, the time difference (Δt) between this vertex time and RF beam bunch was used to identify particles. These cuts are shown in Table 3 [42].

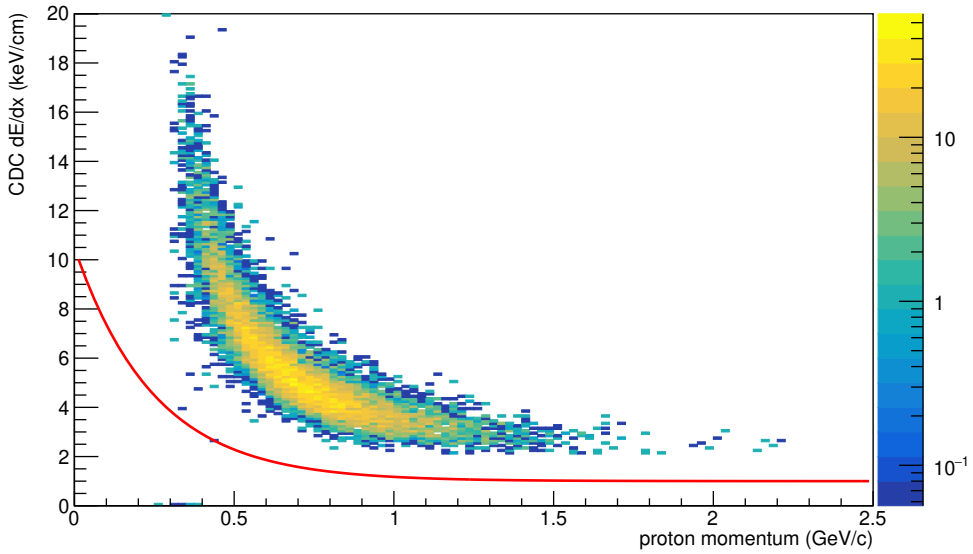

FIG. 29: Energy loss dE/dx in the Central Drift Chamber (CDC) as a function of proton momentum. Red curve represents the loose cut on dE/dx for proton identification.

Particle Type	BCAL cut	TOF cut	FCAL cut
Proton	$\|\Delta t\| < 1.0$	$\|\Delta t\| < 0.6$	$\|\Delta t\| < 2.0$
K^+	$\|\Delta t\| < 0.75$	$\|\Delta t\| < 0.3$	$\|\Delta t\| < 2.5$
π^-	$\|\Delta t\| < 1.0$	$\|\Delta t\| < 0.5$	$\|\Delta t\| < 2.0$
γ	$\|\Delta t\| < 1.5$	-	$\|\Delta t\| < 2.5$

TABLE 3: Timing cuts (Δt) for different particles in the BCAL, TOF and FCAL. Times are in ns.

4.2.2 COMBINATION SELECTION

The $\gamma p \to \gamma K^+ \Lambda$ candidate combinations were selected at the DSelector stage using the following cuts:

- Beam energy: 8.2 GeV $< E_{beam} <$ 8.8 GeV
- Measured missing mass squared: $|MM^2| < 0.08$ (GeV/c^2)^2
- Kinematic fit confidence level (CL) $> 10^{-4}$ (Corresponds to χ^2/ NDF (number of degrees of freedom) < 5)
- K^+ vertex z position: 51.2 cm $< z <$ 78.8 cm
- K^+ vertex radial position: $r <$ 1.0 cm
- FCAL shower quality > 0.5

The quantities plotted were found using kinematically fit 4-vectors except for the measured missing mass squared.

The coherent peak energy range of 8.2 GeV $< E_{beam} <$ 8.8 GeV was chosen for the events, because the beam polarization is maximum in that energy range and to match the TPOL analysis of polarization values.

Figure 30 shows the time difference $\Delta t = t_{vertex} - t_{RF}$ between the event vertex time, as measured with the final state particles and projected back to the vertex, and the RF time. The electron beam provided from the accelerator comes as bunches that are in 4 ns intervals. The region between the blue lines indicates the signal region (-2.004 ns $< \Delta t <$ 2.004 ns) consisting of a single RF bunch. The red lines indicate the sample of out of time RF bunches used as accidentals. Contribution from this accidentally tagged beam photons as a background must be estimated and subtracted. It will be discussed further in Sec. 4.2.3.

Figure 31 shows the measured missing mass squared distribution. It should be peaking around zero since the reaction under study is exclusive (all final particles are detected). A loose cut on the magnitude of the missing mass squared was applied to be less than 0.08 (GeV/c^2)^2 (as shown by red dashed lines).

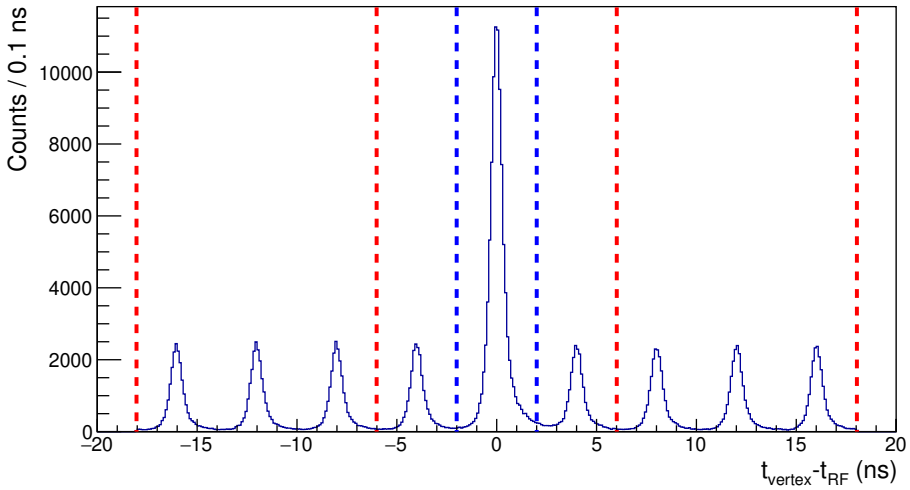

FIG. 30: Time difference between event vertex and RF time. The dashed blue lines indicate the in-time beam photons and the dashed red lines indicate the out-of-time beam photons that will be used for accidental subtraction.

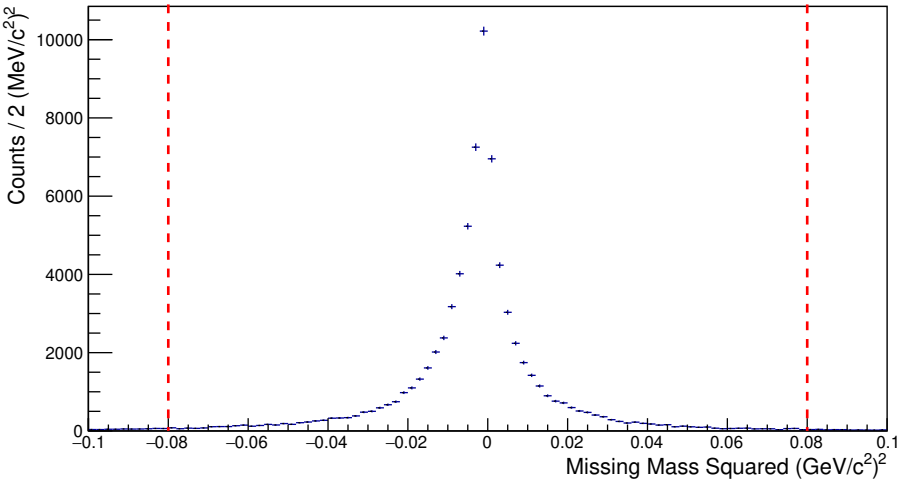

FIG. 31: Missing mass squared distribution for the reaction $\gamma p \to \gamma K^+ \pi^- p$

As can be seen in Appendix E, the loss of signal events is only 0.7% when tightening the cut to 0.08 $(\mathrm{GeV}/c^2)^2$ from the default analysis library cut at 0.1 $(\mathrm{GeV}/c^2)^2$. Furthermore, Fig. 32 shows the missing mass squared distribution in log scale with all the other cuts

applied and $M_{\Lambda\gamma}$ within the Σ^0 peak. It clearly shows that the reduction of signal events due to the cut at 0.08 $(\mathrm{GeV}/c^2)^2$ is negligible. The effect of loosening and tightening of the cut on beam asymmetry results will be shown in Sec. 5.5.1.

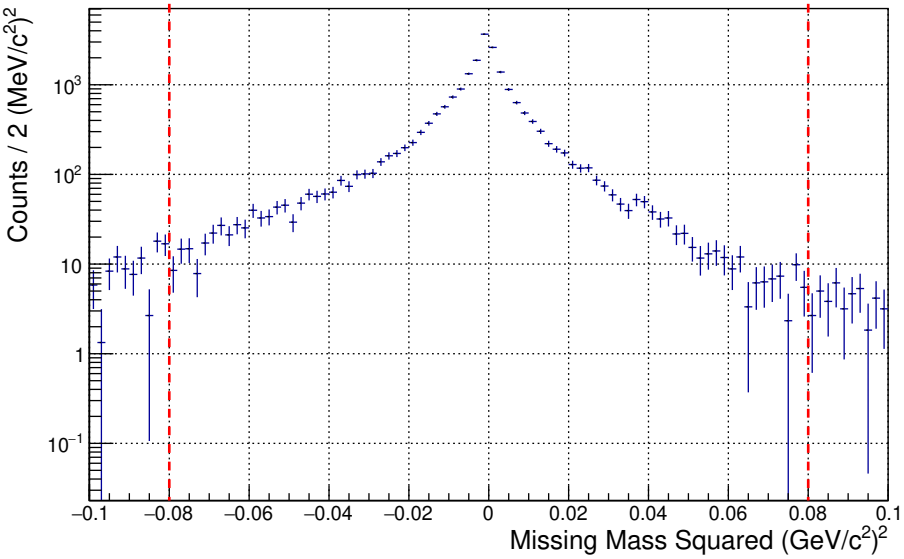

FIG. 32: Missing mass squared distribution in log scale for the reaction $\gamma p \to \gamma K^+\pi^- p$ with events selected in the Σ^0 peak.

The kinematic fit was introduced in Sec. 4.2.1. A cut of CL $> 10^{-4}$ was used in order to remove the background. A very loose cut was not applied on the confidence level as it results in similar statistical errors for yield asymmetry fits described in Sec. 5.3 but giving much higher value for χ^2/NDF of the kinematic fit. (For an example CL $> 10^{-10}$ corresponds to a χ^2/NDF < 10.6 and an example plot of yield asymmetry fits for this cut is given in Appendix E.) Figure 33 shows the kinematic fit confidence level distribution and the applied nominal cut is indicated by red dashed line. This cut corresponds to a cut on χ^2/NDF < 5 and is shown in Fig. 34.

Since the K^+ track should be originating from the target region, cuts were applied on the z and r vertex positions of the reconstructed kaon's distance of closest approach to the beamline. A study was done to find the resolution in target z using $K^+\Sigma^0$ t-channel MC and the relevant figures are shown in Appendix D.1. A 3σ cut was made for the target windows from positions at z=50.3 cm and z=79.6 cm. Based on this studies the K^+ vertex z position is required to be between 51.2 and 78.8 cm (Fig. 35) in order to avoid events that can be

produced from the target windows. The vertex radius r was required to be less than 1.0 cm (Fig. 36) consistent with the radial size of the liquid hydrogen target.

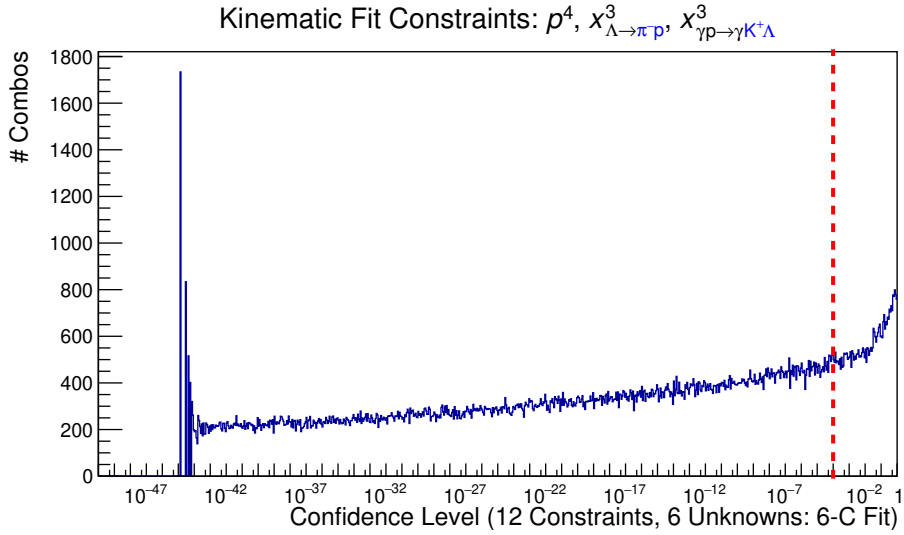

FIG. 33: Kinematic fit confidence level distribution for data. X-axis is in the log scale.

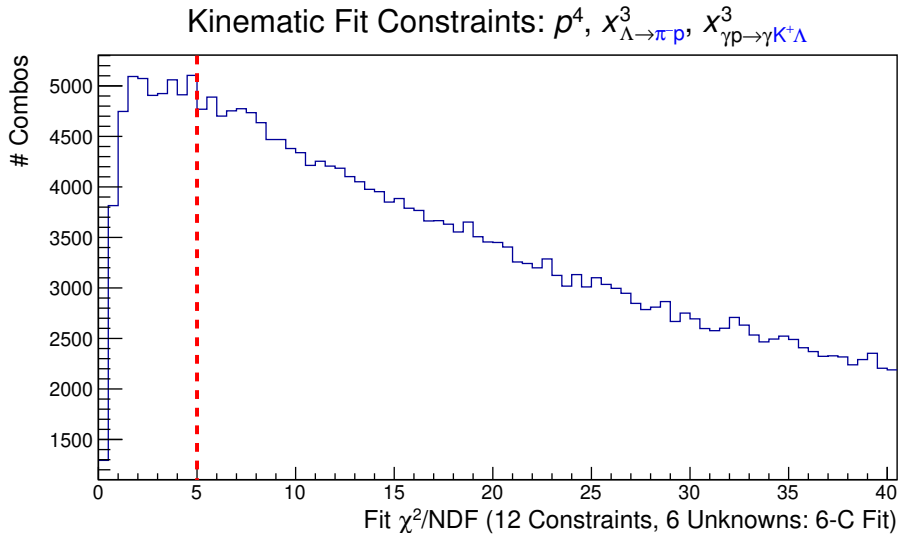

FIG. 34: Kinematic fit χ^2/ NDF distribution.

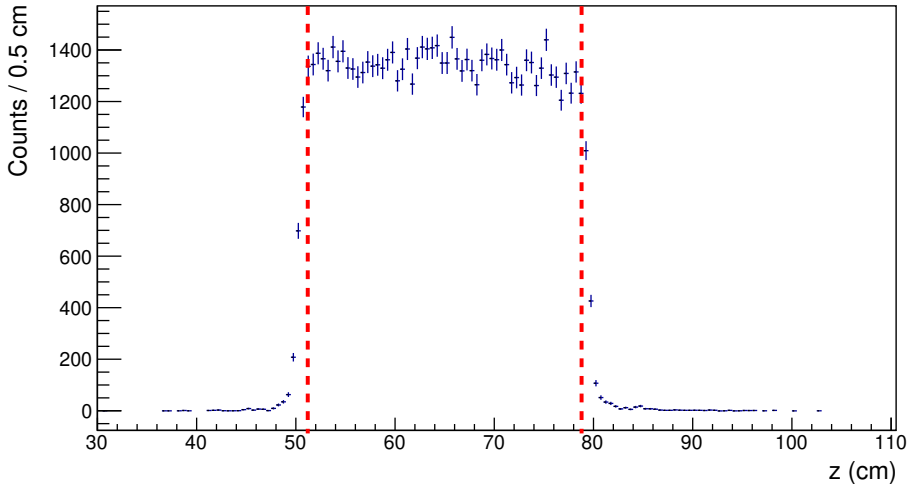

FIG. 35: Vertex position along the beamline for K^+.

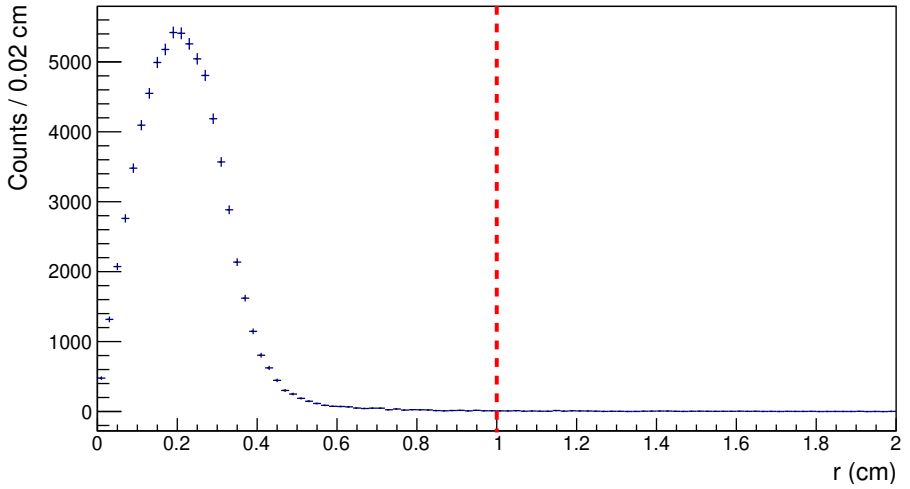

FIG. 36: Radial vertex position for K^+.

Figure 37 shows the invariant mass of $\pi^- p$ after the cuts mentioned above. $\Lambda^0(1116)$ peak is clearly seen with some background remaining above the Λ mass range. However, it'll be shown that Λ's from the Σ^0 peak don't have any background under it.

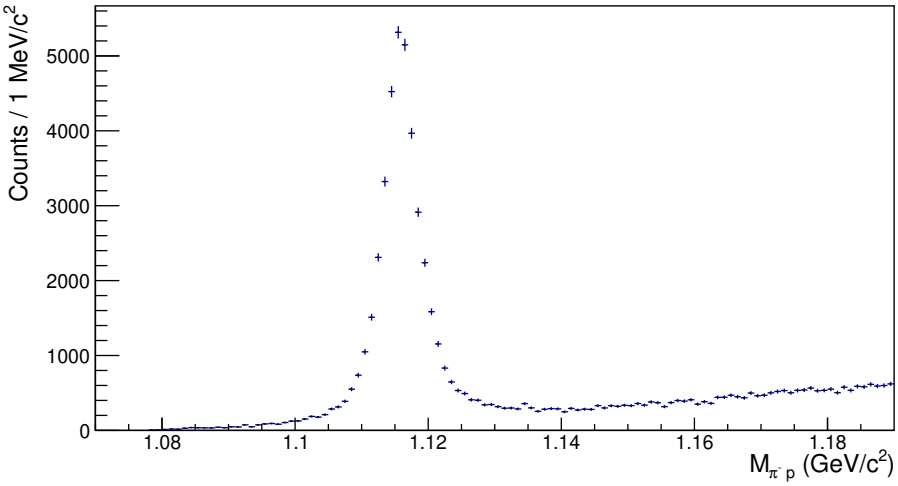

FIG. 37: The accidental subtracted histogram for invariant mass of $\pi^- p$ after the cuts applied.

Figure 38 shows the fit to accidental subtracted histogram of $M_{\pi^- p}$. Analogous Gaussian width (σ) was found as 3 MeV using the full width half maximum (FWHM) of the Voigtian (σ = FWHM / ($2\ \sqrt{2\,ln2}$)). Events within the range $|M_{\pi^- p} - M_\Lambda| < 3\sigma$ were selected and invariant mass of $\Lambda\gamma$ was constructed. Figure 39 shows this and according to this, a considerable amount of background is underneath the $\Sigma^0(1193)$ peak.

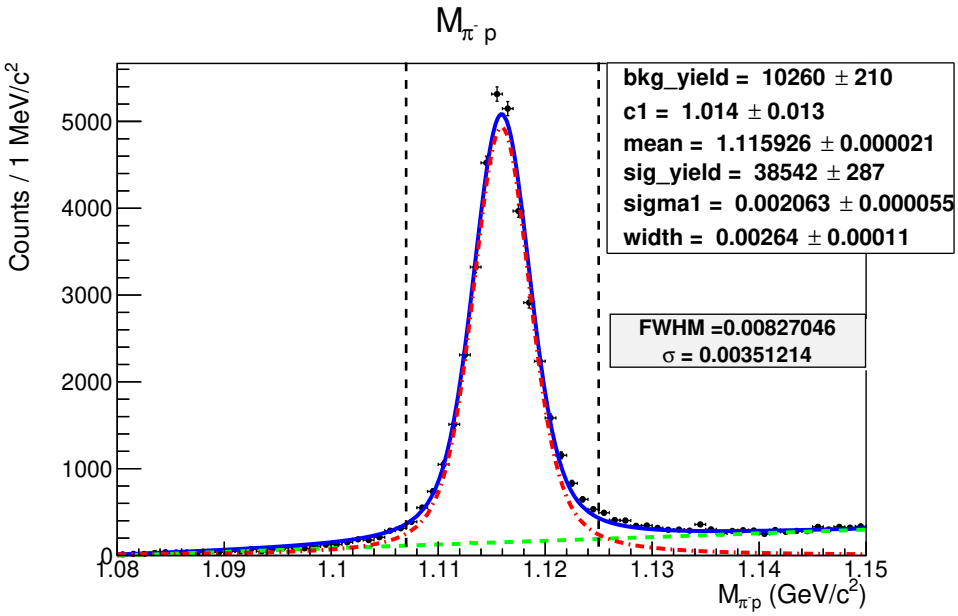

FIG. 38: Invariant mass of $\pi^- p$ distribution fitted with the Voigtian function for a signal (red dot dashed curve) plus first order Chebychev polynomial for the background (green dashed curve). The blue solid curve is a result of the total fit. The fit gives a χ^2/NDF = 314.50/66 = 4.77. Dashed vertical lines represent the region of Λ events selected for the analysis.

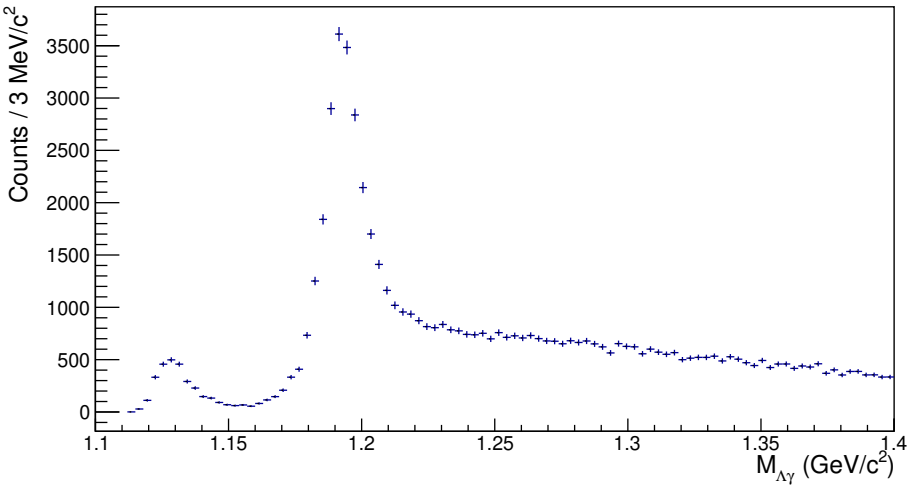

FIG. 39: The accidental subtracted histogram for invariant mass of $\Lambda\gamma$.

There can be split-off showers that produced from charged hadrons interacting with calorimeters. These are not matched to charged tracks and can be mis-identified as photons.

So, the shower quality is used as a kinematic topology to study any correlation to this background.

The shower quality variable is a new method introduced by GlueX FCAL group [43]. It is included in the ROOT trees as NeutralHypo__ShowerQuality. It gives a quality score between 0 and 1 to a neutral shower in FCAL using machine learning techniques. So, it can be used to remove uncorrelated showers.

Figure 40 shows the invariant mass of $\Lambda\gamma$ versus shower quality in FCAL. It is evident that the background with higher masses above the Σ^0 region and the lower mass peak is associated with lower quality values of the shower (close to 0). Furthermore it was found from simulation that $K^+\Lambda$ t- and u-channel events combined with a neutral shower form this background.

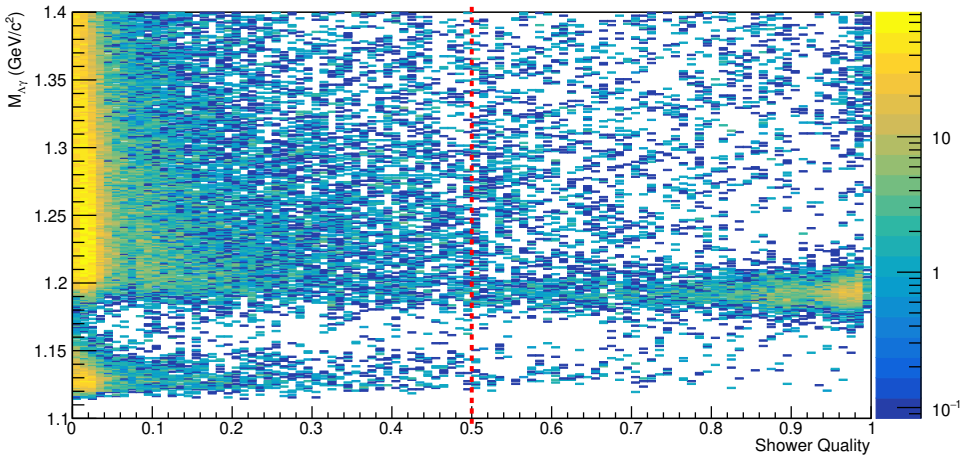

FIG. 40: Invariant mass of $\Lambda\gamma$ vs FCAL shower quality.

A cut of FCAL shower quality > 0.5 was used to get rid of this background. Effect of this cut on invariant mass of $\Lambda\gamma$ spectrum can be seen in Fig. 41. Figures 42 and 43 show that the shower quality cut eliminates the background coming from $K^+\Lambda$ channel.

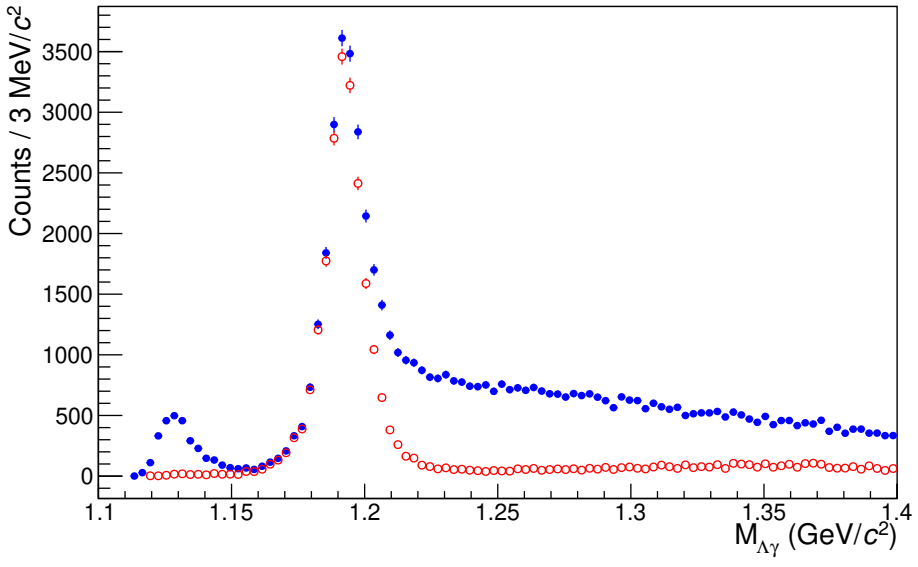

FIG. 41: Invariant mass of $\Lambda\gamma$ before (blue solid circles) and after shower quality > 0.5 cut (red open circles).

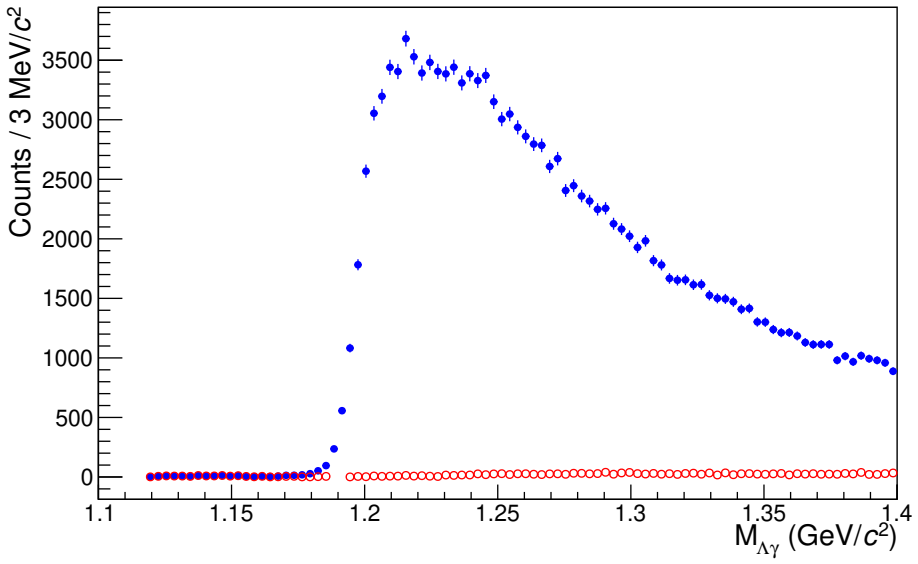

FIG. 42: Comparison of $K^+\Lambda$ t-channel events before (blue solid circles) and after (red open circles) shower quality > 0.5 cut (MC).

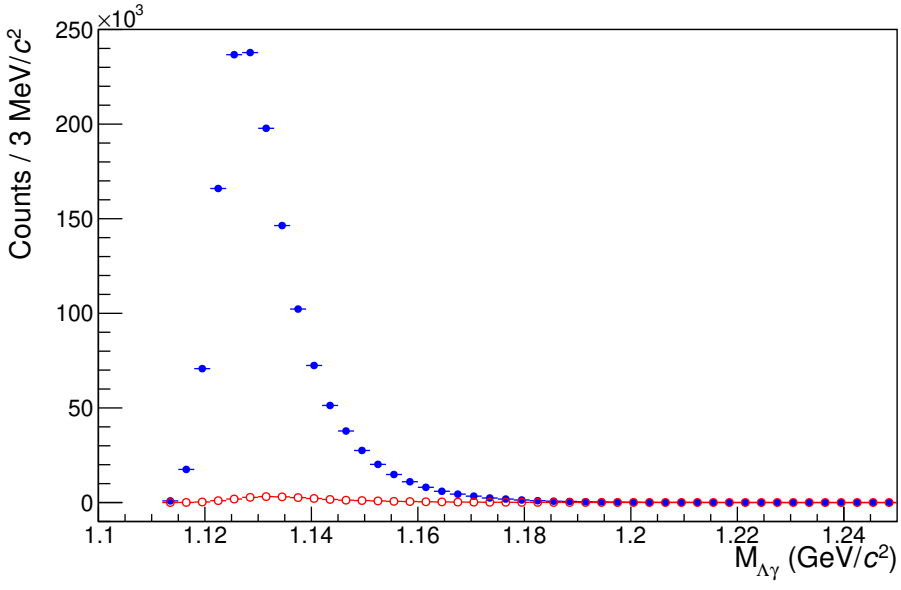

FIG. 43: Comparison of $K^+\Lambda$ u-channel events before (blue solid circles) and after (red open circles) shower quality > 0.5 cut (MC).

Figure 44 shows a fit to the accidental subtracted histogram of invariant mass of $\Lambda\gamma$ after all the cuts including FCAL shower quality > 0.5. The width (σ) of Σ^0 peak is about 8 MeV. Events within the range $|M_{\Lambda\gamma} - M_\Sigma| < 3\sigma$ were selected for the beam asymmetry analysis. Background under the Σ^0 peak was found to be $\sim$2%. The fractions of background under the Σ^0 peak for different $-t$ bins and the $-u$ bin used in the analysis are shown in Appendix D.3.

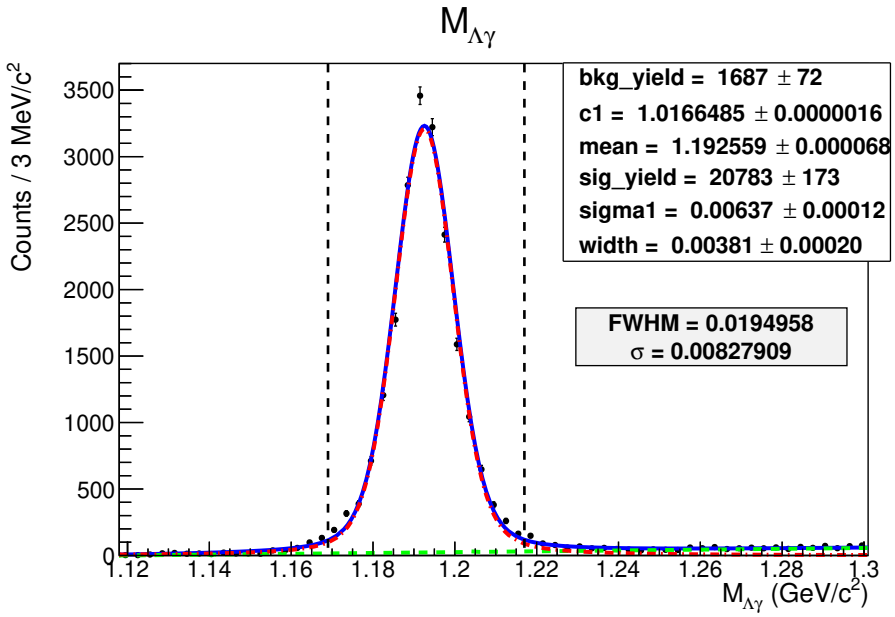

FIG. 44: Invariant mass of the $\Lambda\gamma$ distribution fitted with a Voigtian function for the signal (red dot dashed curve) plus first order Chebychev polynomial for the background (green dashed curve). The blue solid curve is a result of the total fit. The fit gives a $\chi^2/\text{NDF} = 249.31/56 = 4.45$. Dashed vertical lines represent the region of Σ^0 events selected for the analysis.

Using the MC for $K^+\Sigma^0$ reaction, a study was done about the photon polar angle (θ_γ) distribution. Figures 45 and 46 show θ_γ distributions for $K^+\Sigma^0$ t-channel and u-channel. Events were selected in the range 1.169 GeV/c^2 $< M_{\Lambda\gamma} <$ 1.217 GeV/c^2 to match with the mass region selected for data. From this, we see that almost all photons in the t-channel go to BCAL ($\theta_\gamma > 11°$) while most photons in the u-channel go to FCAL (fraction of photons in the range $1° - 11°$ from Fig. 46 is 67%.)

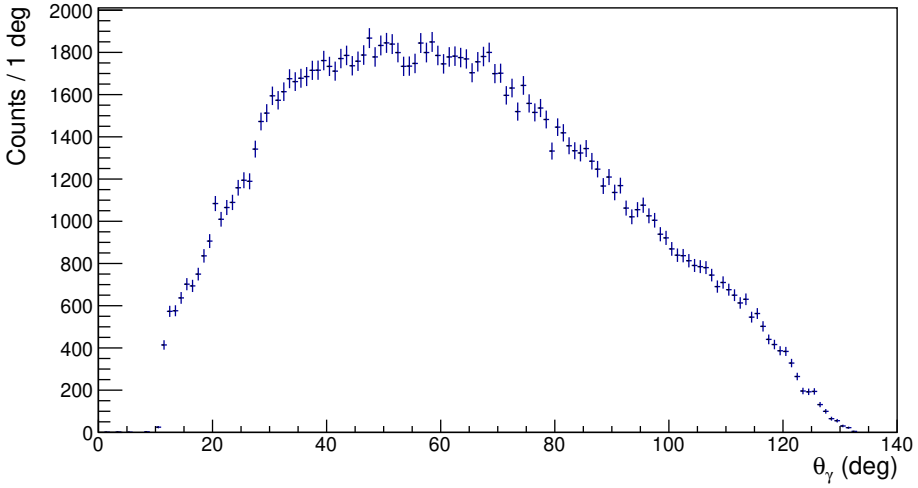

FIG. 45: Photon polar angle distribution for $K^+\Sigma^0$ t-channel MC.

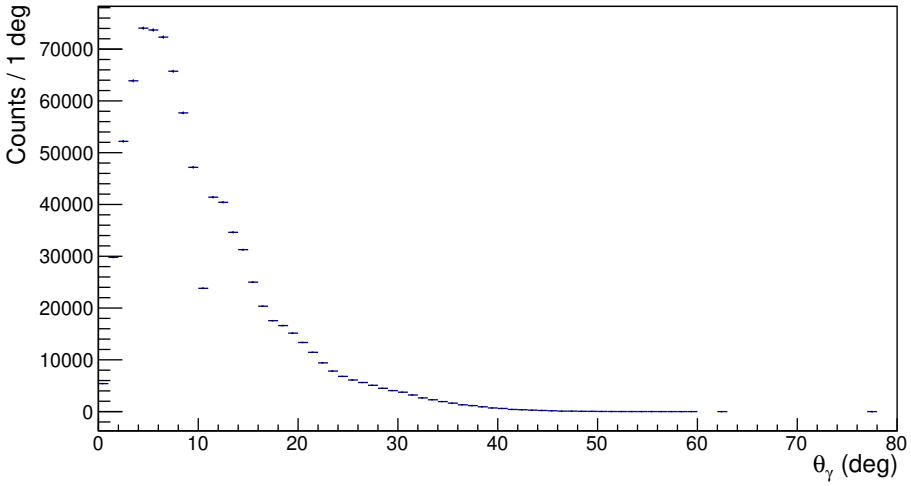

FIG. 46: Photon polar angle distribution for $K^+\Sigma^0$ u-channel MC.

In addition to this, the effect of the shower quality > 0.5 cut on Σ^0 yield was also investigated using MC. This is shown in Fig. 47. It appears that there is almost no effect on the t-channel Σ^0 events. For the u-channel, the fraction of signal events lost is negligible, on the order of a few percent as one can see from Fig. 48 .

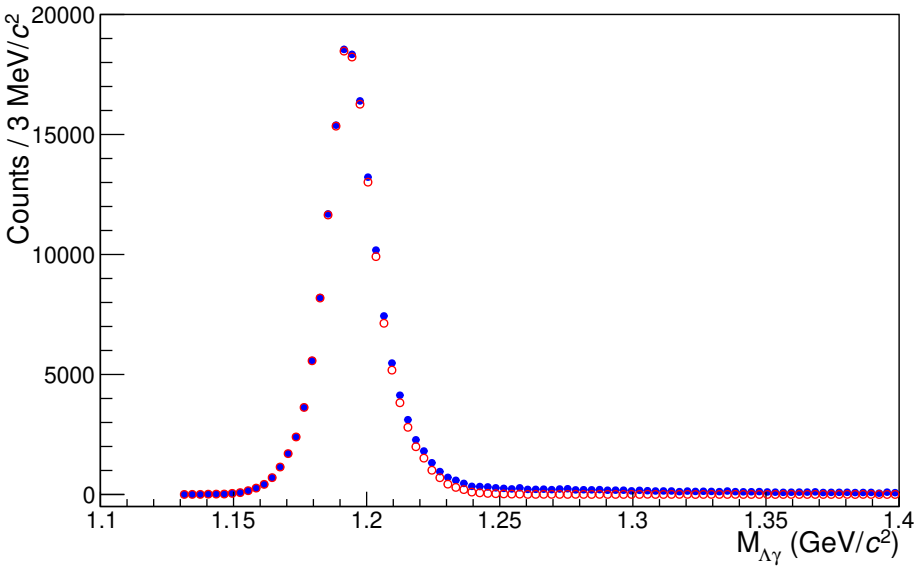

FIG. 47: Comparison of $K^+\Sigma^0$ t-channel yield before (blue solid circles) and after (red open circles) shower quality > 0.5 cut (MC).

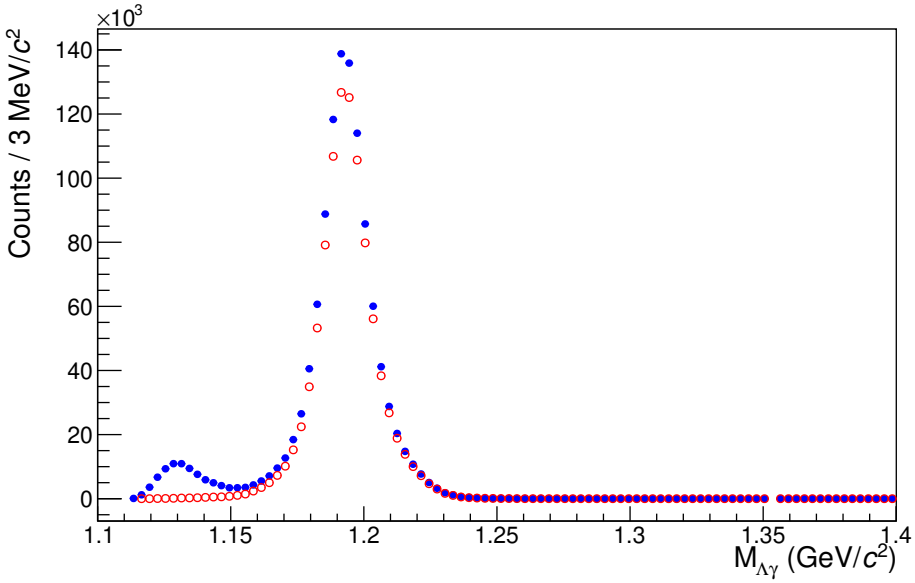

FIG. 48: Comparison of $K^+\Sigma^0$ u-channel yield before (blue solid circles) and after (red open circles) shower quality > 0.5 cut (MC).

Figure 49 shows the $-t$ distribution after all the cuts for events selected within range

of 1.169 GeV/c^2 < $M_{\Lambda\gamma}$ < 1.217 GeV/c^2. Figure 50 shows the $-u$ distribution with the same cuts. The two peaks in low and high $-t(-u)$ regions suggest both t and u-channel contributions for the reaction. Here, Mandelstam variables t and u were calculated using four-momenta of particles in the following way.
$t = (p_{beam} - p_{K^+})^2$ and $u = (p_{target} - p_{K^+})^2$.

From Fig. 50, we see that there are few events with $-u < 0$. This is physically possible if the mass is transferred along with momentum, in particular, if a proton is replaced by a lighter kaon. It was decided to keep these events for beam asymmetry analysis in the u-channel.

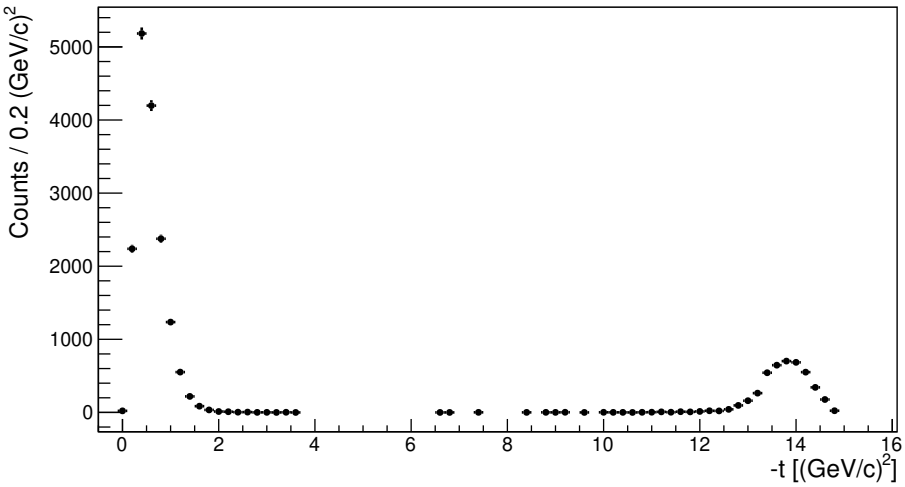

FIG. 49: $K^+\Sigma^0$ $-t$ distribution after all the cuts.

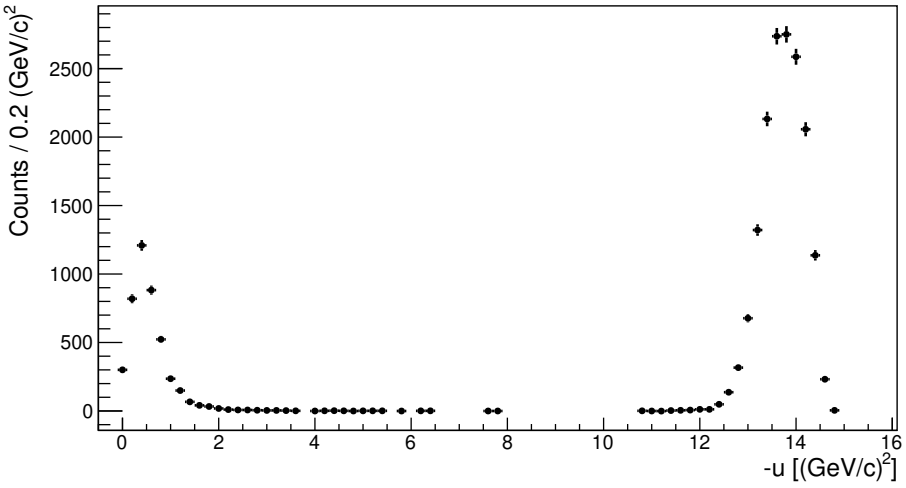

FIG. 50: $K^+\Sigma^0$ $-u$ distribution after all the cuts.

In order to understand the large gap between events in the low $-t$ and $-u$ regions, a MC sample was generated with a very flat t slope of 0.01 $(\mathrm{GeV}/c)^{-2}$ and the acceptance was found in the entire range of t between 0 and 16 $(\mathrm{GeV}/c)^2$. Figure 51 shows the thrown and accepted $-t$ distributions for this case and Fig. 52 shows the corresponding acceptance. The acceptances for low $|t|$ and low $|u|$ regions were also found using simulations with corresponding $t(u)$ slopes and are shown in Appendix D.2.

The acceptance was calculated as:

$$\text{Acceptance} = \frac{\text{Number of reconstructed events}}{\text{Number of generated events}} \tag{37}$$

It can be seen that the acceptance is very low (by 3 orders of magnitude) in the mid $-t$ region between low $-t$ and $-u$ regions leading to the gap observed in the distribution in data.

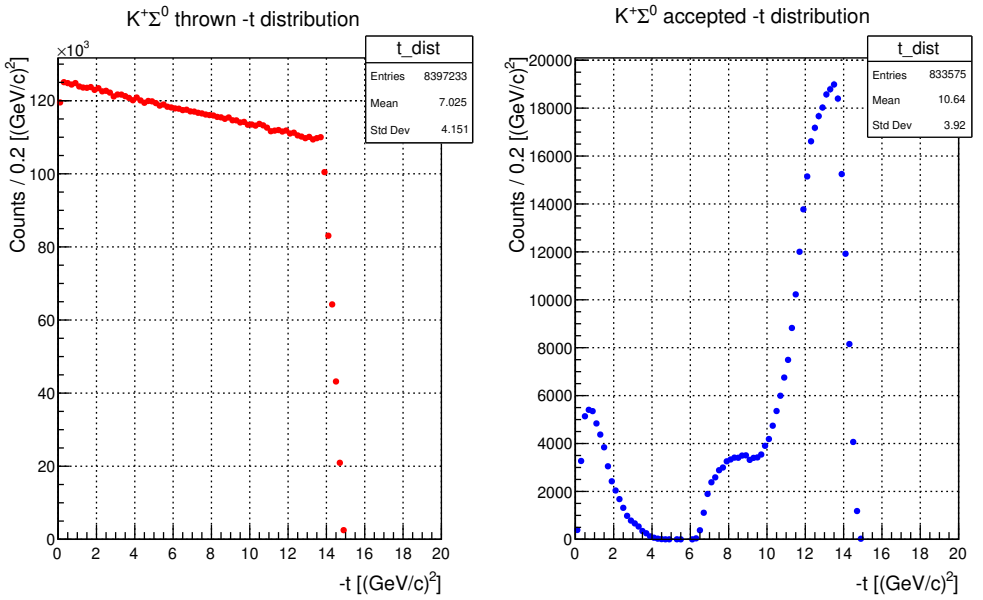

FIG. 51: $K^+\Sigma^0$ thrown (left) and accepted (right) -t distributions for a t-slope of 0.01 $(\mathrm{GeV}/c)^{-2}$.

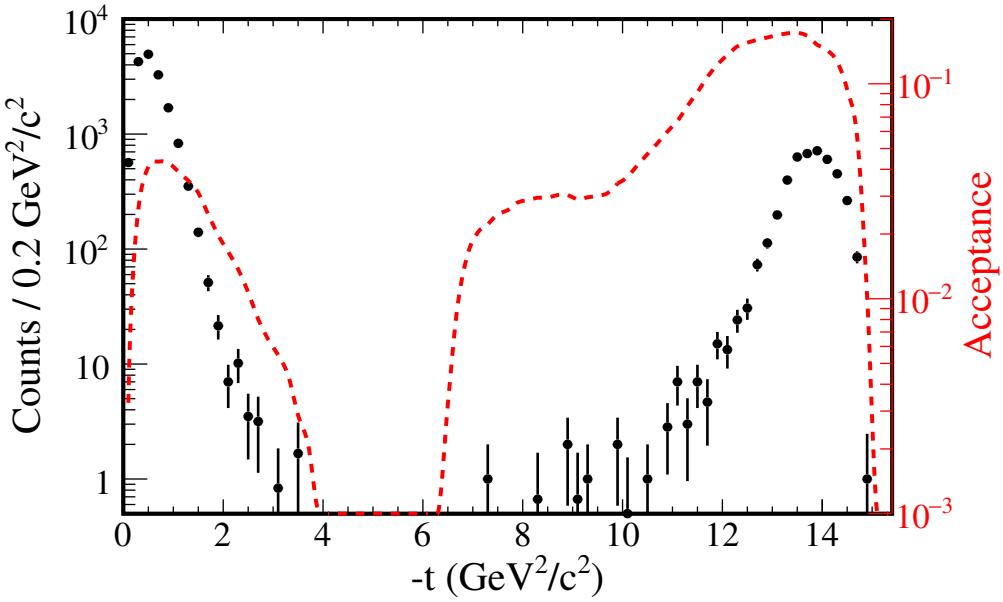

FIG. 52: Acceptance for the events from MC with t-slope of 0.01 $(\mathrm{GeV}/c)^{-2}$ (red, dashed line), $-t$ distribution from data is shown by solid circles.

4.2.3 ACCIDENTAL SUBTRACTION

The contribution of accidentally tagged beam photons to the yield was introduced in Sec. 4.2.2. As shown in Fig. 30, a sample of accidentally tagged combos with 6.012 ns$< |\Delta t| <$ 18.036 ns was used to estimate this contribution to the K^+ ϕ distributions used in the beam asymmetry analysis. The accidental distributions were scaled by a factor of 1/6 because they contain 6 accidental RF bunches. Then, they were subtracted from the distribution for main RF bunch.

4.2.4 NUMBER OF COMBINATIONS PER EVENT

In GlueX reconstruction there are more than one combination for an event. This is done to prevent the efficiency from getting too low. But after all the cuts in the analysis, number of combinations per event should be close to 1 (Exactly 1.0 is the ideal case) which means majority of combos are for true signal. So the following was done to estimate the number of combinations per event.

Figure 53 shows the number of events that was in the TTree after the full event selection. Figure 54 shows the number of combinations for "IsComboCut" was flagged as true (1) or not (0). The combinations which survive the event selection are those with flag=0. Combinations with different beam photons were excluded by selecting combinations only in the primary beam bunch.

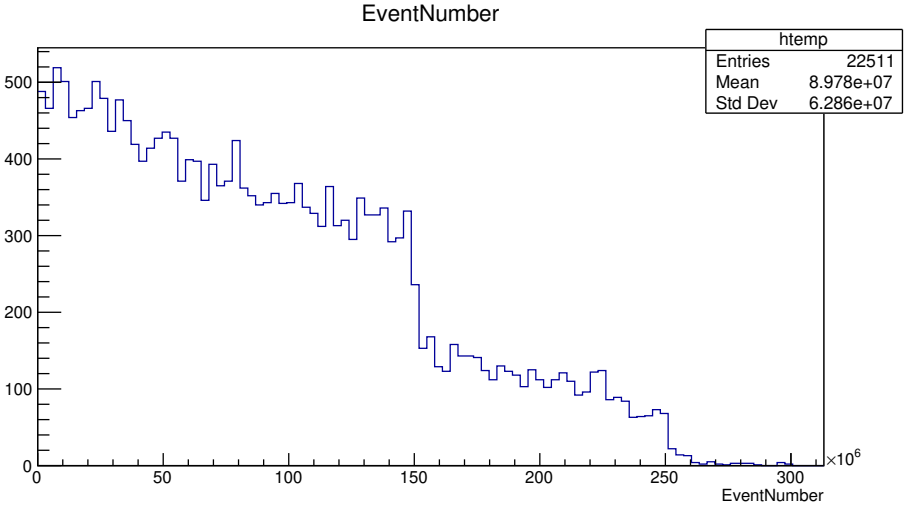

FIG. 53: The number of events after the full event selection.

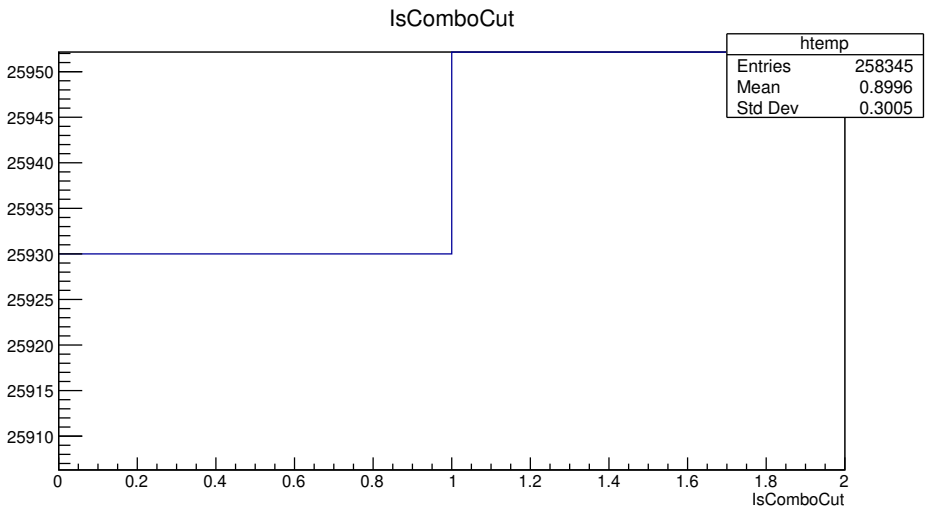

FIG. 54: Combinations that were flagged as cut or uncut.

Then, number of surviving combos per event is,

$$\frac{\text{combos not cut}}{\text{number of events}} = \frac{25930}{22511} = 1.15 \tag{38}$$

4.2.5 BACKGROUND UNDER THE SIGNAL PEAK

In Sec. 4.2.2, it was mentioned that there is some background under the Λ peak in the $M_{\pi^- p}$ spectrum (Fig. 37). This should be accounted for while doing the beam asymmetry analysis. Figure 55 shows the invariant mass of $\pi^- p\gamma$ vs that of $\pi^- p$. Figure 56 shows the $M_{\pi^- p}$ spectrum for events within the range of 1.169 GeV/c^2 $< M_{\pi^- p\gamma} <$ 1.217 GeV/c^2. As one can see the Λ peak has no background and only the 2% background under the Σ^0 peak was considered while estimating the beam asymmetry from background as described in Sec. 5.5.7.

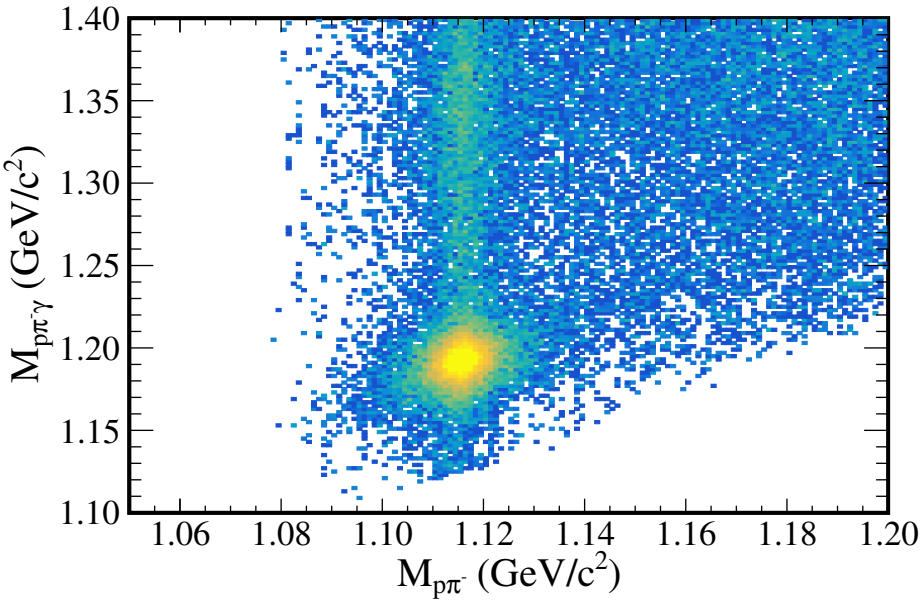

FIG. 55: Invariant mass of $\pi^- p\gamma$ vs invariant mass of $\pi^- p$ (data).

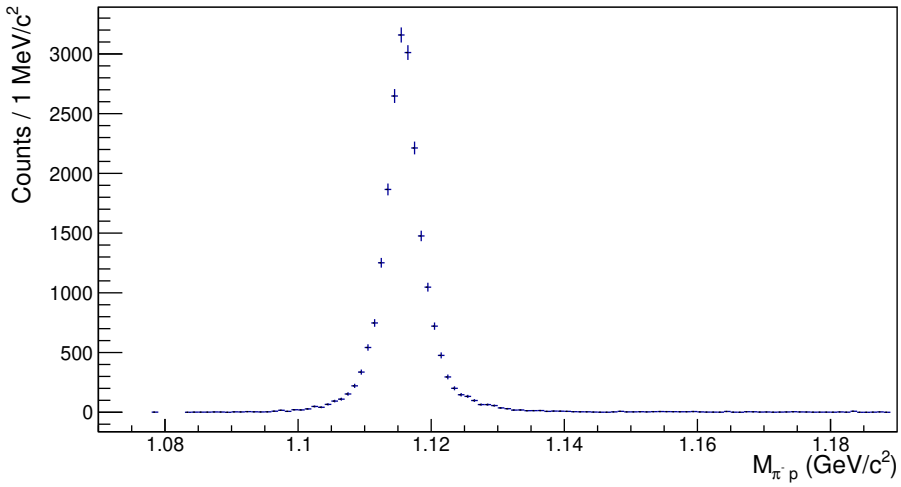

FIG. 56: Invariant mass of $\pi^- p$ within the Σ^0 region (data).

CHAPTER 5

BEAM ASYMMETRY MEASUREMENT (t-CHANNEL)

5.1 BEAM ASYMMETRY METHOD

For the photoproduction of psuedoscalar mesons using a linearly polarized photon beam and an unpolarized target, the polarized cross section is given by,

$$\sigma_{pol}(\phi, \phi_{lin}) = \sigma_{unpol}[1 - P_\gamma \Sigma \cos(2(\phi - \phi_{lin}))]. \tag{39}$$

Where σ_{unpol} is the unpolarized cross section, ϕ is the angle between plane parallel to the lab floor and K^+ production plane. It is equivalent to the azimuthal angle of K^+ in the lab frame. The magnitude of the photon beam polarization is given by P_γ. Figure 57 shows the relevant angles in the lab frame.

The beam asymmetry Σ is a measure of the difference between cross sections with two mutually perpendicular polarizations.

$$\Sigma = \frac{\sigma_\perp - \sigma_\parallel}{\sigma_\perp + \sigma_\parallel} \tag{40}$$

Where $\sigma_\perp$ and $\sigma_\parallel$ are cross sections for the two mutually perpendicular polarization directions which we call "PERP" and "PARA". PARA is normally taken to be when the polarization plane of the beam is parallel(0°) to the lab floor ($x - z$ plane) and PERP when it is perpendicular(90°). Another set with PARA=-45° and PERP=45° is chosen to allow an independent check of systematics for the two sets.

Cross sections for each orientation can be found using the following relations:

$$\sigma_\parallel(\phi) = \sigma_{pol}(\phi, \phi_{lin} = 0) = \sigma_{unpol}(1 - P_\parallel \Sigma \cos 2\phi), \tag{41}$$

$$\sigma_\perp(\phi) = \sigma_{pol}(\phi, \phi_{lin} = 90) = \sigma_{unpol}(1 + P_\perp \Sigma \cos 2\phi). \tag{42}$$

Here $P_\parallel$ and $P_\perp$ are the magnitude of the photon beam polarization in the PARA and PERP orientations, respectively.

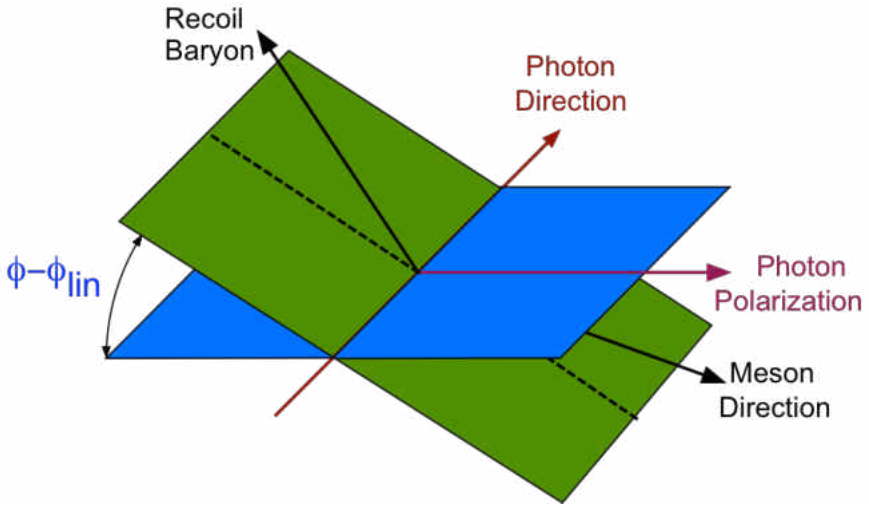

FIG. 57: Illustration of the angles used for the beam asymmetry analysis in the lab frame. Figure from Ref. [44].

The event yield in each orientation is given by

$$Y_{\parallel}(\phi) \sim N_{\parallel}\left[\sigma_{unpol}A(\phi)\left(1 - P_{\parallel}\Sigma\cos 2\phi\right)\right], \tag{43}$$

$$Y_{\perp}(\phi) \sim N_{\perp}\left[\sigma_{unpol}A(\phi)\left(1 + P_{\perp}\Sigma\cos 2\phi\right)\right] \tag{44}$$

where:

- $A(\phi)$ is an arbitrary function for the ϕ-dependent detector acceptance and efficiency,
- $N_{\perp(\parallel)}$ is the flux of photons in the PERP (PARA) orientation.

If there is no background, a polarization-dependent yield asymmetry $S(\phi)$ can be defined as

$$S(\phi) = \frac{Y(\phi)_{\perp} - F_R Y(\phi)_{\parallel}}{Y(\phi)_{\perp} + F_R Y(\phi)_{\parallel}} = \frac{\sigma(\phi)_{\perp}A(\phi) - \sigma(\phi)_{\parallel}A(\phi)}{\sigma(\phi)_{\perp}A(\phi) + \sigma(\phi)_{\parallel}A(\phi)}. \tag{45}$$

The ϕ-dependent acceptance, $A(\phi)$ cancels if it is the same for both PARA and PERP modes. $F_R = \frac{N_{\perp}}{N_{\parallel}}$ is the ratio of the integrated photon flux for PERP and PARA for a given data set. Then, measured yield asymmetry can be fit by the following function [45]

$$f(\phi) = \frac{(P_{\perp} + P_{\parallel})\Sigma\cos 2(\phi - \phi_0)}{2 + (P_{\perp} - P_{\parallel})\Sigma\cos 2(\phi - \phi_0)}. \tag{46}$$

A phase shift ϕ_0 was added to allow for the misalignment of polarization of the beam and will be discussed in Sec. 5.3. Measurements of $P_\perp$ and $P_\parallel$ are found using TPOL data as mentioned in Sec. 3.1.4. Then, from the only fit parameter, beam asymmetry Σ can be obtained.

5.2 RELATIVE FLUX NORMALIZATION

Using the PS hits in coincidence with a hit in the TAGM or TAGH, the integrated photon flux was determined. As explained in Sec. 4.2.3, accidentally tagged photons were subtracted. Here Δt is the time difference between the PS pair and the tagger hit. The ratio of tagged flux for PARA and PERP data sets in the beam energy range $8.2 < E_\gamma < 8.8$ GeV is shown in Table 4.

Data Set	PARA Integrated Flux	PERP Integrated Flux	F_R
0/90	4.18800×10^{12}	4.34682×10^{12}	1.03792
-45/45	4.09501×10^{12}	4.07606×10^{12}	0.99537

TABLE 4: Flux normalization ratios (F_R) for different polarization directions.

5.3 EXAMPLE FIT TO THE Σ^0 SAMPLE (t-CHANNEL)

Using the relative flux ratio, the ϕ-dependent yields were fit to extract the Σ beam asymmetry. A set of example fits is shown in Figs. 58 and 59 for the Σ^0 event sample integrated over the entire t region used for this analysis ($0.1\ (\mathrm{GeV}/c)^2 < -t < 1.4\ (\mathrm{GeV}/c)^2$). The upper plots are fits to the PARA (left) and PERP (right) yields independently. There are two free parameters in these fits of the form

$$f(\phi) = C[1 + P\Sigma\cos(2(\phi - \phi_0))] \tag{47}$$

with $p_0 = C$ for normalization and $p_1 = P\Sigma$.

The phase constant ϕ_0 allows for the PARA (PERP) polarization plane orientation to not be exactly parallel to the $x-z$ ($x-y$) plane in the lab. Phase constants were obtained from a study of $\rho(770)$ decay asymmetries and are given in Table 5 [46]. The value $\phi_0 = 3.13^\circ$ was used for fitting yield asymmetry in each individual bins of $-t$ for 0/90 data set. The value $\phi_0 = 3.16^\circ$ was used for fitting the yield asymmetry in the -45/45 data set.

Nominal ϕ	ϕ_0	statistical	systematic
0°	1.77	±0.04	±0.56
90°	4.50	±0.04	±0.50
Asymmetry	3.13	±0.03	±0.14
45°	2.85	±0.05	±0.53
-45°	3.43	±0.04	±0.59
Asymmetry	3.16	±0.03	±0.17

TABLE 5: Deviation of polarization plane orientation with uncertainties.

The lower left plot in Fig. 58 is a fit to the normalized yield asymmetry $S(\phi)$ (Eqn. 45) according to the fit function in Eqn. 46.

The fit results for the two beam orientation sets in the individual $-t$ bins are shown in Appendix C.1. The lower right plot in Fig. 58 is relevant for understanding of the impact of instrumental asymmetries and is discussed in Sec. 5.5.2.

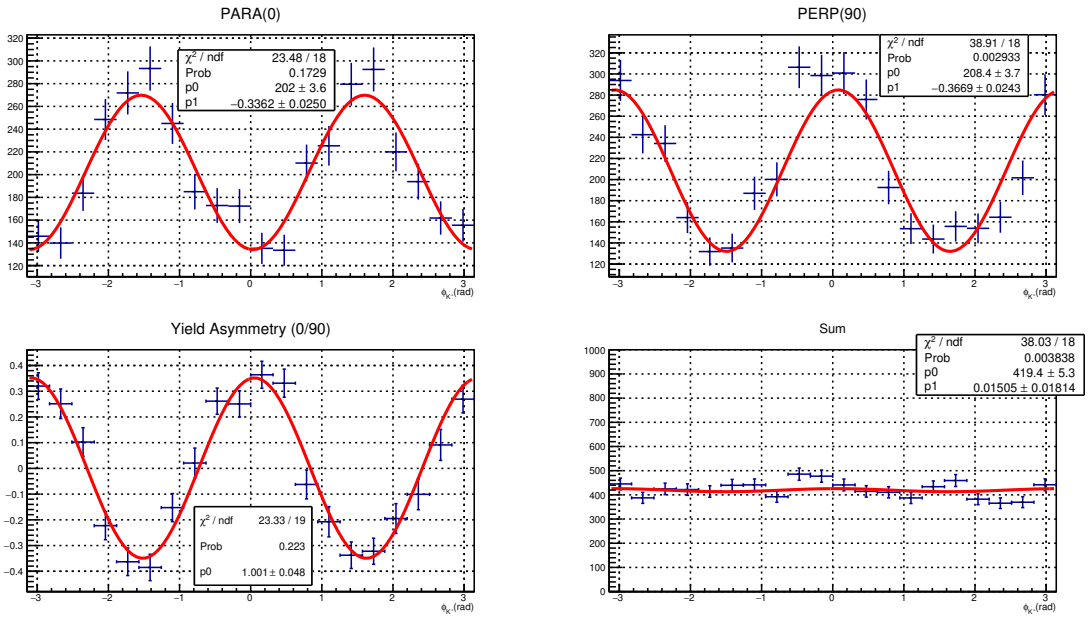

FIG. 58: Polarization direction set to 0/90. Fits to the ϕ distributions in the beam energy range $8.2 < E_\gamma < 8.8$ GeV, integrated over the entire t range. Upper row: fits to the PARA (left) and PERP (right) distributions independently. Lower row (left): fit to the asymmetry (Eqn. 45). Lower row (right): fit to the sum $Y(\phi)_\perp + F_R Y(\phi)_\parallel$, which is sensitive to instrumental asymmetries.

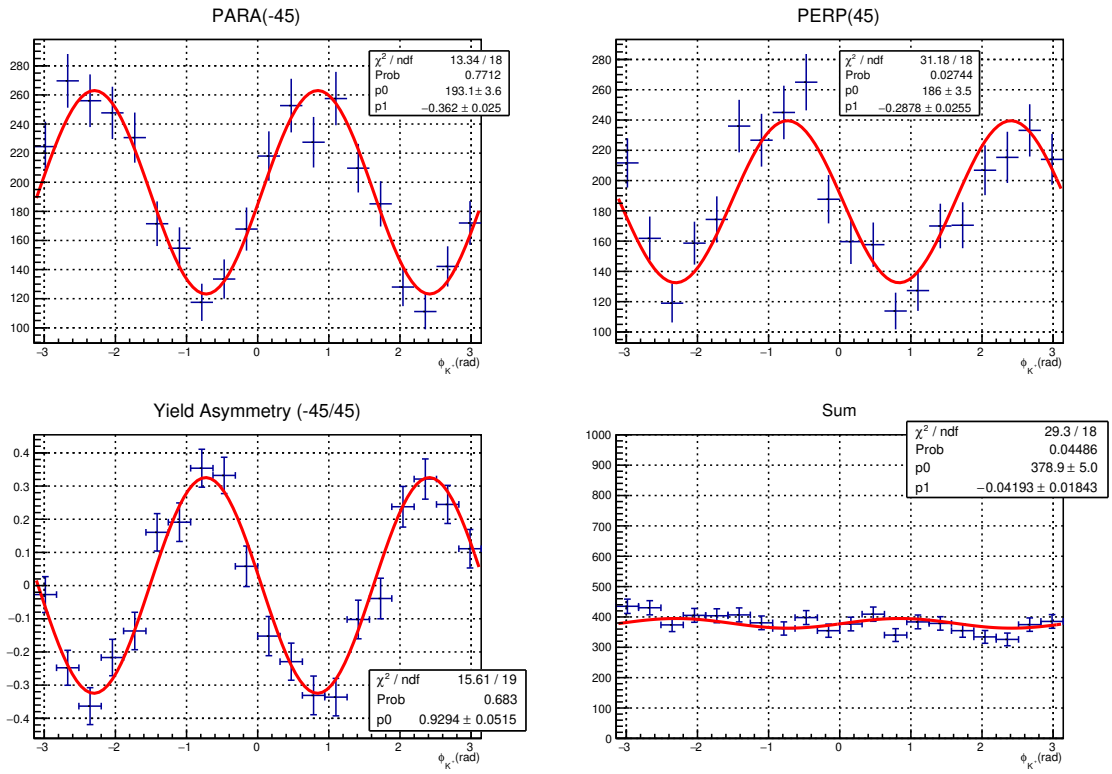

FIG. 59: Polarization direction set to -45/45. Fits to the ϕ distributions in the beam energy range $8.2 < E_\gamma < 8.8$ GeV, integrated over the entire t range. Upper row: fits to the PARA (left) and PERP (right) distributions independently. Lower row (left): fit to the asymmetry (Eqn. 45). Lower row (right): fit to the sum $Y(\phi)_\perp + F_R Y(\phi)_\parallel$, which is sensitive to instrumental asymmetries.

5.4 SUMMARY OF FIT RESULTS

Figure 60 shows the beam asymmetry results obtained from fitting the yield asymmetry histograms for individual $-t$ bins.

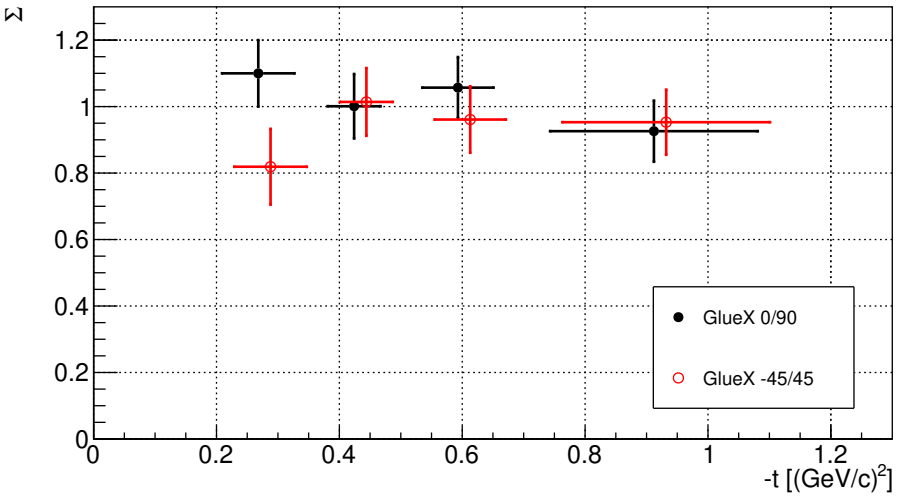

FIG. 60: The beam asymmetry Σ for $\gamma p \to K^+\Sigma^0$ in the t channel. The black solid circles correspond to polarization direction set to 0/90, red open circles correspond to polarization direction set to -45/45 ($-t$ coordinates are shifted by 0.02 $(\mathrm{GeV}/c)^2$ to the right for clarity). Vertical error bars represent statistical uncertainties while horizontal error bars are drawn to indicate the RMS widths of $-t$ bins used.

5.5 SYSTEMATIC STUDIES

5.5.1 EVENT SELECTION

By varying the parameters of the event selection described in Sec 4.2.2, the systematic dependence of the asymmetry on the event selection criteria was studied. The list of nominal cuts and the looser and tighter cuts that were used for this purpose are given in Table 6. For each variation of the cut, the asymmetry was extracted in bins of $-t$.

Figures 61 and 62 show the values of the asymmetry as a function of $-t$, where each parameter is represented by an individual color and two marker shapes for tighter and looser cuts. The asymmetry for the default cut parameters is shown by the open black circles.

Looser Cut	Nominal Cut	Tighter Cut
50.9 cm $< z <$ 79.1 cm	51.2 cm $< z <$ 78.8 cm	51.5 cm $< z <$ 78.5 cm
$r <$ 1.2 cm	$r <$ 1.0 cm	$r <$ 0.8 cm
$\lvert MM^2 \rvert < 0.1\,\mathrm{GeV}^2$	$\lvert MM^2 \rvert < 0.08\,\mathrm{GeV}^2$	$\lvert MM^2 \rvert < 0.06\,\mathrm{GeV}^2$
CL $> 10^{-5}$	CL $> 10^{-4}$	CL $> 10^{-3}$
$\lvert M_{\pi^- p} - M_\Lambda \rvert <$ 0.012 GeV	$\lvert M_{\pi^- p} - M_\Lambda \rvert <$ 0.009 GeV	$\lvert M_{\pi^- p} - M_\Lambda \rvert <$ 0.006 GeV
$\lvert M_{\Lambda\gamma} - M_{\Sigma^0} \rvert <$ 0.032 GeV	$\lvert M_{\Lambda\gamma} - M_{\Sigma^0} \rvert <$ 0.024 GeV	$\lvert M_{\Lambda\gamma} - M_{\Sigma^0} \rvert <$ 0.016 GeV
shower quality > 0.3	shower quality > 0.5	shower quality > 0.7

TABLE 6: Variation of the event selection cut parameters to study systematic impact on the asymmetry.

All the data points associated with cut systematics are within the 1σ statistical error of the nominal data points. Colors for different cut variations are as shown in Fig. 63.

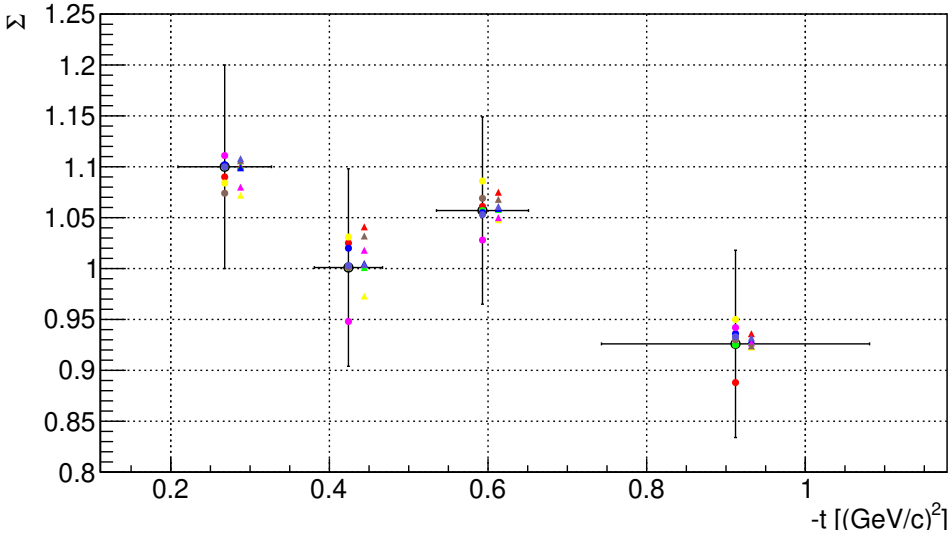

FIG. 61: Σ asymmetry measured for each of the cut parameter variations, shown as different colored points in each $-t$ bin for the 0/90 orientation. Full circles represent tighter cuts and triangles represent looser cuts. The open circles and vertical error bars are the asymmetry values and statistical errors using the nominal cut parameters.

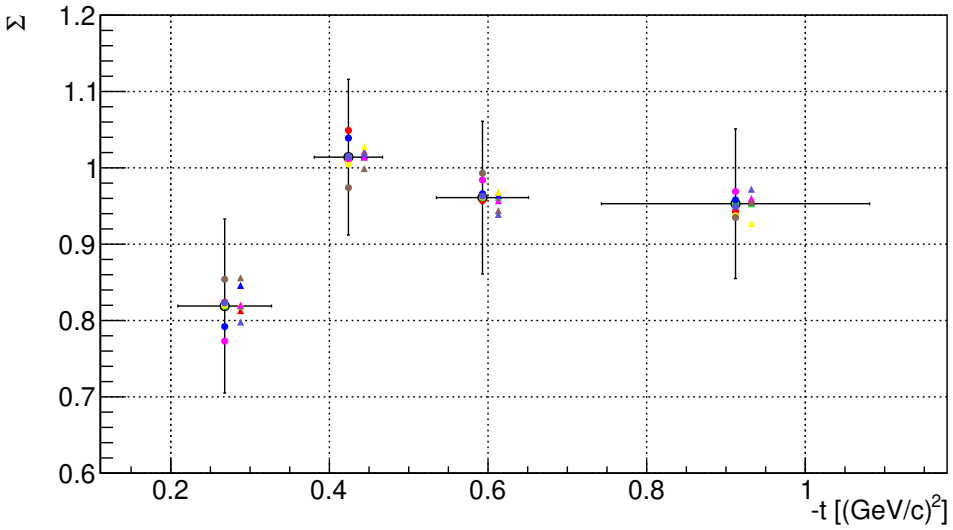

FIG. 62: Σ asymmetry measured for each of the cut parameter variations, shown as different colored points in each $-t$ bin for the -45/45 orientation. Full circles represent tighter cuts and triangles represent looser cuts. The open circles and vertical error bars are the asymmetry values and statistical errors using the nominal cut parameters.

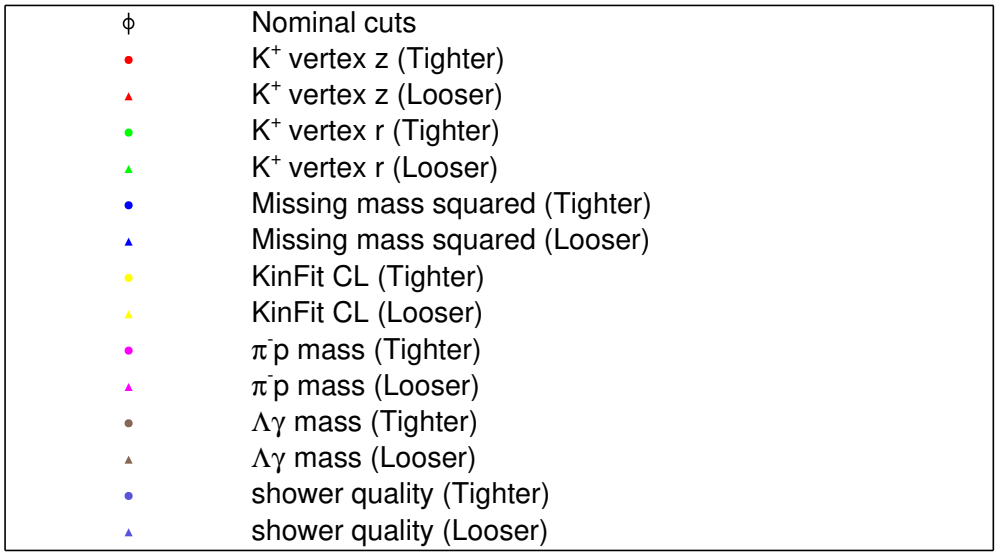

FIG. 63: Legend for cut systematics plots (Figs. 61 and 62).

Tables 7 and 8 give systematic uncertainties for each cut variation for 0/90 and -45/45 orientation sets. Here the uncertainty was calculated as the difference between asymmetry obtained from the cut variation and the nominal cut. For each cut variable, errors associated with looser and tighter values were averaged. Then, systematic uncertainties due to cuts were calculated by adding uncertainties due to each cut variable in quadrature. The total uncertainty due to the cut systematics is obtained as follows.

$$\delta_{CUTSYS} = \sqrt{\sum_{n=1}^{N} \delta_n^2}\,, \tag{48}$$

where δ_n is the average uncertainty of the cut variable 'n' and N is the number of cut variables.

Tables 9 and 10 give the calculated systematic uncertainties for 0/90 and -45/45 beam orientations respectively.

	-t $(\mathrm{GeV}/c)^2$			
cut variation	0.10-0.35	0.35-0.50	0.50-0.70	0.70-1.40
K^+ vertex z loose	0.001	0.040	0.018	0.010
K^+ vertex z tight	0.010	0.024	0.004	0.038
K^+ vertex r loose	0	0	0.001	0.002
K^+ vertex r tight	0	0	0	0.001
Missing mass squared loose	0.001	0.004	0.002	0.004
Missing mass squared tight	0.002	0.019	0.002	0.010
KinFit CL loose	0.028	0.028	0.009	0.003
KinFit CL tight	0.016	0.030	0.029	0.024
$M_{\pi^- p}$ loose	0.020	0.017	0.007	0.001
$M_{\pi^- p}$ tight	0.011	0.053	0.029	0.016
$M_{\Lambda\gamma}$ loose	0.006	0.031	0.011	0.002
$M_{\Lambda\gamma}$ tight	0.026	0	0.012	0.004
FCAL shower quality loose	0.008	0.003	0.004	0.006
FCAL shower quality tight	0	0.002	0.004	0.007

TABLE 7: Systematic uncertainty for each cut variation for individual $-t$ bins for 0/90 orientation.

	-t $(\mathrm{GeV}/c)^2$			
cut variation	0.10-0.35	0.35-0.50	0.50-0.70	0.70-1.40
K^+ vertex z loose	0.006	0.007	0.007	0.005
K^+ vertex z tight	0.005	0.035	0.004	0.010
K^+ vertex r loose	0	0	0	0
K^+ vertex r tight	0	0.003	0	0
Missing mass squared loose	0.027	0.002	0.003	0.002
Missing mass squared tight	0.027	0.025	0.005	0.005
KinFit CL loose	0.002	0.014	0.007	0.026
KinFit CL tight	0.001	0.009	0.001	0.016
$M_{\pi^- p}$ loose	0.001	0	0.004	0.007
$M_{\pi^- p}$ tight	0.046	0.002	0.023	0.016
$M_{\Lambda\gamma}$ loose	0.037	0.015	0.017	0.002
$M_{\Lambda\gamma}$ tight	0.035	0.040	0.032	0.018
FCAL shower quality loose	0.021	0.005	0.022	0.019
FCAL shower quality tight	0.004	0.001	0.002	0.004

TABLE 8: Systematic uncertainty for each cut variation for individual $-t$ bins for -45/45 orientation.

$-t$ bin $[(\mathrm{GeV/c})^2]$	Systematic uncertainty
$0.10 < -t < 0.35$	0.032
$0.35 < -t < 0.50$	0.059
$0.50 < -t < 0.70$	0.031
$0.70 < -t < 1.40$	0.031

TABLE 9: Cut dependence systematic uncertainty on Σ for individual $-t$ bins for 0/90 orientation.

$-t$ bin $[(\mathrm{GeV/c})^2]$	Systematic uncertainty
$0.10 < -t < 0.35$	0.053
$0.35 < -t < 0.50$	0.039
$0.50 < -t < 0.70$	0.031
$0.70 < -t < 1.40$	0.030

TABLE 10: Cut dependence systematic uncertainty on Σ for individual $-t$ bins for -45/45 orientation.

5.5.2 INSTRUMENTAL ASYMMETRY

Any instrumental asymmetries not canceled by the PERP - PARA subtraction described in Sec. 5.1 can be seen in the sum $Y_{\perp}(\phi) + F_R Y_{\parallel}(\phi)$. For every $-t$ bin, fits to the sum of yields were done using the functional form

$$f_{inst}(\phi) = C[1 + A_{inst} \cos 2(\phi - \phi_0)]. \tag{49}$$

There are two free parameters, $p_0 = C$ for normalization and $p_1 = A_{inst}$. The same value was used for the phase constant of the fit ϕ_0 as for the fits to the yield asymmetry $S(\phi)$. Figure 64 shows the measured instrumental asymmetries as a function of $-t$ from the fits to the sum of yields shown in Figs. 65 and 66. From the fits, we see that instrumental asymmetry is close to zero for both 0/90 and -45/45 modes. So, a systematic uncertainty will not be assigned due to the instrumental asymmetry. Additionally, a linear fit was done for the sum of yields to compare χ^2 values with that for cosine fit. Linear fits are shown in Figs. 67 and 68. Both type of fits seem to have similar χ^2 values.

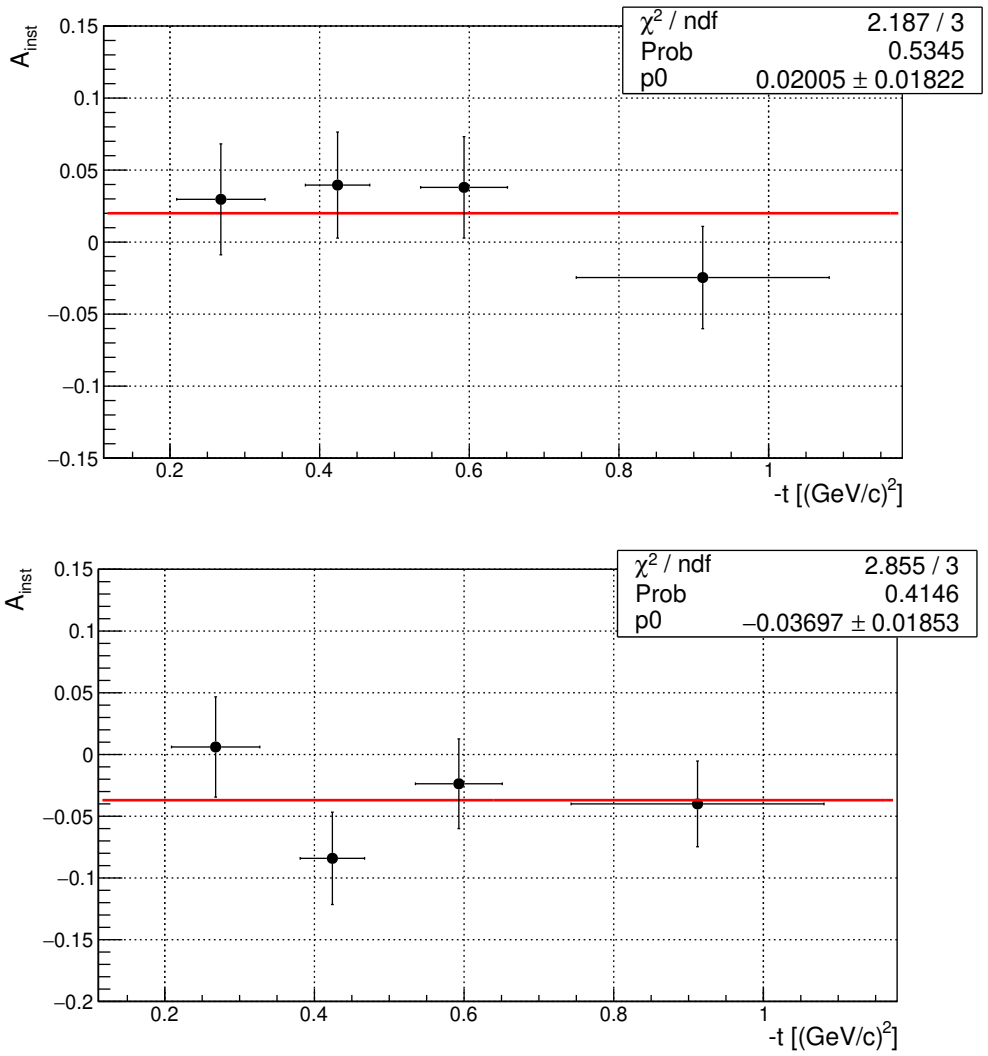

FIG. 64: Instrumental asymmetry for 0/90 orientation (top) and -45/45 orientation (bottom) as a function of $-t$.

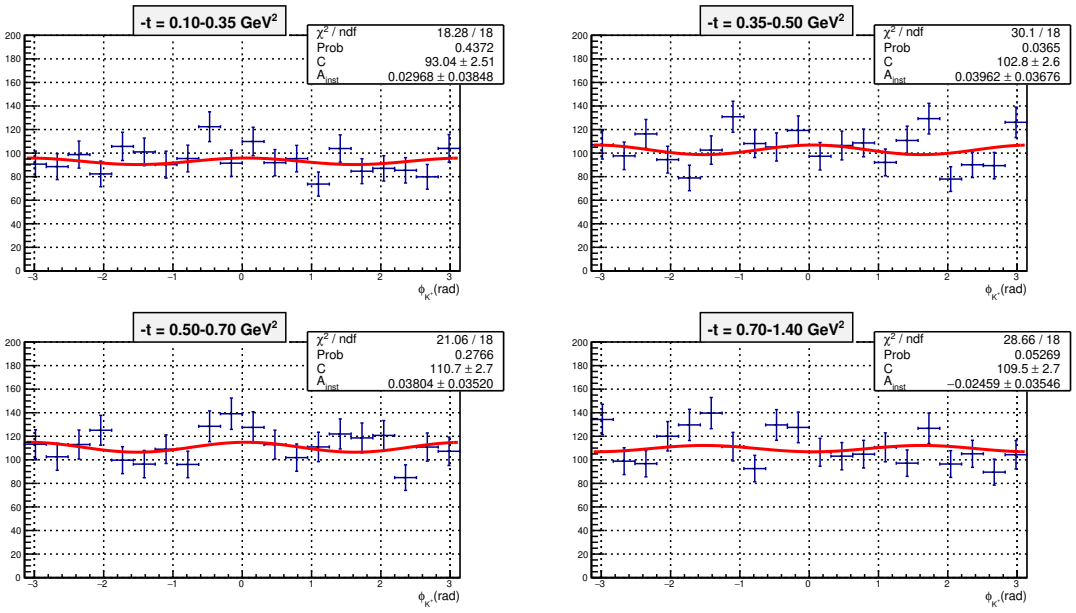

FIG. 65: Cosine fits to the sum $Y(\phi)_\perp + F_R Y(\phi)_\parallel$ for 0/90 orientation.

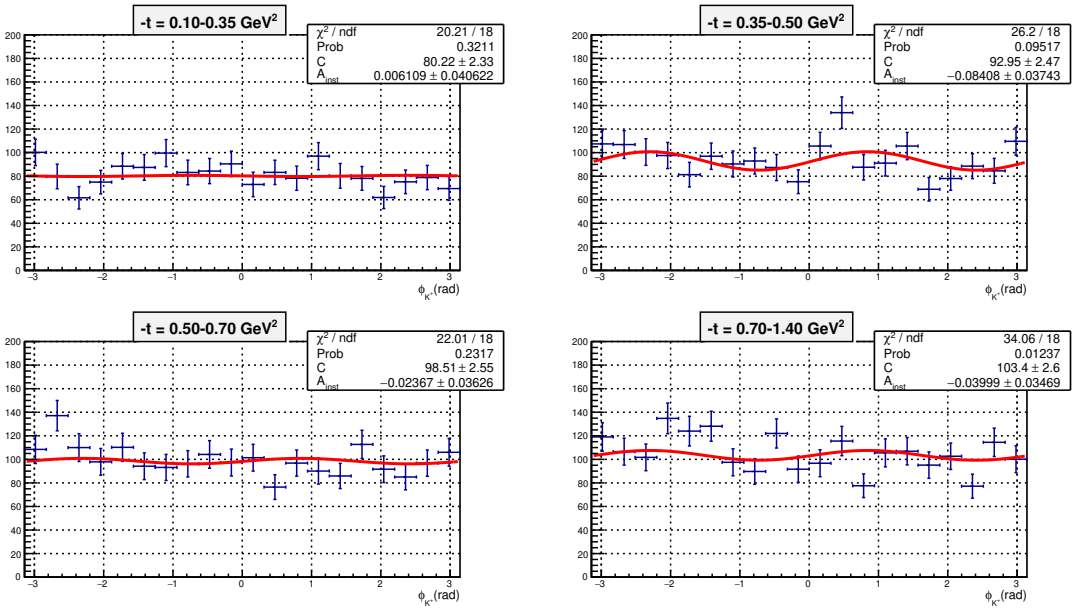

FIG. 66: Cosine fits to the sum $Y(\phi)_\perp + F_R Y(\phi)_\parallel$ for -45/45 orientation.

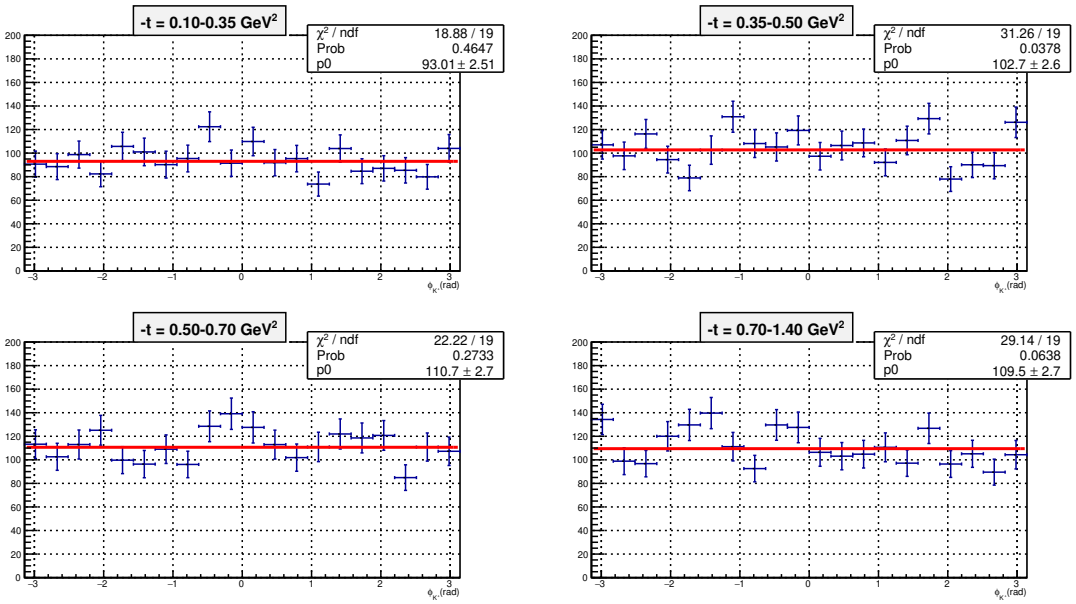

FIG. 67: Linear fits to the sum $Y(\phi)_{\perp} + F_R Y(\phi)_{\parallel}$ for 0/90 orientation.

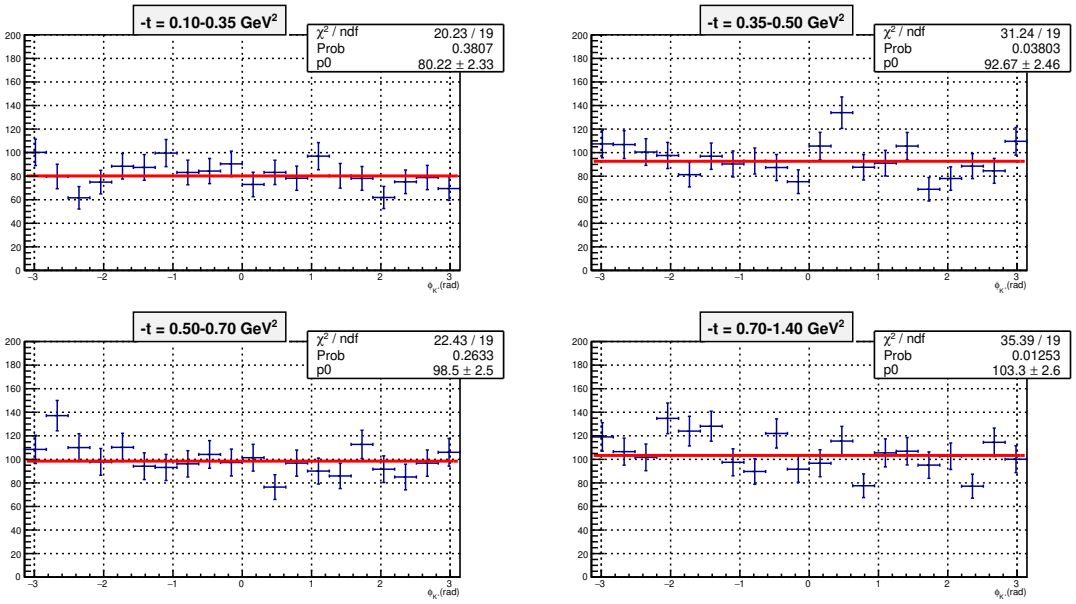

FIG. 68: Linear fits to the sum $Y(\phi)_{\perp} + F_R Y(\phi)_{\parallel}$ for -45/45 orientation.

5.5.3 PHASE DEPENDENCE

While extracting beam asymmetry values, we chose to fix the phase parameter ϕ_0 in the fits to the yield asymmetry for all $-t$ bins. The linear polarization axis cannot change with $-t$. But, any sensitivity to fixing of this phase is studied with fitting the yield asymmetry allowing phase constant to be a free parameter. Figures 69 and 70 show yield asymmetry plots with phase parameter being free. Figure 71 shows the measured asymmetry values along with the nominal results.

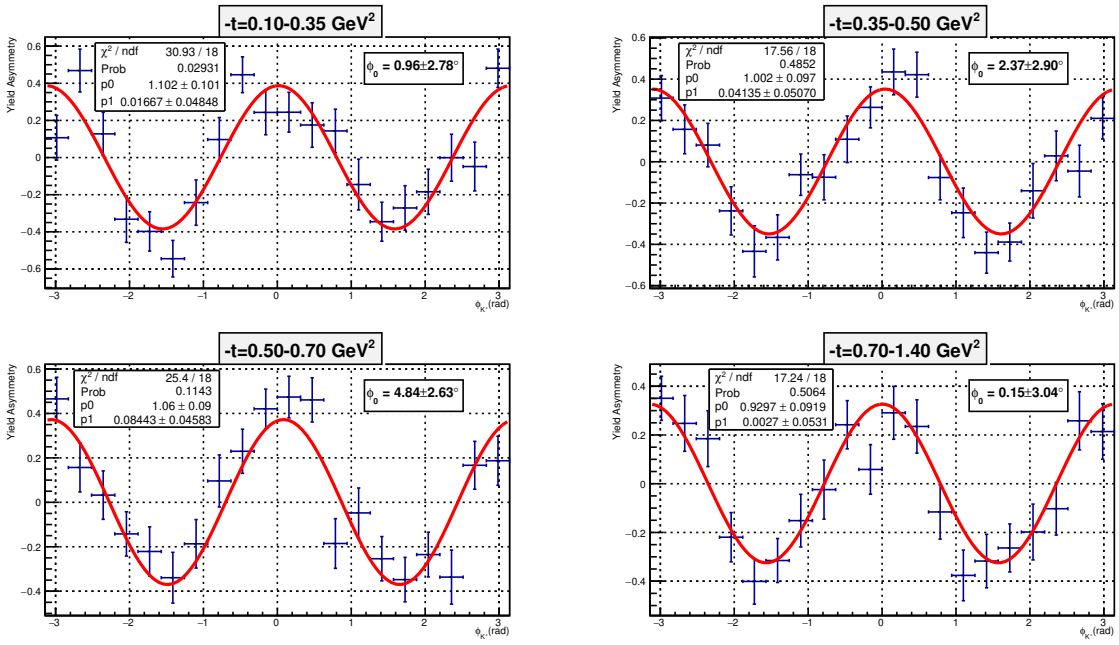

FIG. 69: Yield asymmetry plots for allowing the phase to be a free parameter in the fit for 0/90 orientation. The ϕ_0 values on which fits converge are given in the text boxes inside plots.

Using the standard deviation of histograms for differences between floating ϕ_0 fit asymmetries and nominal asymmetries, a systematic error of 0.11% was assigned to 0/90 orientation and an error of 0.70% was assigned to -45/45 orientation.

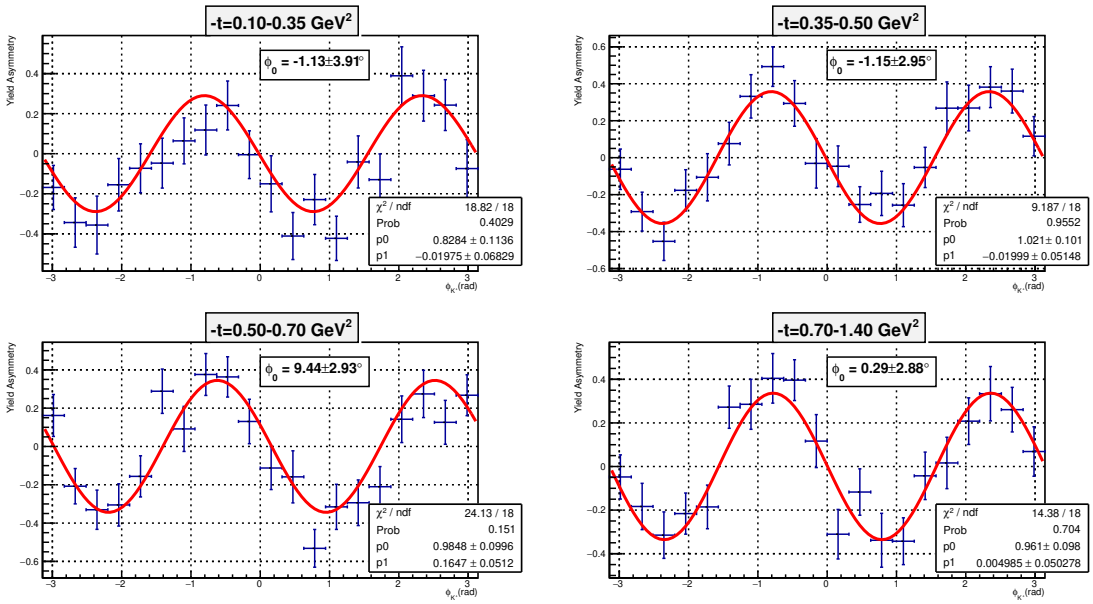

FIG. 70: Yield asymmetry plots for allowing the phase to be a free parameter in the fit for -45/45 orientation. The ϕ_0 values on which fits converge are given in the text boxes inside plots.

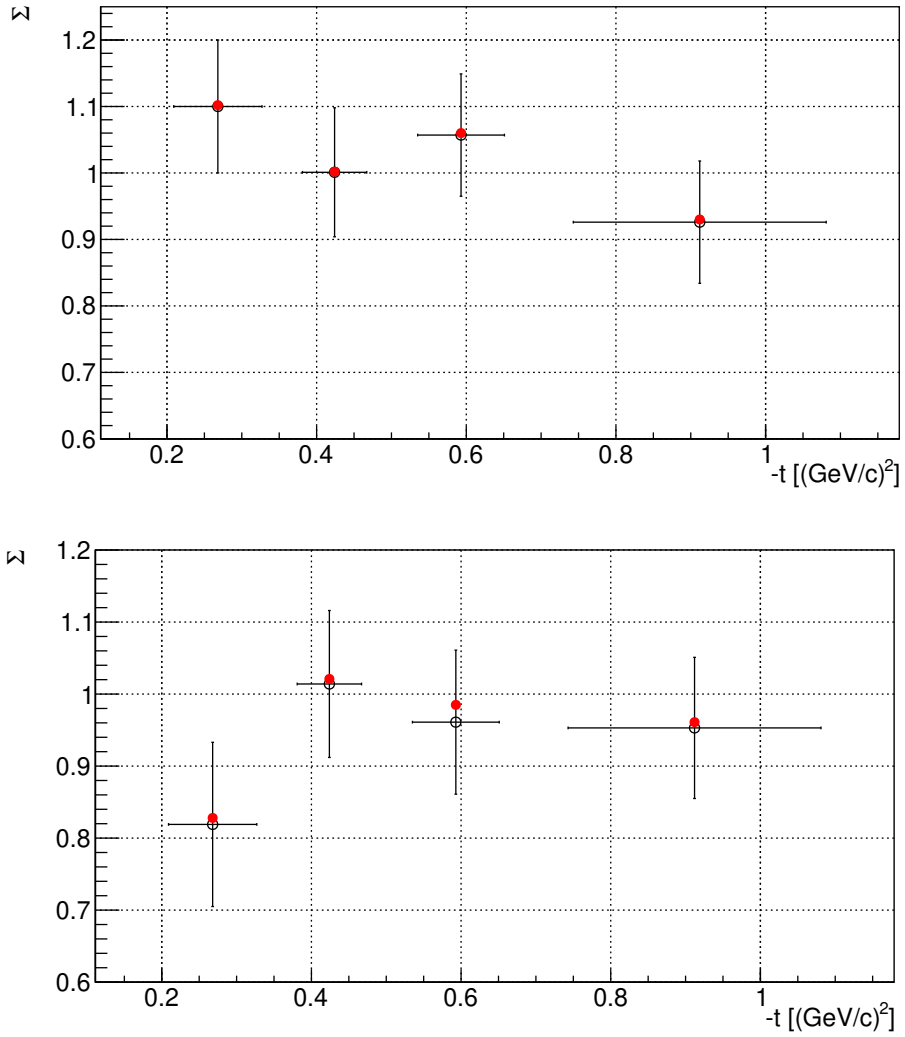

FIG. 71: Σ asymmetry measured while allowing the phase to be a free parameter in the fit (red closed point) in the 0/90 orientation (top) and -45/45 orientation (bottom). The open black circles and error bars are the asymmetry values and statistical errors using the fixed phase.

5.5.4 FLUX NORMALIZATION DEPENDENCE

To estimate the sensitivity of the measured Σ values to the flux normalization determined by PS yields, asymmetries were measured again by changing the nominal flux ratio by $\pm 5\%$. The measured asymmetries with the varied flux normalization are shown in Fig. 72. The deviations of the red and blue points from the nominal asymmetry values were computed for all $-t$ bins and standard deviations of histograms were taken as the systematic uncertainty of the flux normalization. The average deviation for the 0/90 orientation is 0.002 while the maximum deviation is 0.011. The average deviation for the -45/45 orientation is 0.002 while the maximum deviation is 0.008. A systematic error of 0.496% was assigned to the 0/90 orientation and an error of 0.38% was assigned to the -45/45 orientation respectively.

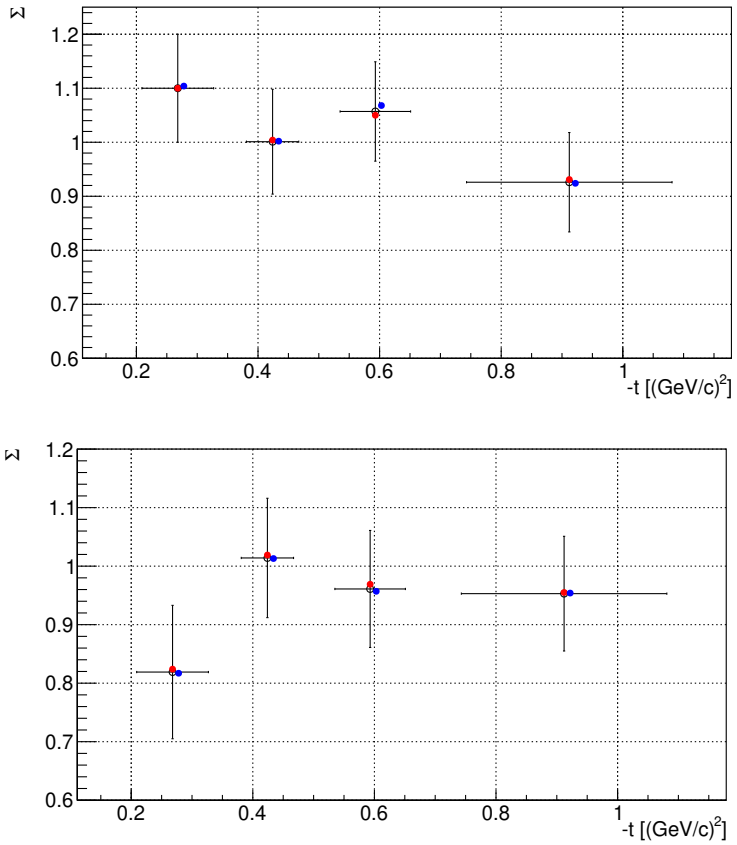

FIG. 72: Σ asymmetry measured after changing flux normalization by $\pm 5\%$ (red closed points for +5% and blue closed points for -5%) in the 0/90 (top) and -45/45 (bottom) orientations. The open circles and error bars are the asymmetry values and statistical errors using the nominal flux normalization.

5.5.5 FINITE ϕ BIN SIZE DEPENDENCE

The effect of the bin width of ϕ distribution was studied analytically based on the method of Ref. [47]. The correction function to the binned data is defined as (using Table 1 of Ref. [47])

$$R = \frac{\frac{1}{2}\alpha\Delta}{\sin\frac{1}{2}\alpha\Delta}. \tag{50}$$

where $\alpha = 2$ and $\Delta = \frac{2\pi}{20}$ is the bin width used in ϕ histogram. The correction function is a constant as shown in Fig. 73 and has a value of 1.0166. The beam asymmetry values of each set (0/90 and -45/45) were multiplied by this factor for the final results shown in Sec 7.1.

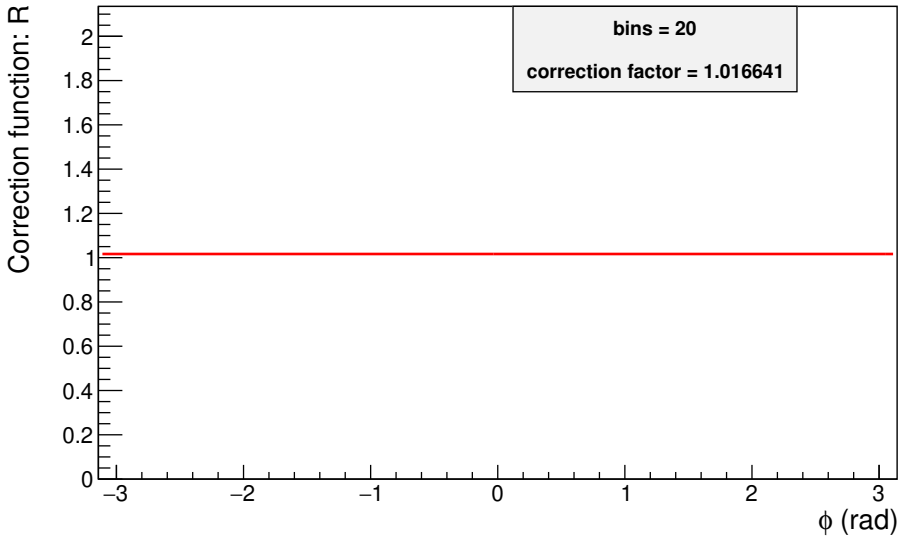

FIG. 73: Correction function R defined in Eqn. 50 for a bin width of $\Delta = \frac{2\pi}{20}$

5.5.6 MINIMUM PHOTON ENERGY DEPENDENCE

The reaction under study involves low energy radiated photons from Σ^0 decay. The BCAL energy threshold was lowered to 50 MeV while making the ROOT TTrees. Figure 74 shows the photon energy (E_γ) distribution in the lab frame for events with 0.1 (GeV/c)^2 $< -t <$ 1.4 (GeV/c)^2. It was estimated that 63% of the total events are below 100 MeV.

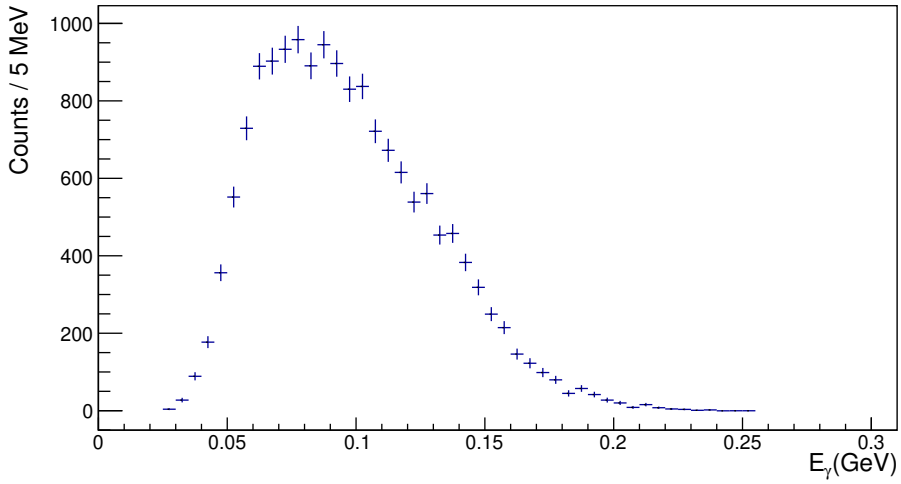

FIG. 74: E_γ distribution in the lab frame for 0.1 (GeV/c)^2 $< -t <$ 1.4 (GeV/c)^2.

To estimate the sensitivity of the measured Σ values to the minimum photon energy in the final state, asymmetries were measured again using the minimum photon energy 55 MeV and 60 MeV. The measured asymmetries with the varied photon energies are shown in Fig. 75. The deviations of the red and blue points from the nominal asymmetry value were computed for all $-t$ bins and the standard deviations of histograms were taken as the systematic uncertainty on minimum photon energy. Average deviation for 0/90 orientation is -0.004 while the maximum deviation is 0.048. Average deviation for -45/45 orientation is 0.012 while the maximum deviation is 0.079. A systematic error of 2.648% was assigned to 0/90 orientation and an error of 2.866% was assigned to -45/45 orientation respectively.

The impact of this cut variation on the total number of signal events was estimated using the distribution shown in Fig. 74. It was found that 8.4% of signal is lost when applying a minimum photon energy cut at 60 MeV.

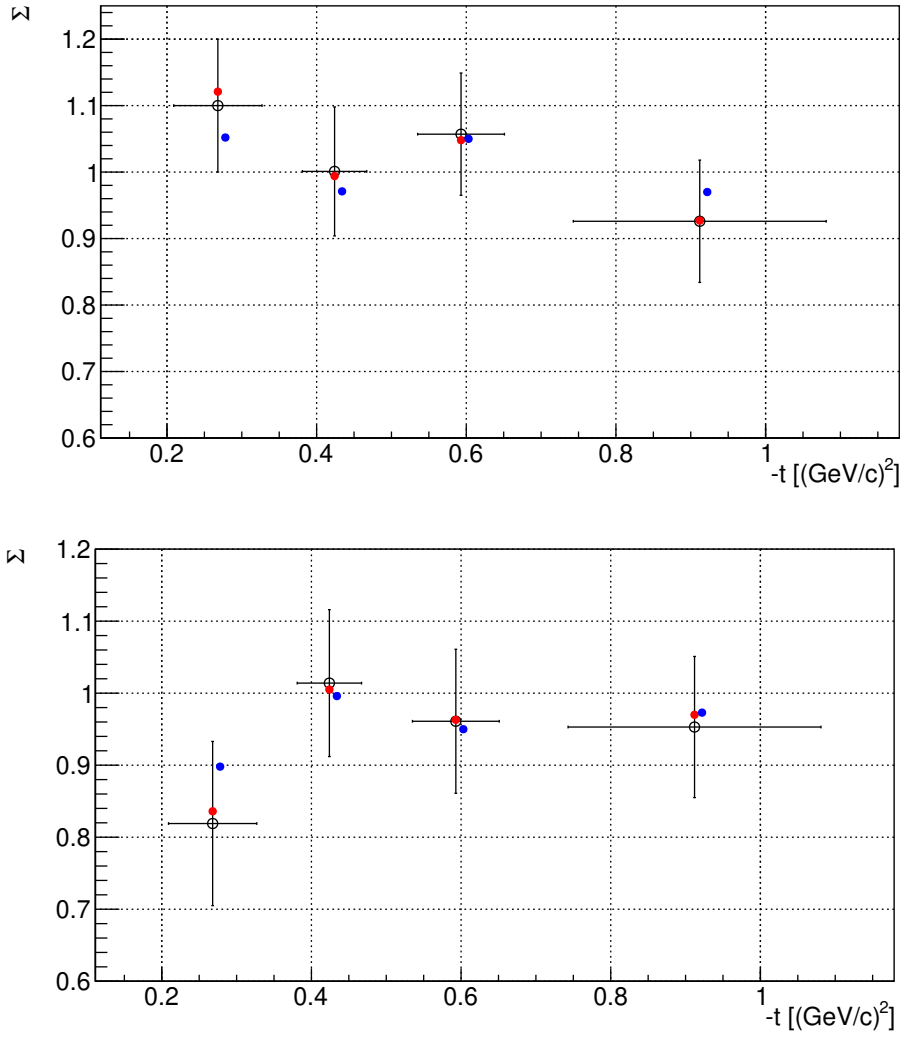

FIG. 75: Σ asymmetry measured after changing minimum photon energy (red closed points for 55 MeV and blue closed points for 60 MeV) in the 0/90 (top) and -45/45 (bottom) orientations. The open circles and error bars are the asymmetry values and statistical errors using the nominal minimum photon energy (50 MeV).

5.5.7 ASYMMETRY FROM THE BACKGROUND

In order to find the systematic uncertainty from the 2% background under the Σ^0 peak the beam asymmetry was found using a sideband region of the invariant mass of $\Lambda\gamma$. Events were selected in the region 1.23 GeV/c^2 < $M_{\Lambda\gamma}$ < 1.4 GeV/c^2 where the Λ events were in the range 1.107 GeV/c^2 < $M_{\pi^- p}$ < 1.125 GeV/c^2.

The relation between measured asymmetry, A_m and asymmetry of the signal, A_s and the background, A_b is as follows:

$$A_m = A_s \cdot f_s + A_b \cdot f_b, \tag{51}$$

that leads to

$$A_s = \frac{A_m - A_b \cdot f_b}{f_s} \tag{52}$$

where f_s and f_b are the fractions of signal (0.98) and background (0.02) events. Due to the low number of events in the sideband region, we made a sample of events by combining the two data sets 0/90 and -45/45 and found the beam asymmetries from the background in the entire t range used in the analysis. Figure 76 shows the fit to the yield asymmetry in the chosen $M_{\Lambda\gamma}$ sideband region.

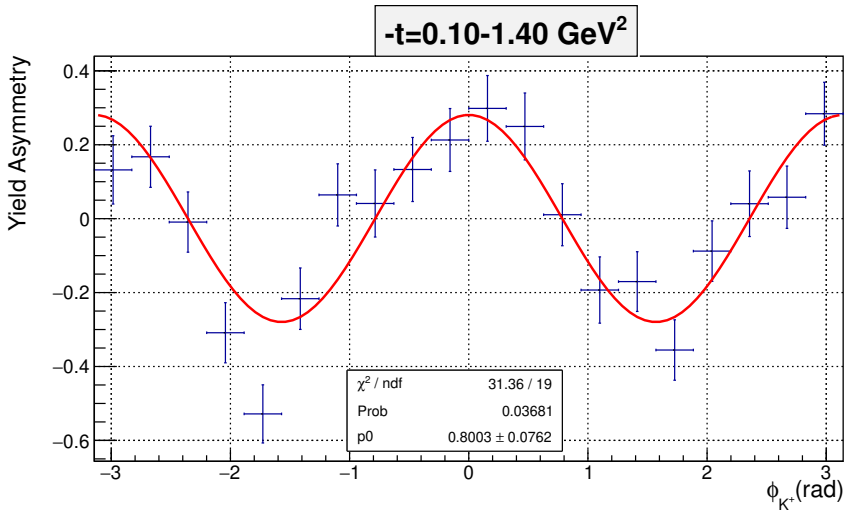

FIG. 76: Fit to the yield asymmmetry in the region 1.23 GeV/c^2 < $M_{\Lambda\gamma}$ < 1.4 GeV/c^2 for 0.1 (GeV/c)^2 < $-t$ < 1.4 (GeV/c)^2.

From the fit parameter the beam asymmetry was extracted and after finite bin correction

we obtained a value $A_b = 0.814 \pm 0.076$. For the average measured asymmetry we calculated the statistical weighted mean of the values given in Table 33 and it was found to be $A_m = 1.000$. Then, using Eqn. 52, we obtained $A_s = 1.004$ therefore a systematic uncertainty of 0.004 was included as the uncertainty associated with the background for the t-channel.

5.5.8 NON-UNIFORMITY OF ACCEPTANCE

For the fit function given by Eqn. 46 we were only considering the beam asymmetry Σ as the polarization observable in the yields for a given orientation. In general for an experiment with a linearly polarized photon beam and an unpolarized target, when the polarization of the recoiling hyperon can be determined via a weak decay asymmetry, the differential cross section is given by,

$$\begin{aligned}\frac{d\sigma}{d\Omega} = \left(\frac{d\sigma}{d\Omega}\right)_0 \{1 &- P^\gamma \Sigma \cos\,2\phi + \alpha \cos\theta_x P^\gamma O_x \sin\,2\phi \\ &+ \alpha P \cos\theta_y - \alpha \cos\theta_y P^\gamma T \cos\,2\phi \\ &+ \alpha \cos\theta_z P^\gamma O_z \sin\,2\phi\}\end{aligned} \tag{53}$$

where $\left(\frac{d\sigma}{d\Omega}\right)_0$ is the unpolarized cross section, P^γ is the polarization of the beam and P, T, O_x and O_z are polarization observables. The direction cosines $\cos\theta_{x,y,z}$ indicate the direction of the decay proton in the hyperon (Σ^0) rest frame and α is the weak decay asymmetry [48].

Figure 77 shows the definition of axis used. The three axes $\hat{x}, \hat{y}$ and $\hat{z}$ are defined in the center of mass frame as,

$$\hat{z} = \frac{\vec{p_\gamma}}{|\vec{p_\gamma}|},\ \hat{y} = \frac{\vec{p_\gamma} \times \vec{p_K}}{|\vec{p_\gamma} \times \vec{p_K}|},\ \hat{x} = \hat{y} \times \hat{z} \tag{54}$$

where $\vec{p_\gamma}$ and $\vec{p_K}$ are momenta of the incoming photon beam and the outgoing kaon. Then the angles θ_x, θ_y and θ_z are measured from the axes $\hat{x}, \hat{y}$ and $\hat{z}$ after boosting to the Σ^0 rest frame and using the final proton momentum vector in the Σ^0 frame.

In the standard analysis method it is assumed that the acceptances in θ_x, θ_y and θ_z are flat and we can try to derive a general formula for the yield asymmetry in the case where acceptances $A(\theta_x)$, $A(\theta_y)$ and $A(\theta_z)$ are not uniform. Then we can make an estimation to see how much uncertainty will be due to this non-uniform acceptance.

Using Eqn. 53 the event yields for $\parallel$ and $\perp$ photon beam polarization orientations can

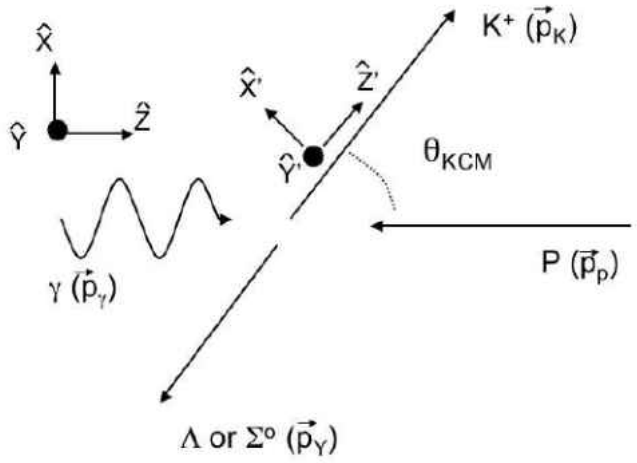

FIG. 77: The definitions of the axes used in the study. Figure is from Ref. [49].

be written as,

$$\begin{aligned} Y_{\parallel}(\phi,\theta_x,\theta_y,\theta_z) \propto A(\phi,\theta_x,\theta_y,\theta_z)[1 &- P_{\parallel}\Sigma\cos\,2\phi + \alpha\cos\theta_x P_{\parallel}O_x\sin\,2\phi \\ &+ \alpha P\cos\theta_y - \alpha\cos\theta_y P_{\parallel}T\cos\,2\phi \\ &+ \alpha\cos\theta_z P_{\parallel}O_z\sin\,2\phi] \end{aligned} \tag{55}$$

$$\begin{aligned} Y_{\perp}(\phi,\theta_x,\theta_y,\theta_z) \propto A(\phi,\theta_x,\theta_y,\theta_z)[1 &+ P_{\perp}\Sigma\cos\,2\phi - \alpha\cos\theta_x P_{\perp}O_x\sin\,2\phi \\ &+ \alpha P\cos\theta_y + \alpha\cos\theta_y P_{\perp}T\cos\,2\phi \\ &- \alpha\cos\theta_z P_{\perp}O_z\sin\,2\phi] \end{aligned} \tag{56}$$

if $P_{\parallel} = P_{\perp} = P_{\gamma}$, the yield asymmetry will be

$$\begin{aligned} \frac{Y(\phi)_{\perp} - Y(\phi)_{\parallel}}{Y(\phi)_{\perp} + Y(\phi)_{\parallel}} = \frac{} {} & P_{\gamma}\Sigma\cos\,2\phi\int A(\theta_x)d(\cos\theta_x)\int A(\theta_y)d(\cos\theta_y)\int A(\theta_z)d(\cos\theta_z) \\ & - \alpha P_{\gamma}O_x\sin\,2\phi\int A(\theta_x)\cos\theta_x\,d(\cos\theta_x)\int A(\theta_y)d(\cos\theta_y)\int A(\theta_z)d(\cos\theta_z) \\ & + \alpha P_{\gamma}T\cos\,2\phi\int A(\theta_x)d(\cos\theta_x)\int A(\theta_y)\cos\theta_y\,d(\cos\theta_y)\int A(\theta_z)d(\cos\theta_z) \\ & - \alpha P_{\gamma}O_z\sin\,2\phi\int A(\theta_x)d(\cos\theta_x)\int A(\theta_y)d(\cos\theta_y)\int A(\theta_z)\cos\theta_z\,d(\cos\theta_z) \\ \hline & \int A(\theta_x)d(\cos\theta_x)\int A(\theta_y)d(\cos\theta_y)\int A(\theta_z)d(\cos\theta_z) \\ & + \alpha P\int A(\theta_x)d(\cos\theta_x)\int A(\theta_y)\cos\theta_y\,d(\cos\theta_y)\int A(\theta_z)d(\cos\theta_z) \end{aligned} \tag{57}$$

This can be written as,

$$\frac{Y(\phi)_\perp - Y(\phi)_\parallel}{Y(\phi)_\perp + Y(\phi)_\parallel} = \frac{\begin{array}{l} P_\gamma \Sigma \cos 2\phi - \alpha P_\gamma O_x \sin 2\phi \frac{\int A(\theta_x)\cos\theta_x \, d(\cos\theta_x)}{\int A(\theta_x) d(\cos\theta_x)} \\ + \alpha P_\gamma T \cos 2\phi \frac{\int A(\theta_y)\cos\theta_y \, d(\cos\theta_y)}{\int A(\theta_y) d(\cos\theta_y)} - \alpha P_\gamma O_z \sin 2\phi \frac{\int A(\theta_z)\cos\theta_z \, d(\cos\theta_z)}{\int A(\theta_z) d(\cos\theta_z)} \end{array}}{1 + \alpha P \frac{\int A(\theta_y)\cos\theta_y \, d(\cos\theta_y)}{\int A(\theta_y) d(\cos\theta_y)}} \quad (58)$$

If we consider $R_x = \frac{\int A(\theta_x)\cos\theta_x \, d(\cos\theta_x)}{\int A(\theta_x) d(\cos\theta_x)}, R_y = \frac{\int A(\theta_y)\cos\theta_y \, d(\cos\theta_y)}{\int A(\theta_y) d(\cos\theta_y)}, \; R_z = \frac{\int A(\theta_z)\cos\theta_z \, d(\cos\theta_z)}{\int A(\theta_z) d(\cos\theta_z)}$ and calculate the integrals in $\cos\theta_i$ from -1 to 1 we can find the contribution coming from the asymmetry of events in the corresponding angle.

Tables 11-13 show the calculated integrals and the corresponding ratios for each $-t$ bin used in the analysis. The values from integrals contained more significant figures and are used to find the ratio but the values given in tables are rounded. Acceptance plots in angles θ_x, θ_y and θ_z are shown in Appendix F. The acceptance histograms were fitted with a 4th order polynomial and the acceptance functions were found for use in the integrals.

Additionally, 2d plots were made for recoil angles θ_x, θ_y and θ_z vs. K^+ lab ϕ angle from t-channel MC and corresponding acceptances are shown in Appendix F. Acceptances are uniform in ϕ.

$-t$ bin [(GeV/c)^2]	$\int A(\theta_x)d(\cos\theta_x)$	$\int A(\theta_x)\cos\theta_x\, d(\cos\theta_x)$	R_x
$0.10 < -t < 0.35$	0.026	0.010	0.385
$0.35 < -t < 0.50$	0.073	0.031	0.419
$0.50 < -t < 0.70$	0.084	0.030	0.362
$0.70 < -t < 1.40$	0.082	0.022	0.266

TABLE 11: The integrals associated with the asymmetry of events in recoil angle θ_x for t-channel

$-t$ bin [(GeV/c)^2]	$\int A(\theta_y)d(\cos\theta_y)$	$\int A(\theta_y)\cos\theta_y\, d(\cos\theta_y)$	R_y
$0.10 < -t < 0.35$	0.026	0.004	0.148
$0.35 < -t < 0.50$	0.073	0.009	0.127
$0.50 < -t < 0.70$	0.084	0.011	0.126
$0.70 < -t < 1.40$	0.082	0.011	0.138

TABLE 12: The integrals associated with the asymmetry of events in recoil angle θ_y for t-channel

$-t$ bin [(GeV/c)^2]	$\int A(\theta_z)d(\cos\theta_z)$	$\int A(\theta_z)\cos\theta_z\, d(\cos\theta_z)$	R_z
$0.10 < -t < 0.35$	0.026	0.00009	0.003
$0.35 < -t < 0.50$	0.073	-0.005	-0.075
$0.50 < -t < 0.70$	0.084	-0.008	-0.090
$0.70 < -t < 1.40$	0.082	-0.007	-0.083

TABLE 13: The integrals associated with the asymmetry of events in recoil angle θ_z for t-channel

Writing Eqn. 58 in terms of R_x, R_y and R_z gives,

$$\frac{Y(\phi)_\perp - Y(\phi)_\parallel}{Y(\phi)_\perp + Y(\phi)_\parallel} = \frac{\begin{array}{c} P_\gamma \Sigma \cos\,2\phi - \,\alpha P_\gamma O_x \sin\,2\phi\, R_x \\ + \alpha P_\gamma T \cos\,2\phi\, R_y - \,\alpha P_\gamma O_z \sin\,2\phi\, R_z \end{array}}{1 + \alpha P\, R_y} \tag{59}$$

This can be written in the following form,

$$\frac{Y(\phi)_\perp - Y(\phi)_\parallel}{Y(\phi)_\perp + Y(\phi)_\parallel} = \frac{P_\gamma[(\Sigma + B)\cos\,2\phi + C\,\sin\,2\phi]}{1 + D} \tag{60}$$

where $B = \alpha\, T R_y$, $C = -(\alpha\, O_x R_x + \alpha\, O_z R_z)$ and $D = \alpha\, P R_y$.

In order to find the constants B, C and D we used $\alpha = 0.750$ [50] and the RPR-2007 model [14] predictions for P,T,O_x and O_z. Figure 78 shows the predictions for those polarization observables and beam asymmetry Σ for the t-channel. Values found for B, C and D are given in Table 14.

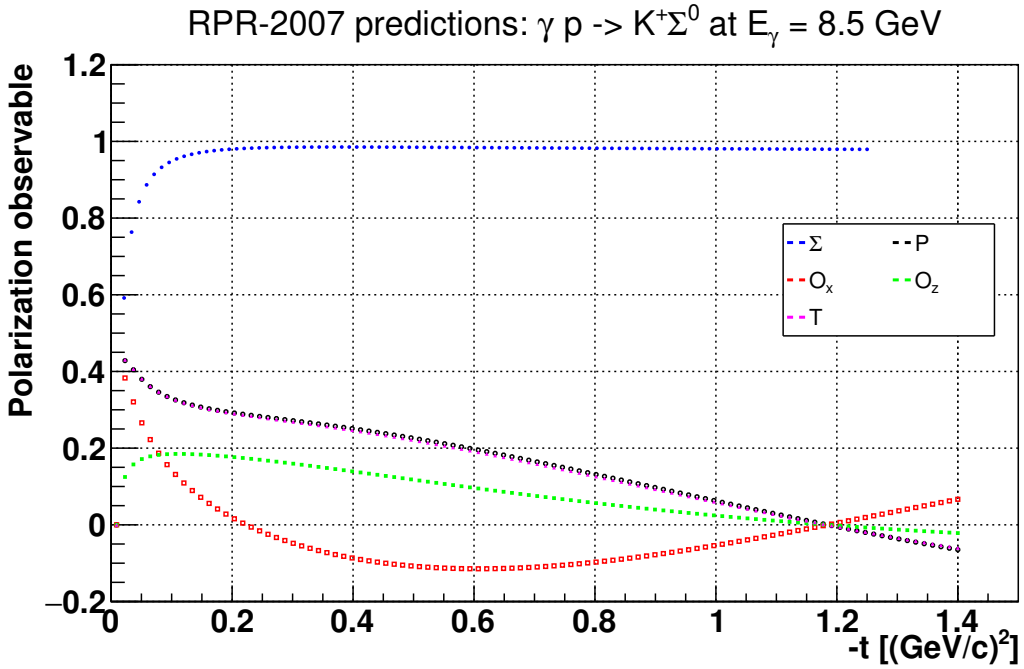

FIG. 78: RPR-2007 predictions for polarization observables for $\gamma p \to K^+\Sigma^0$ at $E_\gamma = 8.5$ GeV for the t-channel.

$-t$ [(GeV/c)^2]	B	C	D
0.268	0.0305994	0.00828148	0.0308824
0.424	0.0229152	0.0368844	0.0233467
0.593	0.0183028	0.0376789	0.0188395
0.912	0.00917362	0.0173528	0.00963026

TABLE 14: Constants B, C and D for the mean values of $-t$ bins used in the analysis.

Then we can use the new fit function given in Eqn. 60 and find the beam asymmetry values (only fit parameter) to compare with the nominal fit results. Tables 15 and 16 show the values from the fits and the differences.

$-t$ [(GeV/c)^2]	nominal fit value	new fit value	difference
0.268	1.100	1.104	0.004
0.424	1.001	1.002	0.001
0.593	1.057	1.058	0.001
0.912	0.9263	0.9267	0.0004

TABLE 15: Comparison of Σ after the new fit with the nominal values for 0/90 orientation set.

$-t$ [(GeV/c)^2]	nominal fit value	new fit value	difference
0.268	0.8191	0.8141	0.0050
0.424	1.0144	1.0159	0.0015
0.593	0.9612	0.9611	0.0001
0.912	0.9530	0.9521	0.0009

TABLE 16: Comparison of Σ after the new fit with the nominal values for -45/45 orientation set.

This suggests that the maximum systematic uncertainty due to non-uniform acceptance is $\sim$0.5% for the t-channel. However as can be seen in Fig. 78, P and T have almost same values from the model prediction. This can be due to some theoretical constraints on the polarization observables the model has used and we did another study to find the systematic uncertainty using more conservative values for P and T.

The values used are,

(i) $T = 0$ and $P = 0.25$

(ii) $T = 0.25$ and $P = 0.1$.

O_x and O_z were assumed to be zero.

Case (i): $T = 0, P = 0.25$ and $O_x = O_z = 0$

$-t$ [(GeV/c)^2]	B	C	D
0.268	0	0	0.02775
0.424	0	0	0.0238125
0.593	0	0	0.023625
0.912	0	0	0.025875

TABLE 17: Constants B, C and D for the mean values of $-t$ bins used in the analysis for $T = 0$ and $P = 0.25$.

$-t$ [(GeV/c)^2]	nominal fit value	new fit value	difference
0.268	1.100	1.131	0.031
0.424	1.001	1.025	0.024
0.593	1.057	1.081	0.024
0.912	0.926	0.951	0.025

TABLE 18: Comparison of Σ values after the new fit with the nominal values for 0/90 orientation set for $T = 0$ and $P = 0.25$.

$-t$ [(GeV/c)^2]	nominal fit value	new fit value	difference
0.268	0.819	0.842	0.023
0.424	1.014	1.038	0.024
0.593	0.961	0.984	0.023
0.912	0.953	0.977	0.024

TABLE 19: Comparison of Σ values after the new fit with the nominal values for -45/45 orientation set for $T = 0$ and $P = 0.25$.

Case (ii): $T = 0.25, P = 0.1$ and $O_x = O_z = 0$

$-t$ [(GeV/c)^2]	B	C	D
0.268	0.02775	0	0.0111
0.424	0.0238125	0	0.009525
0.593	0.023625	0	0.00945
0.912	0.025875	0	0.01035

TABLE 20: Constants B, C and D for the mean values of $-t$ bins used in the analysis for $T = 0.25$ and $P = 0.1$.

$-t$ [(GeV/c)^2]	nominal fit value	new fit value	difference
0.268	1.100	1.085	0.015
0.424	1.001	0.987	0.014
0.593	1.057	1.043	0.014
0.912	0.926	0.910	0.016

TABLE 21: Comparison of Σ values after the new fit with the nominal values for 0/90 orientation set for $T = 0.25$ and $P = 0.1$.

$-t$ [(GeV/c)^2]	nominal fit value	new fit value	difference
0.268	0.819	0.801	0.018
0.424	1.014	1.000	0.014
0.593	0.961	0.947	0.014
0.912	0.953	0.937	0.016

TABLE 22: Comparison of Σ values after the new fit with the nominal values for -45/45 orientation set for $T = 0.25$ and $P = 0.1$.

From Tables 18 - 22 we can see that the systematic uncertainties range from $\sim$1% - 3%. We chose to include 3% as a more conservative systematic uncertainty due to the non-uniform acceptance for the t-channel.

5.5.9 BEAM POLARIZATION

The beam polarization values used for beam asymmetry analysis and their statistical uncertainties were given in Table 2. We see that for each orientation polarization P is close to 0.35 while the statistical uncertainty is around 0.01. This gives $\frac{\delta P}{P} \approx 0.03$. This uncertainty will shift beam asymmetry measurements by an overall scale factor. Systematic uncertainties on TPOL measurements also contribute to this normalization uncertainty. The systematic uncertainty from TPOL is estimated to be 1.5% [26]. Since the final beam asymmetry result contains statistically weighted result from four orientations, the statistical uncertainty must be scaled by a factor of 4. The total normalization uncertainty on the final beam asymmetry result is therefore, $\sqrt{\frac{(0.03)^2}{4} + (0.015)^2} = 2.1\%$. This will not be combined with other systematic uncertainties.

5.5.10 SYSTEMATICS SUMMARY

A summary of systematic uncertainties on the Σ beam asymmetries obtained for the t-channel is presented in Table 23. Total systematic uncertainty for each orientation set was found by adding individual contributions given in Table 23 in quadrature. As mentioned in Sec. 5.5.9, the uncertainty from the beam polarization was not combined with this systematics.

Study	0/90 Systematic Error	-45/45 Systematic Error
Event selection	0.031-0.059	0.030-0.053
Phase dependence	0.001	0.007
Flux normalization dependence	0.005	0.004
Minimum photon energy	0.026	0.029
Background	0.004	0.004
Non-uniform acceptance	0.030	0.030
Total	0.051-0.071	0.052-0.068

TABLE 23: Summary of systematic uncertainties from the studies described in Sec. 5.5.

CHAPTER 6

BEAM ASYMMETRY MEASUREMENT (u-CHANNEL)

6.1 FITS TO THE Σ^0 SAMPLE

Figures 79 and 80 show the fits used for the Σ^0 event sample integrated over the entire u region used for the analysis ($-u < 2.0$ (GeV/c)^2). The upper plots are fits to the PARA (left) and PERP (right) yields independently. There are two free parameters in these fits of the form $f(\phi) = C[1 + P\Sigma\cos(2(\phi - \phi_0))]$, with $p_0 = C$ for normalization and $p_1 = P\Sigma$. Fits to the sum of yields were done using the functional form given in Eqn. 49.

Same phase constant values were used for ϕ_0 which were given in Sec. 5.3.

From the yield asymmetry plots, beam asymmetry values were obtained for $-u < 2.0$ (GeV/c)^2 and they are,

$\Sigma = 0.428 \pm 0.099$ for 0/90 orientation,

$\Sigma = 0.338 \pm 0.099$ for -45/45 orientation

where uncertainties are statistical errors from the fits.

Additionally, a linear fit was done for the sum of yields to compare χ^2 values with that for cosine fit. Linear fits are shown in Figs. 81 and 82. Both types of fits seem to have similar χ^2 values.

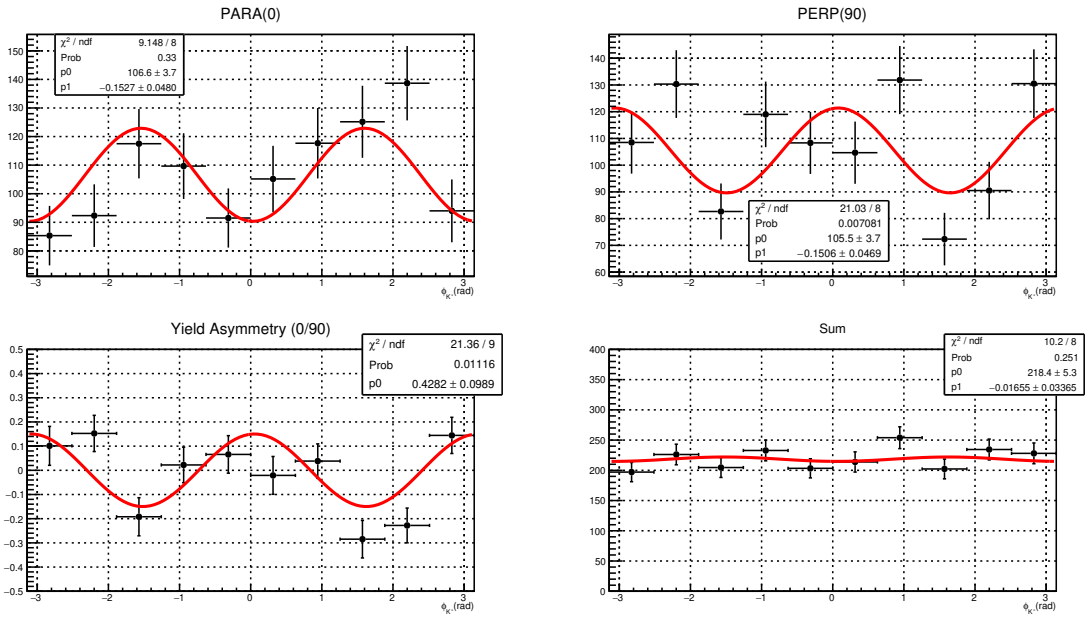

FIG. 79: Polarization direction set to 0/90. Fits to the ϕ distributions in the beam energy range $8.2 < E_\gamma < 8.8$ GeV, integrated over the entire u range. Upper row: fits to the PARA (left) and PERP (right) distributions independently. Lower row (left): fit to the asymmetry (Eqn. 45). Lower row (right): fit to the sum $Y(\phi)_\perp + F_R Y(\phi)_\parallel$, which is sensitive to instrumental asymmetries.

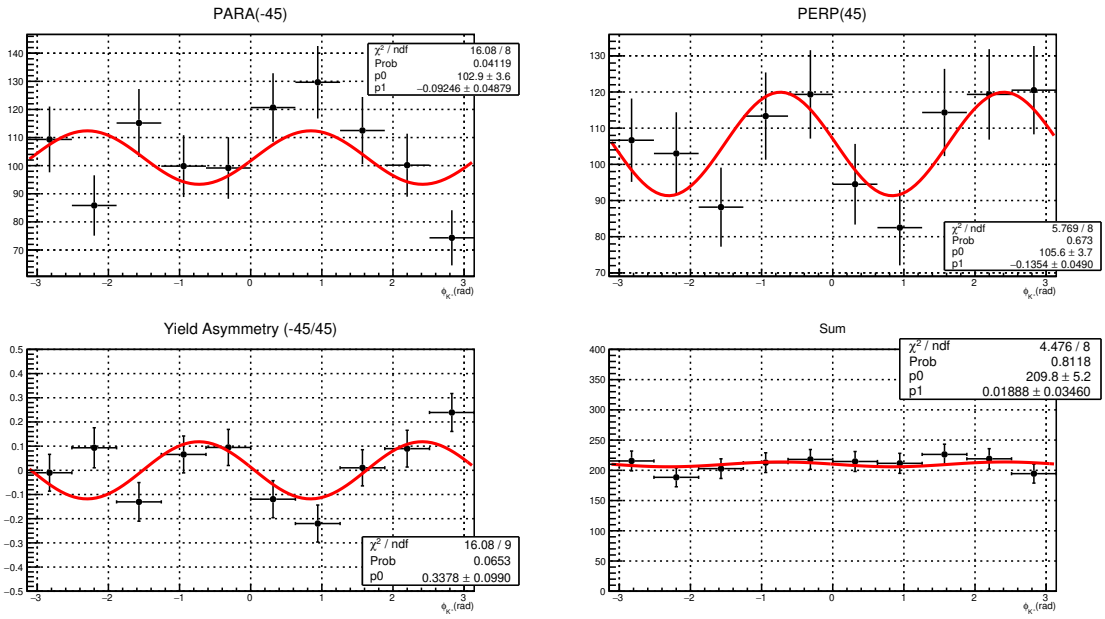

FIG. 80: Polarization direction set to -45/45. Fits to the ϕ distributions in the beam energy range $8.2 < E_\gamma < 8.8$ GeV, integrated over the entire u range. Upper row: fits to the PARA (left) and PERP (right) distributions independently. Lower row (left): fit to the asymmetry (Eqn. 45). Lower row (right): fit to the sum $Y(\phi)_\perp + F_R Y(\phi)_\parallel$, which is sensitive to instrumental asymmetries.

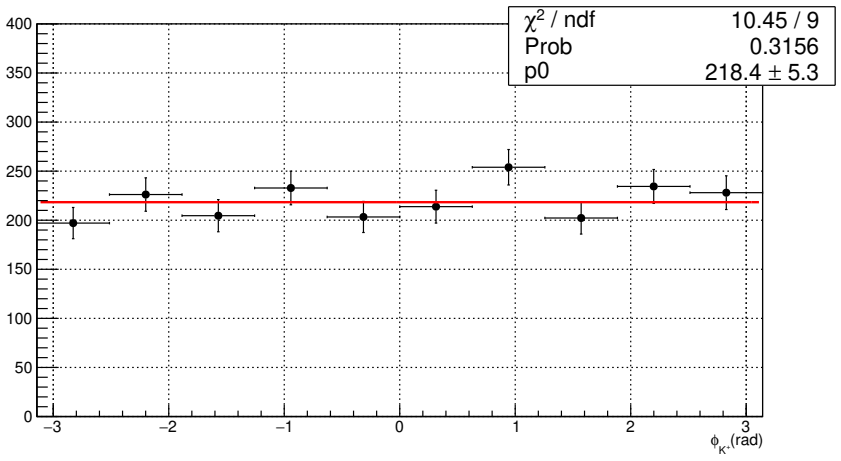

FIG. 81: Linear fit to the sum $Y(\phi)_{\perp} + F_R Y(\phi)_{\parallel}$ for 0/90 orientation.

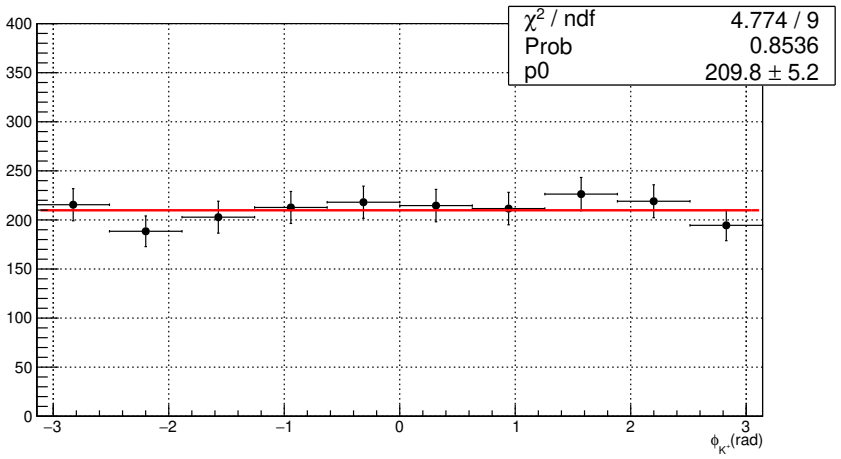

FIG. 82: Linear fit to the sum $Y(\phi)_{\perp} + F_R Y(\phi)_{\parallel}$ for -45/45 orientation.

6.2 SYSTEMATIC STUDIES

6.2.1 EVENT SELECTION

By varying the parameters of the event selection described in Sec. 4.2.2, the systematic dependence of the asymmetry on the event selection criteria was studied. The list of nominal cuts and the looser and tighter cuts that were used for this are same as those in Table 6. For each variation of the cut, the asymmetry was extracted for the $-u$ bin.

Figure 83 shows the values of the asymmetry where each parameter is represented by an individual color, and the asymmetries for the nominal cut parameters are shown by the open black circles. All the filled data points are within the 1σ statistical error of the nominal cut value points. Colors for different cut variations are the same as shown in Fig. 63.

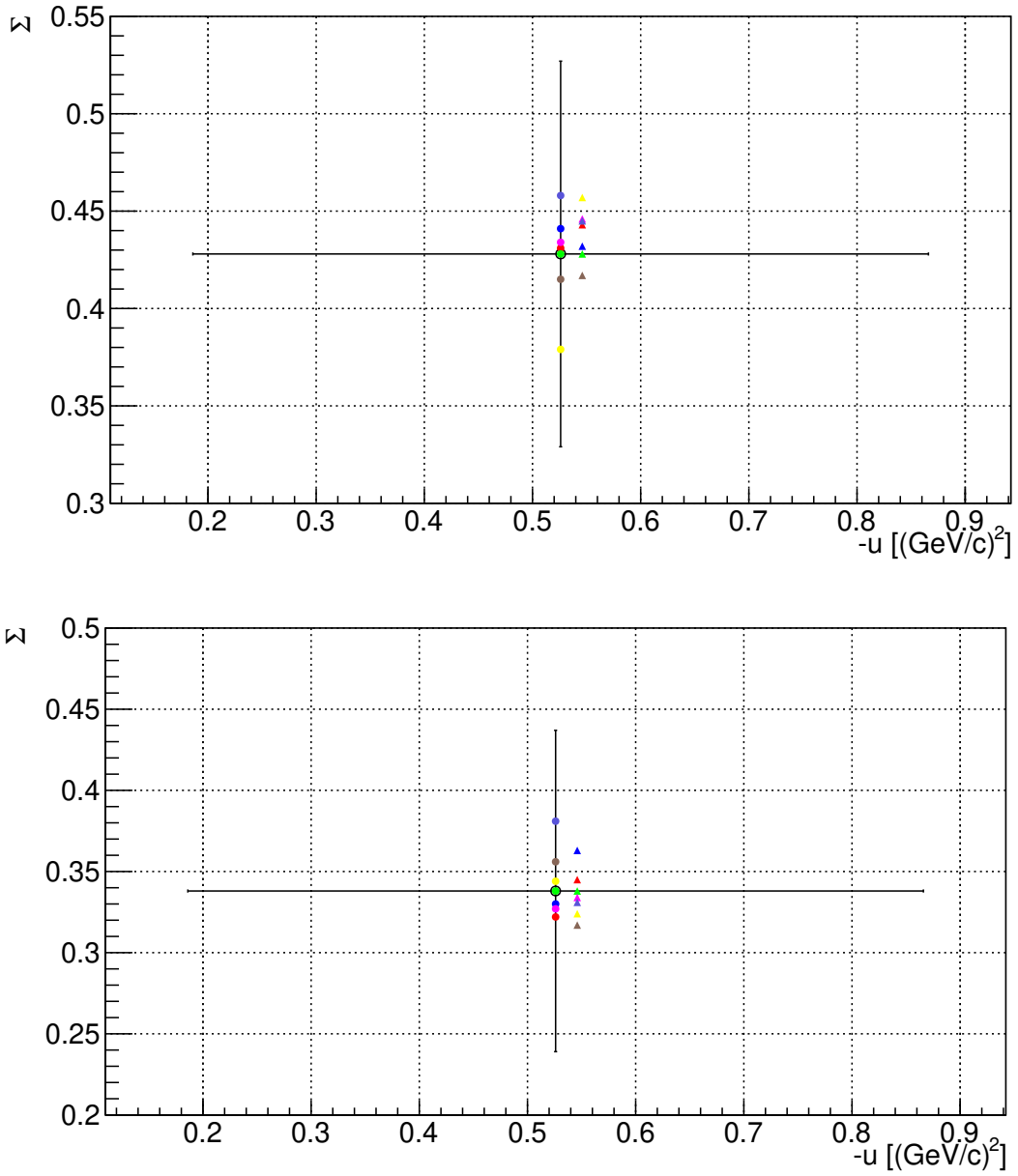

FIG. 83: Σ asymmetry measured for each of the cut parameter variations, shown as different colored points for the 0/90 (top) and -45/45 (bottom) orientations. The open circles and vertical error bars are the asymmetry values and statistical errors using the nominal cut parameters.

Table 24 gives the systematic uncertainties for each cut variation for 0/90 and -45/45 orientation sets.

The total systematic uncertainty due to the cut variation is 5% for 0/90 orientation and

cut variation	0/90 uncertainty	-45/45 uncertainty
K^+ vertex z loose	0.015	0.007
K^+ vertex z tight	0.003	0.016
K^+ vertex r loose	0	0
K^+ vertex r tight	0	0
Missing mass squared loose	0.004	0.025
Missing mass squared tight	0.013	0.008
KinFit CL loose	0.029	0.014
KinFit CL tight	0.049	0.006
$M_{\pi^- p}$ loose	0.018	0.004
$M_{\pi^- p}$ tight	0.006	0.011
$M_{\Lambda\gamma}$ loose	0.011	0.021
$M_{\Lambda\gamma}$ tight	0.013	0.018
FCAL shower quality loose	0.017	0.007
FCAL shower quality tight	0.030	0.043

TABLE 24: Systematic uncertainty for each cut variation for 0/90 and -45/45 orientations.

4% for -45/45 orientation.

6.2.2 PHASE DEPENDENCE

Any sensitivity that can be due to fixing of the phase parameter ϕ_0 was studied with fitting the yield asymmetry allowing phase constant to be a free parameter. Figures 84 and 85 show yield asymmetry plots with phase parameter being free. Figure 86 shows the measured asymmetry values along with the nominal results.

Using the difference of beam asymmetry values from nominal, a systematic error of 2.2% was assigned to 0/90 orientation and an error of 2.1% was assigned to -45/45 orientation.

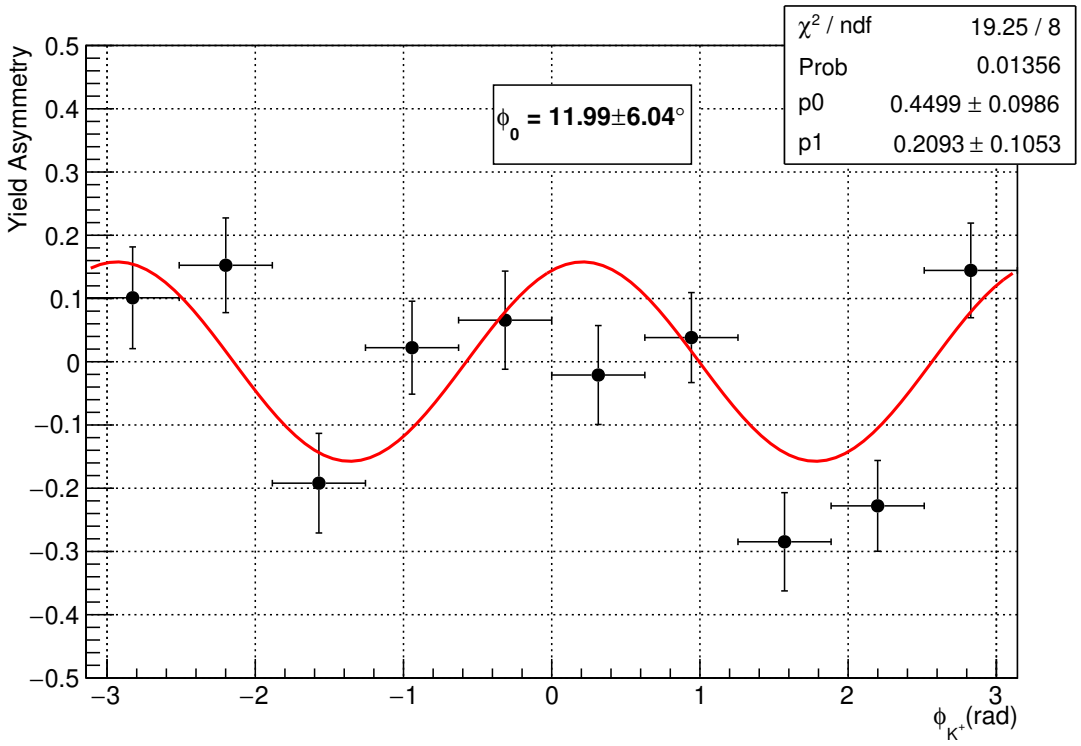

FIG. 84: Yield asymmetry allowing the phase to be a free parameter in the fit for 0/90 orientation. The ϕ_0 value on which fit converge is given in the text box inside the plot.

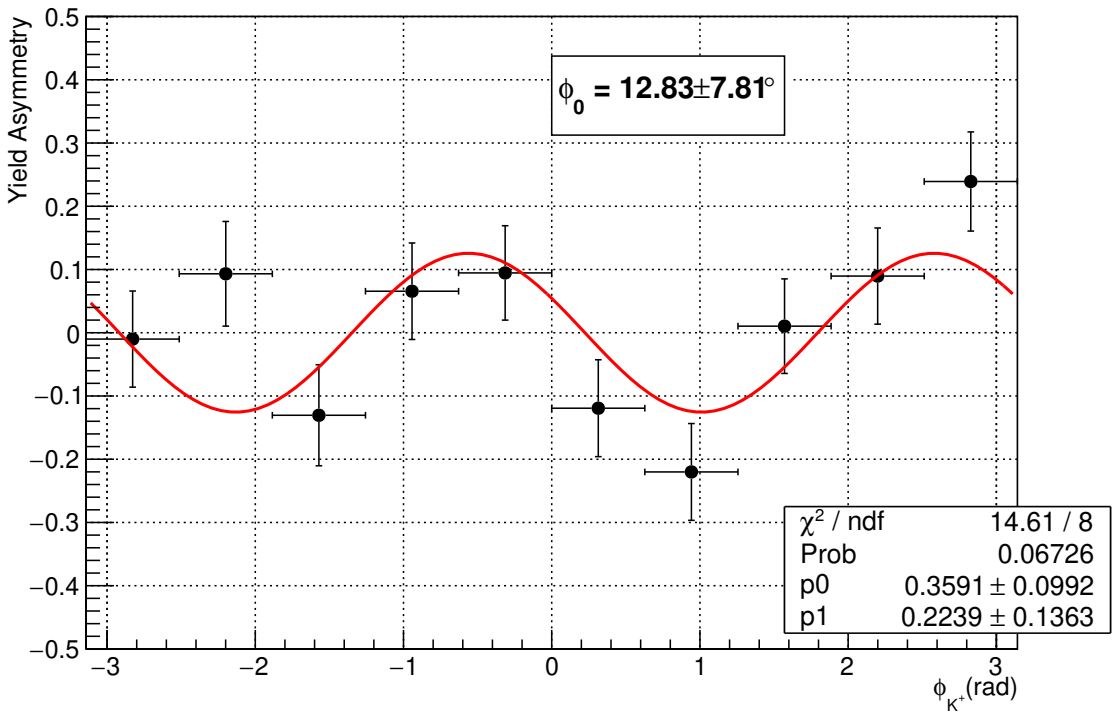

FIG. 85: Yield asymmetry allowing the phase to be a free parameter in the fit for -45/45 orientation. The ϕ_0 value on which fit converge is given in the text box inside the plot.

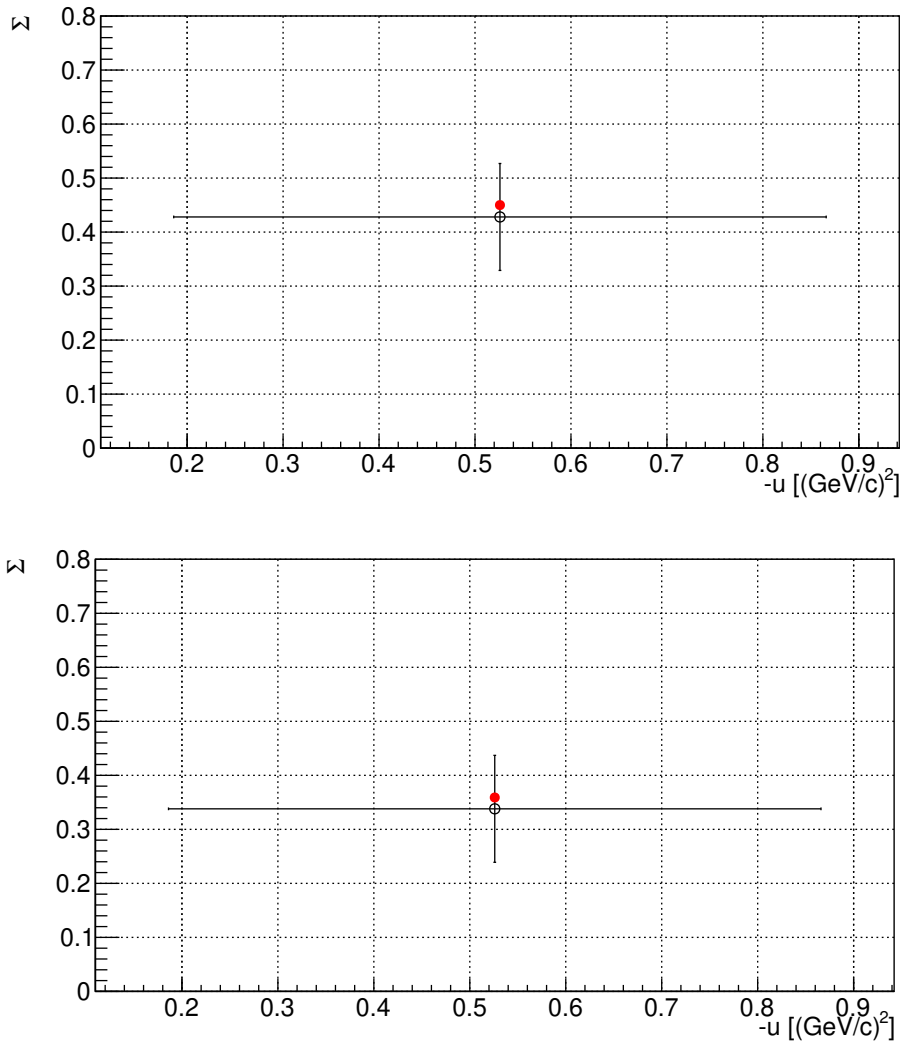

FIG. 86: Σ asymmetry measured while allowing the phase to be a free parameter in the fit (red closed point) in the 0/90 orientation (top) and -45/45 orientation (bottom). The open black circle and error bar are asymmetry value and statistical error using the fixed phase.

6.2.3 FLUX NORMALIZATION DEPENDENCE

To estimate the sensitivity of the measured Σ values to the flux normalization determined by PS yields, asymmetries were measured again by changing the nominal flux ratio by $\pm 5\%$. The measured asymmetries with the varied flux normalization are shown in Fig. 87. Using the difference between the measured asymmetries from the nominal, a systematic error of 0.6% was assigned to 0/90 orientation and an error of 0.2% was assigned to -45/45 orientation respectively.

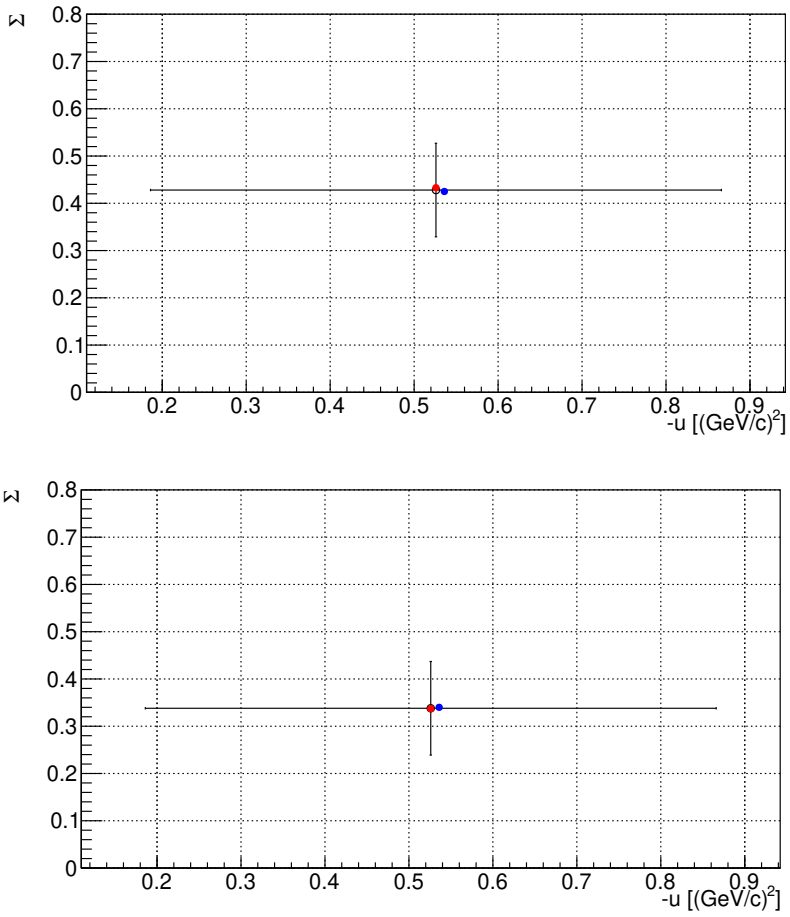

FIG. 87: Σ asymmetry measured after changing flux normalization by $\pm 5\%$ (red closed points for +5% and blue closed points for -5%) in the 0/90 (top) and -45/45 (bottom) orientations. The open circles and error bars are the asymmetry values and statistical errors using the nominal flux normalization.

6.2.4 FINITE ϕ BIN SIZE DEPENDENCE

The effect of the bin width of ϕ distribution was studied analytically using Eqn. 50. $\Delta = \frac{2\pi}{10}$ was used as the bin width. The correction function is a constant as shown in Fig. 88 and has a value of 1.069. Values of Σ shown in Sec. 6.1 were multiplied by this number and the corrected beam asymmetry values are given in Sec. 7.2.

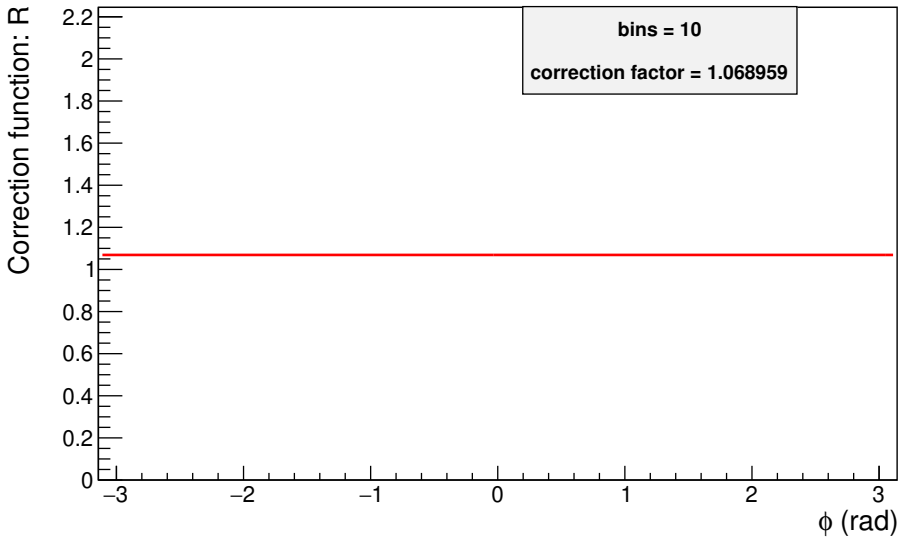

FIG. 88: Correction function R defined in Eqn. 50 for a bin width of $\Delta = \frac{2\pi}{10}$

6.2.5 MINIMUM PHOTON ENERGY DEPENDENCE

In Sec. 5.5.6, it was shown that there is a large fraction of photons from Σ^0 decay with energy below 100 MeV for the t-channel. Figure 89 shows the photon energy (E_γ) distribution in the lab frame for events with $-u < 2.0$ (GeV/c)^2. It was estimated that only 5% of the total events are below 100 MeV. So, the event sample in the low $|u|$ region is insensitive to the minimum shower energy around 50 MeV. Therefore a systematic uncertainty was not estimated for the u-channel due to minimum photon energy.

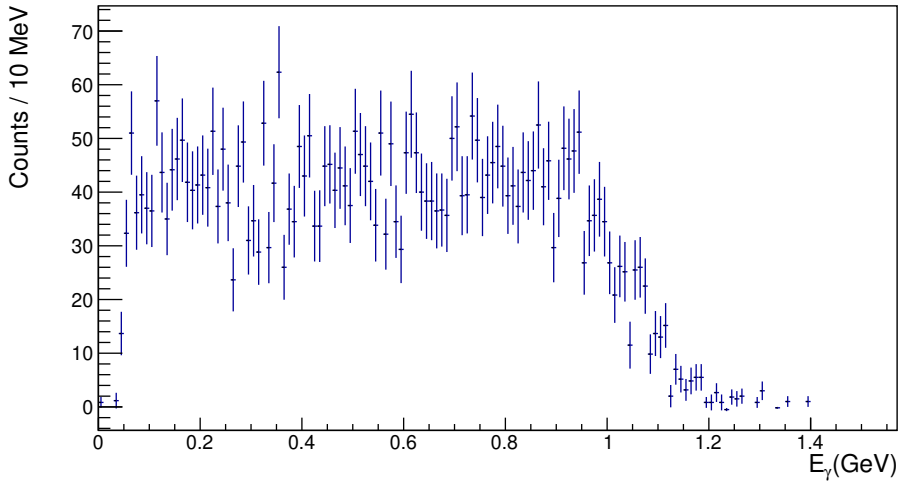

FIG. 89: E_γ distribution in the lab frame for $-u < 2.0$ (GeV/c)^2.

6.2.6 ASYMMETRY FROM THE BACKGROUND

Following the method used in Sec. 5.5.7 for the t-channel, beam asymmetry was calculated for the background using the region 1.23 GeV/c^2 $< M_{\Lambda\gamma} <$ 1.4 GeV/c^2 for $-u < 2.0$ (GeV/c)^2. Figure 90 shows the fit to the yield asymmetry.

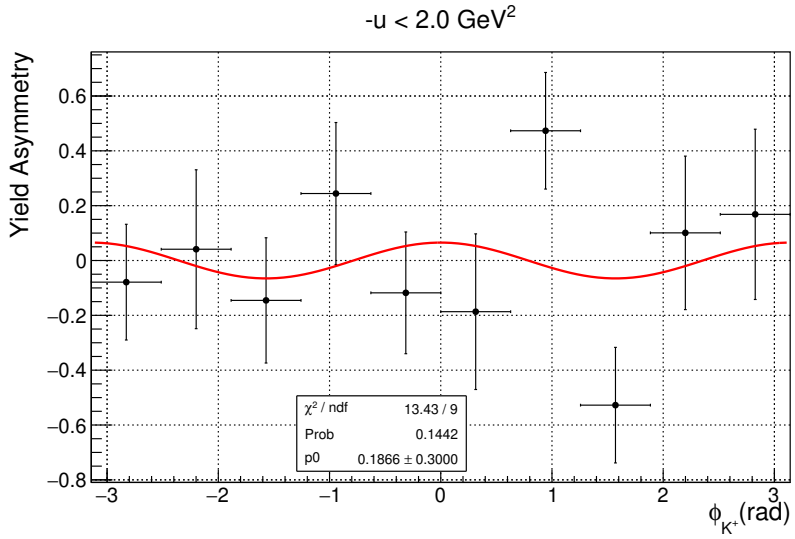

FIG. 90: Fit to the yield asymmmetry in the region 1.23 GeV/c^2 $< M_{\Lambda\gamma} <$ 1.4 GeV/c^2 for $-u < 2.0$ (GeV/c)^2.

From the fit parameter the beam asymmetry was extracted and the finite bin correction gave a value $A_b = 0.199 \pm 0.300$. The average measured asymmetry was found to be $A_m = 0.410$. Then, using Eqn. 52, we obtained a value of $A_s = 0.414$ therefore a systematic uncertainty of 0.004 was included as the uncertainty associated with the background for the u-channel.

6.2.7 NON-UNIFORMITY OF ACCEPTANCE

Similar to the method shown in Sec. 5.5.8 the non-uniformity of acceptance in recoil angles of the decay proton were estimated for the u-channel. Corresponding histograms are shown in Appendix F.

Additionally, 2d plots were made for recoil angles θ_x, θ_y and θ_z vs. K^+ lab ϕ angle from u-channel MC and the corresponding acceptances are shown in Appendix F. Acceptances are uniform in ϕ.

$-u$ bin [(GeV/c)^2]	$\int A(\theta_x) d(\cos\theta_x)$	$\int A(\theta_x)\cos\theta_x\, d(\cos\theta_x)$	R_x
$-u < 2.0$	0.2159	-0.0008	-0.0039

TABLE 25: The integrals associated with the asymmetry of events in recoil angle θ_x for u-channel.

$-u$ bin [(GeV/c)^2]	$\int A(\theta_y) d(\cos\theta_y)$	$\int A(\theta_y)\cos\theta_y\, d(\cos\theta_y)$	R_y
$-u < 2.0$	0.2158	0.0058	0.0268

TABLE 26: The integrals associated with the asymmetry of events in recoil angle θ_y for u-channel.

$-u$ bin [(GeV/c)^2]	$\int A(\theta_z) d(\cos\theta_z)$	$\int A(\theta_z)\cos\theta_z\, d(\cos\theta_z)$	R_z
$-u < 2.0$	0.2159	-0.0073	-0.0340

TABLE 27: The integrals associated with the asymmetry of events in recoil angle θ_z for u-channel.

In order to find the uncertainty using the ratios R_i, we made predictions for other polarization observables for a beam asymmetry value of $\Sigma = 0.4$. Based on the Ref. [51], the following constraint equations were used while calculating the observables.

$$|[\Sigma P - (C_x O_z - C_z O_x)] - T| < 0.005 \tag{61}$$

$$|[O_x^2 + O_z^2 + C_x^2 + C_z^2 + \Sigma^2 - T^2 + P^2] - 1| < 0.0001 \tag{62}$$

$$O_x^2 + O_z^2 + \Sigma^2 < 1 \tag{63}$$

$$|T - P| \leq 1 - \Sigma \tag{64}$$

$$|T + P| \leq 1 + \Sigma \tag{65}$$

Figure 91 show the relations between B,C and D and Fig. 92 shows P vs. T for 1000 possible values for P,T,O_x,O_z,C_x and C_z satisfying the above constraint equations. From the plot of D vs. B values for two extremes were used in the fit function given by Eqn. 60 while keeping $C = 0$.

The values used are,

(i) $B = 0.008$ and $D = 0.018$

(ii) $B = -0.018$ and $D = -0.008$

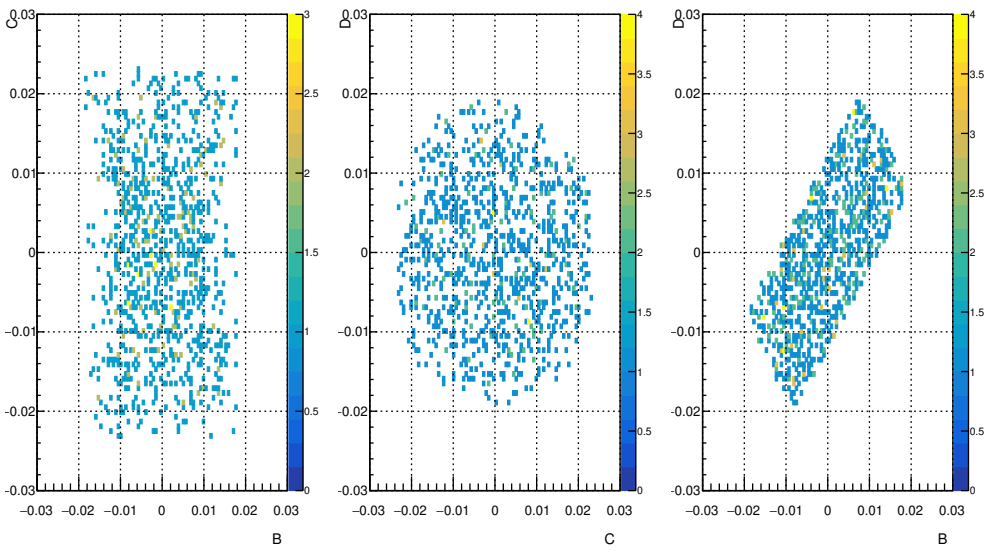

FIG. 91: Plots of the ratios C vs. B (left), D vs. C (middle) and D vs. B (right) found for $\Sigma = 0.4$.

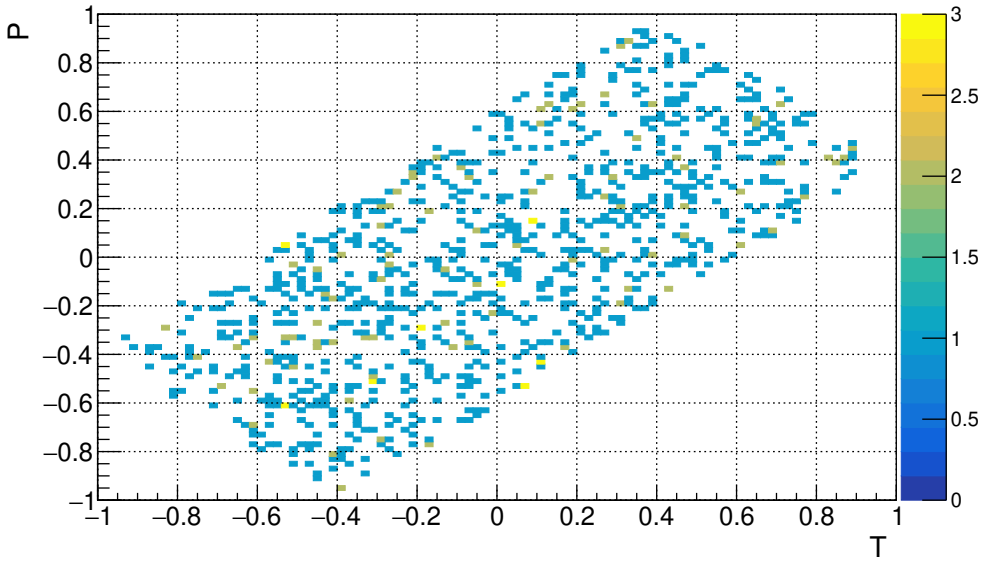

FIG. 92: P vs. T for $\Sigma = 0.4$.

Case (i):$B = 0.008$ and $D = 0.018$

orientation set	nominal fit value	new fit value	difference
0/90	0.4282	0.4284	0.0002
-45/45	0.3378	0.3358	0.0020

TABLE 28: Comparison of Σ values after the new fit with the nominal values for $B = 0.008$ and $D = 0.018$.

Case (ii):$B = -0.018$ and $D = -0.008$

orientation set	nominal fit value	new fit value	difference
0/90	0.4282	0.4432	0.0150
-45/45	0.3378	0.3530	0.0152

TABLE 29: Comparison of Σ values after the new fit with the nominal values for $B = -0.018$ and $D = -0.008$.

From Tables 28 and 29 we can see that the maximum systematic uncertainty due to the non-uniformity of acceptance is $\sim 1.5\%$ for the u-channel.

6.2.8 SYSTEMATICS SUMMARY

A summary of systematic uncertainties on the Σ beam asymmetries obtained for the u-channel is presented in Table 30. Total systematic uncertainty for each orientation set was found by adding individual contributions given in Table 30 in quadrature.

Study	0/90 Systematic Error	-45/45 Systematic Error
Event selection	0.050	0.040
Phase dependence	0.022	0.021
Flux normalization dependence	0.006	0.002
Background	0.004	0.004
Non-uniform acceptance	0.015	0.015
Total	0.057	0.048

TABLE 30: Summary of systematic uncertainties from the studies described in Sec. 6.2.

CHAPTER 7

RESULTS

7.1 t-CHANNEL

Figure 93 shows the results for Σ beam asymmetry for $\gamma p \to K^+\Sigma^0$ as a function of -t for 0/90 and -45/45 orientation sets. Total uncertainties for each orientation set were found from adding statistical and systematic uncertainties in quadrature. Results are compared with previous SLAC 16 GeV results and RPR-2007 model prediction at 8.5 GeV.

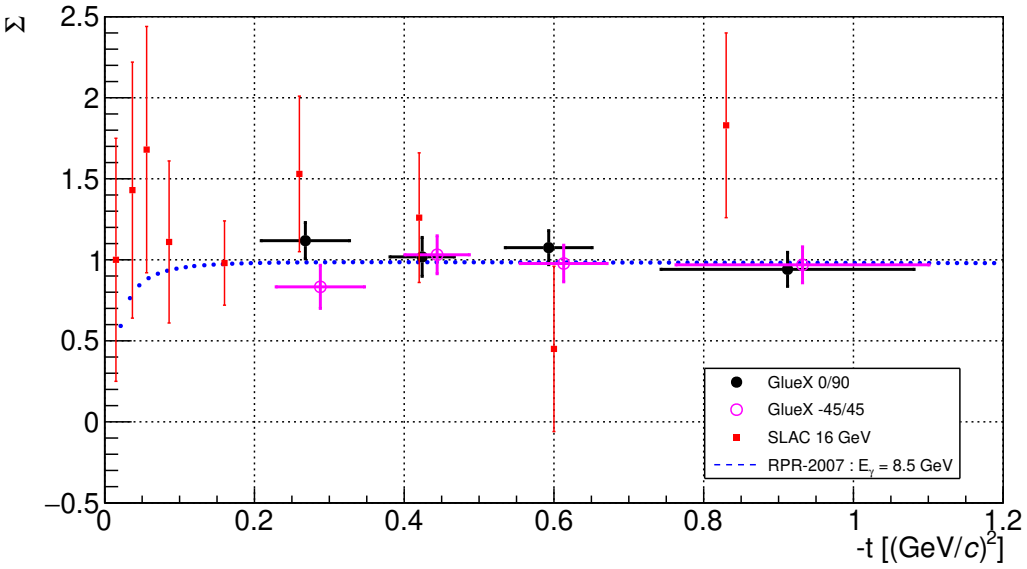

FIG. 93: The beam asymmetry Σ for $\gamma p \to K^+\Sigma^0$ in the t channel. The black solid circles correspond to the polarization direction set to 0/90, magenta open circles correspond to the polarization direction set to -45/45 (-t coordinates are shifted by 0.02 $(\mathrm{GeV}/c)^2$ to the right for clarity), vertical error bars represent total uncertainties while horizontal error bars are to indicate the RMS widths of the $-t$ bins used. Red squares are previous SLAC [7] results at $E_\gamma = 16$ GeV and the blue dotted curve represents predicted values from RPR-2007 model [14] at $E_\gamma = 8.5$ GeV.

Figure 94 shows the final result found by combining results of 0/90 and -45/45. We used a conservative approach and the larger systematic uncertainty from the two data sets were used as the average systematic uncertainty for each $-t$ bin. Combined beam asymmetry values and statistical uncertainties were found by using statistical errors of the two data sets as weights as given below following the method in Ref. [52].

The weighted average asymmetry is given by,

$$\hat{\mu} = \frac{\sum x_i/\sigma_i^2}{\sum 1/\sigma_i^2} \tag{66}$$

where x_i are measured beam asymmetry values for 0/90 and -45/45 orientation sets for a given $-t$ bin and σ_i are their statistical uncertainties.

The average error on the weighted beam asymmetry was found as,

$$\sigma(\hat{\mu}) = \sqrt{\frac{1}{\sum 1/\sigma_i^2}} \tag{67}$$

Then, total uncertainties of the combined results were found by adding the combined statistical and systematic errors in quadrature. In addition to the prediction from RPR-2007 model we added a curve (red, dashed) for the model prediction from Guidal *et al.* [53]. Both models use Regge theory and give similar prediction for beam asymmetry as a function of $-t$ for energies beyond resonance region.

Tables 31 - 33 summarize the Σ beam asymmetry results for individual orientation sets and the average result for the t-channel.

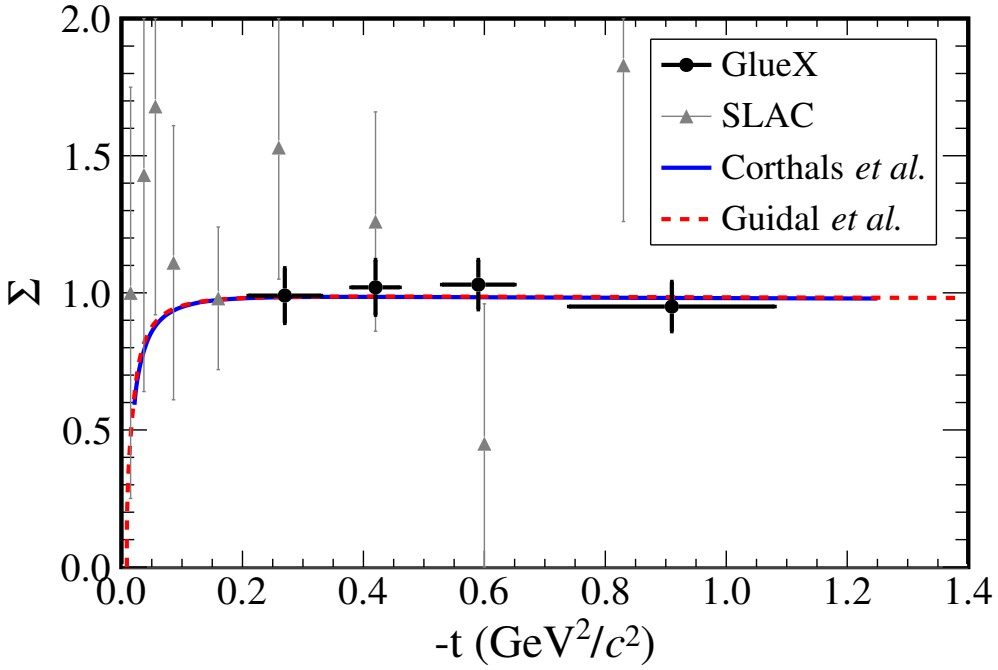

FIG. 94: Beam asymmetry Σ for $\gamma p \to K^+\Sigma^0$ in the t channel. The black solid circles correspond to combined results from 0/90 and -45/45 data sets in this analysis, vertical error bars represent total uncertainties while horizontal error bars are to indicate the RMS widths of the $-t$ bins used. Gray triangles are previous SLAC results [7] at $E_\gamma = 16$ GeV and the curves show predicted values from RPR-2007 [13, 14] (blue, solid) and Guidal *et al.* [53] (red, dashed) at $E_\gamma = 8.5$ GeV respectively.

$-t$ bin [(GeV/c)^2]	Σ	Stat. uncert.	Syst. uncert.	Total uncert.
$0.10 < -t < 0.35$	1.118	0.100	0.051	0.112
$0.35 < -t < 0.50$	1.018	0.097	0.071	0.120
$0.50 < -t < 0.70$	1.075	0.092	0.051	0.105
$0.70 < -t < 1.40$	0.941	0.092	0.051	0.105

TABLE 31: Summary of Σ beam asymmetry for the 0/90 orientation.

$-t$ bin [(GeV/c)^2]	Σ	Stat. uncert.	Syst. uncert.	Total uncert.
$0.10 < -t < 0.35$	0.833	0.114	0.068	0.133
$0.35 < -t < 0.50$	1.031	0.102	0.058	0.117
$0.50 < -t < 0.70$	0.977	0.100	0.053	0.113
$0.70 < -t < 1.40$	0.969	0.098	0.052	0.111

TABLE 32: Summary of Σ beam asymmetry for the -45/45 orientation

$-t$ bin [(GeV/c)^2]	Σ	Stat. uncert.	Syst. uncert.	Total uncert.
$0.10 < -t < 0.35$	0.994	0.075	0.068	0.101
$0.35 < -t < 0.50$	1.024	0.070	0.071	0.100
$0.50 < -t < 0.70$	1.030	0.068	0.053	0.086
$0.70 < -t < 1.40$	0.954	0.067	0.052	0.085

TABLE 33: Summary of average Σ beam asymmetry for the t-channel

7.2 u-CHANNEL

Tables 34-36 show the results for Σ beam asymmetry for $K^+\Sigma^0$ in the u-channel. Combined asymmetry values and uncertainties were found the same way as explained in Sec. 7.1.

$-u$ bin ((GeV/c)^2)	Σ	Stat. uncert.	Syst. uncert.	Total uncert.
$-u < 2.0$	0.458	0.099	0.057	0.114

TABLE 34: Summary of Σ beam asymmetry for the 0/90 orientation.

$-u$ bin ((GeV/c)^2)	Σ	Stat. uncert.	Syst. uncert.	Total uncert.
$-u < 2.0$	0.361	0.099	0.048	0.110

TABLE 35: Summary of Σ beam asymmetry for the -45/45 orientation

$-u$ bin ((GeV/c)^2)	Σ	Stat. uncert.	Syst. uncert.	Total uncert.
$-u < 2.0$	0.410	0.070	0.057	0.090

TABLE 36: Summary of average Σ beam asymmetry for the u-channel

7.3 CONCLUSION

The measurement for t-channel is the first measurement done exclusively for $K^+\Sigma^0$ beam asymmetry above the resonance region. As shown by Fig. 94, the beam asymmetry values for t-channel are close to 1. According to Eqn. 33 this implies that only the perpendicular polarized photon beam contributes to the production of $K^+\Sigma^0$ in the t-channel. Also, it tells that the natural parity exchange dominates presumably with the $K^*(892)$ meson as discussed in Sec. 2.3. Results are consistent with the predictions from RPR-2007 [13, 14] and Guidal *et al.* [53] at $E_\gamma = 8.5$ GeV. Our results have much precise statistical precision than the previous SLAC results at $E_\gamma = 16$ GeV. The SLAC measurement was done using the cross section ratios for $K^+\Lambda$ and $K^+\Sigma^0$ reactions to get the individual beam asymmetries for the two reactions. This is because they only detected the K^+ in the final state so their measurement of asymmetry included the sum of $K^+\Lambda$ and $K^+\Sigma^0$.

The u-channel beam asymmetry for $K^+\Sigma^0$ has never been measured before. As shown in Table 36 an average value of approximately 0.4 is obtained for the low $-u$ region ($-u <$ 2.0 (GeV/c)^2) measured. It indicates that in this kinematic domain, u-channel hyperon exchanges of both $\Sigma(J = 1/2)$ and $Y^*(J = 3/2)$ trajectories contribute to the production of the $K^+\Sigma^0$ final state. There is no model prediction for beam asymmetry in the low $-u$ region yet. The measurement in this work will provide valuable information for theorists to understand the exchange mechanisms contributing to kaon and in general pseudoscalar meson photoproduction.

BIBLIOGRAPHY

[1] R. Bradford *et al.* (CLAS Collaboration), "Differential cross sections for $\gamma + p \rightarrow K^+ + Y$ for Λ and Σ^0 hyperons", Phys. Rev. C **73, 035202** (2006).

[2] B. Dey *et al.* (CLAS Collaboration), "Differential cross sections and recoil polarizations for the reaction $\gamma p \rightarrow K^+\Sigma^0$", Phys. Rev. C **82, 025202** (2010).

[3] M. Tran *et al.* (SAPHIR Collaboration), "Measurement of $\gamma p \rightarrow K^+\Lambda$ and $\gamma p \rightarrow K^+\Sigma^0$ at photon energies up to 2 GeV", Phys. Lett. B **445**, 20 (1998).

[4] A. Lleres *et al.* (GRAAL Collaboration), "Polarization observable measurements for $\gamma p \rightarrow K^+\Lambda$ and $\gamma p \rightarrow K^+\Sigma^0$ for energies up to 1.5 GeV", Eur. Phys. J. A. **31**, 79 (2007).

[5] M. Sumihama *et al.* (LEPS Collaboration), "The $\vec{\gamma}p \rightarrow K^+\Lambda$ and $\vec{\gamma}p \rightarrow K^+\Sigma^0$ reactions at forward angles with photon energies from 1.5 to 2.4 GeV", Phys. Rev. C **73**, 035214 (2006).

[6] W. Briscoe, M. Doering, H. Haberzettl, I. Strakovsky and R. Workman, `http://gwdac.phys.gwu.edu/analysis/prk_analysis.html`.

[7] D. Quinn, J. Rutherford, M. Shupe, D. Sherden, R. Siemann and C. Sinclair, "Study of charged-pseudoscalar-meson photoproduction from hydrogen and deuterium with 16-GeV linearly polarized photons", Phys. Rev. D **20**, 1553 (1979).

[8] M. Gell-Mann, "The EightfoldWay: A Theory of Strong Interaction Symmetry", California Institute of Technology, USA (1961).

[9] M. Gell-Mann, "The symmetry group of vector and axial vector currents", Physics **1**, 63 (1964).

[10] M. Gell-Mann and Y. Ne'eman, *The Eightfold Way*, W. A. Benjamin (1964).

[11] G. Zweig, "An SU_3 Model for Strong Interaction Symmetry and its Breaking", CERN, report number CERN-TH-412 (1964).

[12] M. Thomson, *Modern Particle Physics*, Cambridge University Press (2013).

[13] T. Corthals, J. Ryckebusch and T. Van Cauteren, "Forward-angle $K^+\Lambda$ photoproduction in a Regge-plus-resonance approach", Phys. Rev. **C73**, 045207 (2006).

[14] T. Corthals, T. Van Cauteren, J. Ryckebusch and D.G. Ireland, "Regge-plus-resonance treatment of the $p(\gamma,K^+)\Sigma^0$ and $p(\gamma,K^0)\Sigma^+$ reactions at forward kaon angles", Phys. Rev. **C75**, 045204 (2007).

[15] M. Guidal, PhD thesis, DAPNIA/SPhN-96-03T, CE Saclay (1996).

[16] P. Stichel, "Single pion production by linearly polarized photons at high energies", Z. Phys. **180**, 170 (1964).

[17] G.F. Chew, M.L. Goldberger, F.E. Low and Y. Nambu, "Relativistic dispersion relation approach to photomeson production", Phys. Rev. **106**, 1345 (1957).

[18] G. R. Goldstein, J.F. Owens III and J. Rutherfoord, "Polarization predictions for K^+ photoproduction", Nucl. Phys. **B53**, 197, (1973).

[19] C. Reece, "Continuous Wave Superconducting Radio Frequency Electron Linac for Nuclear Physics Research", Phys. Rev. Accel. Beams. **19**, 124801 (2016).

[20] `https://www.jlab.org/physics/GeV`.

[21] E.S. Smith *et al.*, "The GlueX beam line and detector", `https://halldweb.jlab.org/doc-private/DocDB/ShowDocument?docid=4294`

[22] U. Timm, "Coherent bremsstrahlung of electrons in crystals", Fortschritt der Physik **17**, 765-808 (1969).

[23] K. Livingston, "The stonehenge technique. A method for aligning coherent bremsstrahlung radiators", Nucl. Instrum. Meth. **A 603 (3)**, 205-213 (2009).

[24] K. Mork, "Pair production by photons on electrons", Phys. Rev. **160**, 1065-1071 (1967).

[25] L. Maximon, H. Gima, "Pair production in the field of atomic electrons", Phys. Rev. **A 23**, 172-185 (1981).

[26] M. Dugger *et al.*, "Design and construction of a high-energy photon polarimeter", Nucl. Instrum. Meth. **A867**, 115-127 (2017).

[27] F. Barbosa *et al.*," Pair spectrometer hodoscope for HALL D at Jefferson Lab", Nuclear Instruments and Methods in Physics Research Section A: Accelerators, Spectrometers, Detectors and Associated Equipment, **795**, 376-380 (2015).

[28] C. Keith, "Targets for a neutral kaon beam", Jefferson Lab, Newport News, VA (2016).

[29] E. Pooser *et al.*, "The GlueX Start Counter Detector", Nucl. Instrum. Meth. **A927**, 330 (2019).

[30] E. Smith, "Time-of-Flight Measurements with the Barrel Calorimeter and the Forward Scintillators", From the GlueX Document Database, Document #1001 (2008).

[31] Y. van Haarlem *et al.*, "The GlueX Central Drift Chamber: Design and Performance", Nucl. Instrum. Meth. **A622**, 142 (2010).

[32] D. S. Carman and S. Taylor, "Hall D Forward Drift Chamber Technical Design Report", Jefferson Lab, Newport News, VA (2008).

[33] T. D. Beattie *et al.*, "Construction and performance of the barrel electromagnetic calorimeter for the GlueX experiment", Nucl. Instrum. Meth. **A896**, 24 (2018).

[34] K. Moriya *et al.*, "A Measurement of the energy and timing resolution of the GlueX Forward Calorimeter using an electron beam", Nucl. Instrum. Meth. **A726**, 60 (2013).

[35] GlueX Collaboration, Gluex photos at `https://gluexweb.jlab.org/photos`

[36] Cristiano Fanelli, "Photon energy resolution", `https://halldweb.jlab.org/doc-private/DocDB/ShowDocument?docid=3500`

[37] M. Patsyuk, "GlueX Overview: Status and Some Future Plans", `https://halldweb.jlab.org/doc-private/DocDB/ShowDocument?docid=3109`

[38] J. Stevens, "Spring 2017 Dataset Summary", `https://halldweb.jlab.org/wiki-private/index.php/Spring_2017_Dataset_Summary` (2017).

[39] `https://root.cern.ch`

[40] P. Mattione, "GlueX Analysis Software", `https://halldweb.jlab.org/wiki/index.php/GlueX_Analysis_Software` (2013).

[41] P. Mattione, "DSelector", https://halldweb.jlab.org/wiki/index.php/DSelector (2016).

[42] P. Mattione, "Spring 2017 Analysis Launch Cuts", https://halldweb.jlab.org/wiki/index.php/Spring_2017_Analysis_Launch_Cuts (2017).

[43] R. Barsotti and M.R. Shepherd, "Using machine learning to separate hadronic and electromagnetic interactions in the GlueX forward calorimeter", submitted to JINST, arXiv:2002.09530 [physics.data-an].

[44] W. McGinley, "Development of the barrel calorimeter reconstruction and measurement of the beam asymmetry (Σ) for photoproduced π^0 and η mesons with the GlueX experiment", Ph.D. Thesis, Carnegie Mellon University (2019).

[45] H. Al Ghoul *et al.* (GlueX Collaboration), "Measurement of the beam asymmetry Σ for π^0 and η photoproduction on the proton at $E_\gamma = 9$ GeV", Phys. Rev. **C 95**, 042201(R) (2017).

[46] A. Austregesilo, "Orientations of the photon beam polarization from $\rho(770)$ decay asymmetries",https://halldweb.jlab.org/doc-private/DocDB/ShowDocument?docid=3977 (2019).

[47] E. Smith, "Finite bin corrections in 1-dimension", https://misportal.jlab.org/ul/Physics/Hall-B/clas/viewFile.cfm/2006-007.pdf?documentId=264 (2006).

[48] C.A. Paterson *et al.* (CLAS Collaboration), "Photoproduction of Λ and Σ^0 hyperons using linearly polarized photons", Phys. Rev. **C 93**, 065201 (2016).

[49] R. Bradford, "Measurement of differential cross sections and C_x and C_z for $\gamma p \to K^+\Lambda$ and $\gamma p \to K^+\Sigma^0$ using CLAS at Jefferson Lab", Ph.D. thesis, Carnegie Mellon University (2005).

[50] M. Ablikim *et al.* (BESIII Collaboration), "Polarization and entanglement in baryonantibaryon pair production in electronpositron annihilation", Nature Phys. **15**, 631 (2019).

[51] I.S. Barker, A. Donnachie and J.K. Storrow, "Complete Experiments in Pseudoscalar Photoproduction", Nucl. Phys. **B95**, 347 (1975).

[52] W. Leo, https://ned.ipac.caltech.edu/level5/Leo/Stats4_5.html

[53] M. Guidal, M. Laget and J. -M. Vanderhaeghen, "Pion and kaon photoproduction at high energies: forward and intermediate angles", Nucl. Phys. **A627**, 645 (1997).

APPENDIX A

LIST OF GLUEX SPRING 2017 RUNS

A.1 0/90 PARA (69 RUNS)

31031 31000 30999 30998 30964 30963 30954 30953 30924 30923 30893 30890 30844 30843 30833 30830 30829 30813 30812 30802 30801 30780 30779 30743 30742 30736 30731 30694 30686 30677 30672 30658 30654 30649 30637 30627 30622 30621 30611 30598 30597 30587 30580 30579 30568 30494 30486 30474 30466 30461 30451 30441 30429 30428 30424 30422 30408 30380 30355 30345 30343 30329 30327 30323 30322 30321 30283 30282 30279

A.2 0/90 PERP (78 RUNS)

31046 31029 30996 30995 30962 30961 30952 30951 30947 30920 30903 30902 30891 30889 30859 30858 30842 30841 30840 30827 30826 30824 30811 30810 30809 30800 30797 30796 30778 30770 30741 30740 30735 30730 30701 30693 30684 30676 30668 30657 30653 30648 30636 30626 30625 30620 30610 30596 30595 30586 30578 30577 30567 30499 30493 30490 30485 30473 30465 30460 30450 30447 30446 30442 30432 30431 30410 30409 30383 30381 30361 30346 30344 30330 30326 30324 30281 30280

A.3 -45/45 PARA (74 RUNS)

31032 31002 31001 30966 30965 30956 30955 30927 30926 30896 30895 30848 30847 30835 30834 30816 30815 30804 30803 30784 30783 30745 30744 30737 30733 30732 30696 30695 30688 30687 30679 30678 30673 30659 30655 30650 30638 30630 30629 30623 30612 30607 30602 30600 30590 30589 30582 30581 30570 30496 30495 30487 30480 30477 30468 30467 30463 30462 30453 30452 30448 30433 30420 30411 30404 30403 30385 30384 30349 30347 30331 30299 30285 30284

A.4 -45/45 PERP(69 RUNS)

31034 31004 31003 30994 30993 30958 30957 30929 30928 30899 30898 30856 30855 30838 30836 30821 30818 30807 30805 30787 30785 30754 30749 30738 30734 30697 30690 30680 30675 30674 30666 30660 30656 30651 30643 30642 30641 30639 30633 30632 30624 30616

30614 30608 30592 30591 30571 30497 30488 30484 30482 30481 30470 30469 30464 30454 30449 30434 30421 30402 30401 30387 30386 30350 30348 30332 30300 30298 30286

APPENDIX B

PARAMETERS FOR MC

- software version set: version_recon-2017_01-ver03_8.xml
- halld_recon software version: recon-2017_01-ver03_hdr
- halld_sim software version: 4.2.0
- generator used: genr8
- random trigger background input: Random:recon-2017_01-ver03
- run range: 30274-31057
- no of events generated: 10 million
- Geant version: 3 and 4 (version 3 was used for all the figures in this thesis. Version 4 was used for comparison of acceptance.)
- photon beam energy: 8.2 GeV - 8.8 GeV
- t-slopes used are, (extracted from data)
  - $K^+\Sigma^0$ t-channel = 3.654
  - $K^+\Sigma^0$ u-channel = 3.21
  - $K^+\Lambda$ t-channel = 3.792
  - $K^+\Lambda$ u-channel = 3.064
- After reconstruction, ReactionFilter plugin was applied with the version set version_4.3.0.xml in order to get FCAL shower quality values into the tree.

APPENDIX C

FIT RESULTS

C.1 FIT RESULTS FOR t-CHANNEL

Figures 95-102 show the fit results for each individual $-t$ bin, with panels for the PARA (upper left), PERP (upper right), asymmetry (lower left) and sum (lower right) as described for Fig. 58.

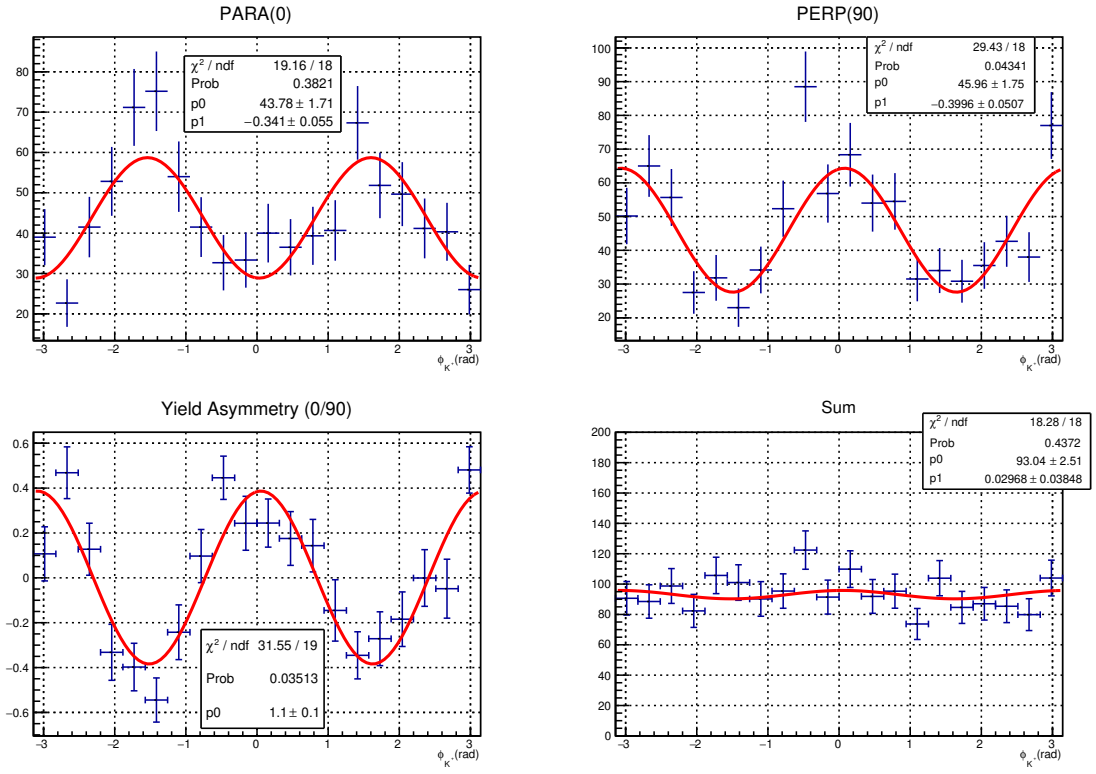

FIG. 95: Polarization direction set to 0/90. Fits to the ϕ distributions for 0.10 GeV^2 $< -t <$ 0.35 GeV^2. The orientation of the plots is the same as Fig. 58.

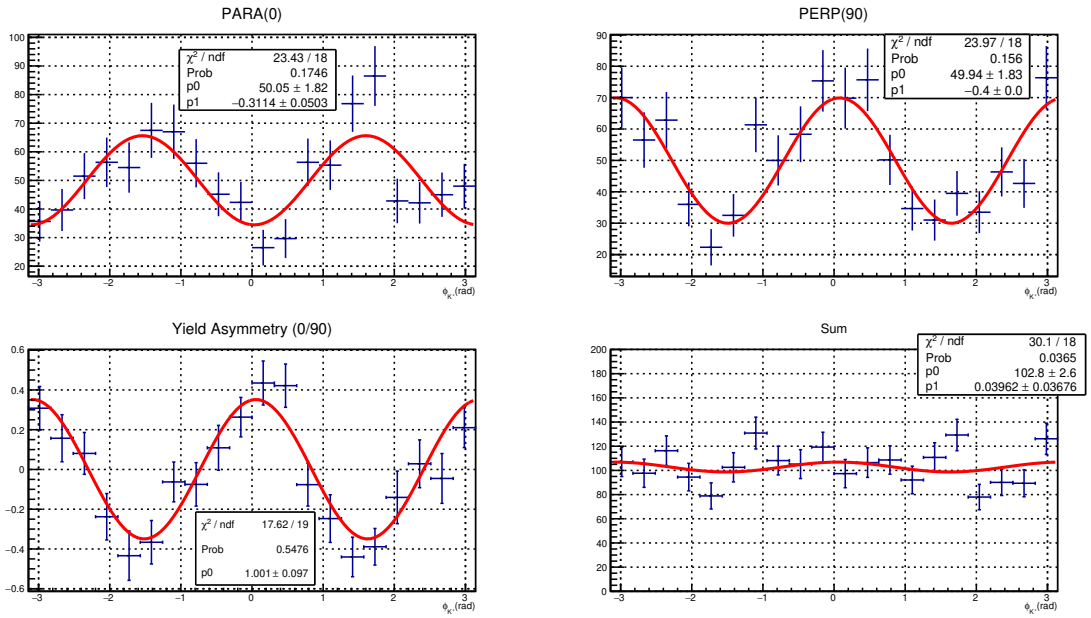

FIG. 96: Polarization direction set to 0/90. Fits to the ϕ distributions for 0.35 GeV^2 $< -t <$ 0.50 GeV^2. The orientation of the plots is the same as Fig. 58.

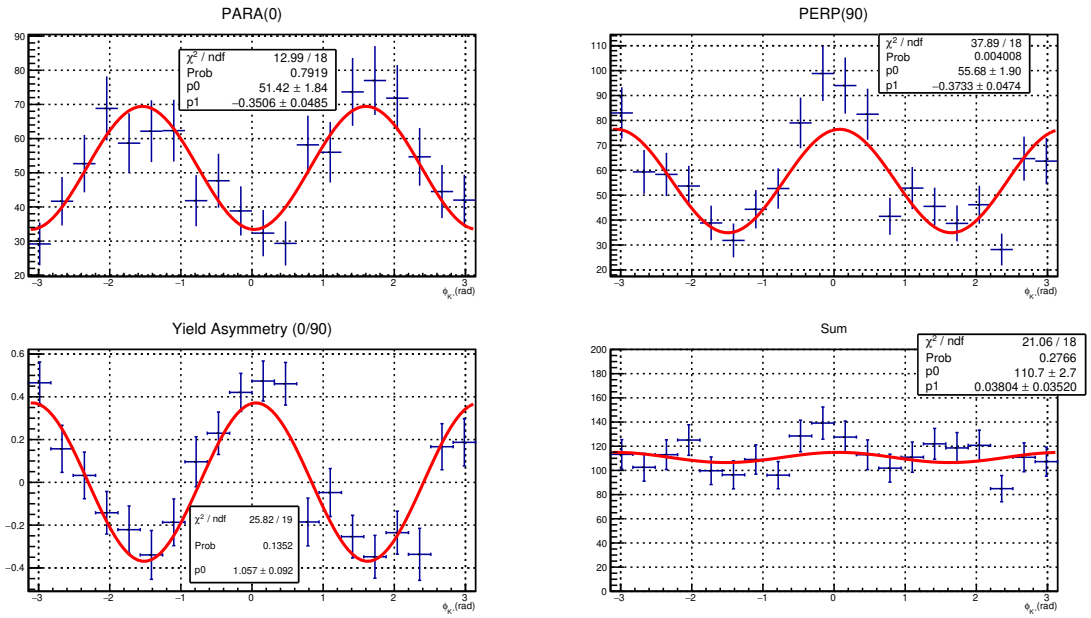

FIG. 97: Polarization direction set to 0/90. Fits to the ϕ distributions for 0.50 GeV^2 $< -t <$ 0.70 GeV^2. The orientation of the plots is the same as Fig. 58.

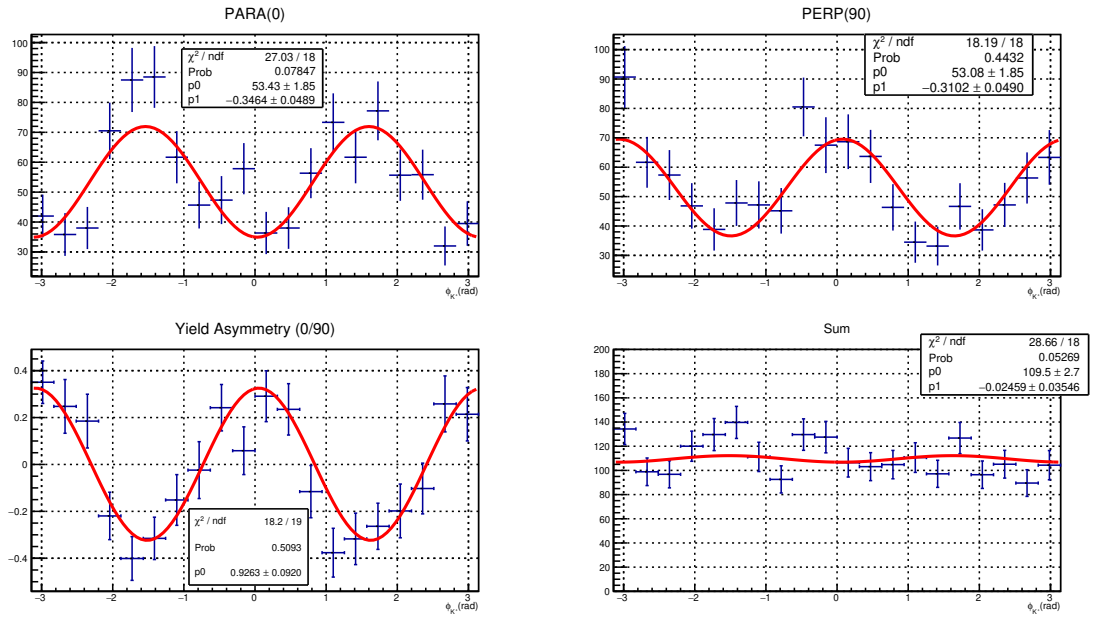

FIG. 98: Polarization direction set to 0/90. Fits to the ϕ distributions for 0.70 GeV^2 $< -t <$ 1.40 GeV^2. The orientation of the plots is the same as Fig. 58.

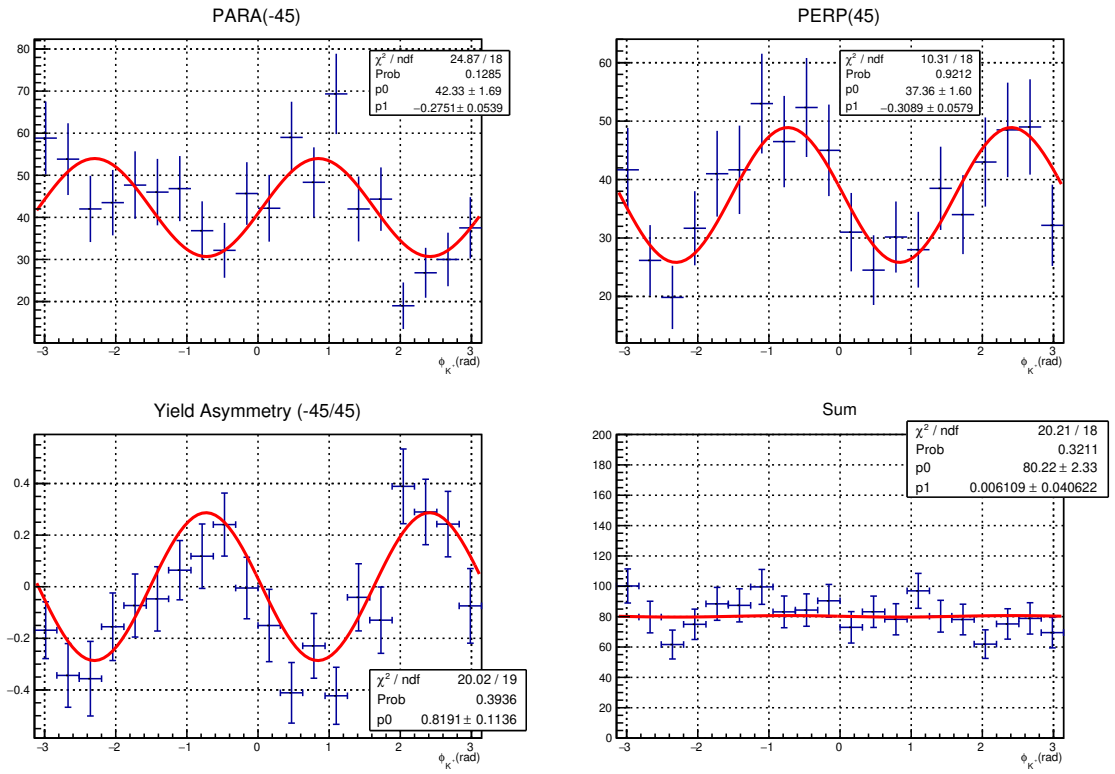

FIG. 99: Polarization direction set to -45/45. Fits to the ϕ distributions for 0.10 GeV^2 $< -t <$ 0.35 GeV^2. The orientation of the plots is the same as Fig. 58.

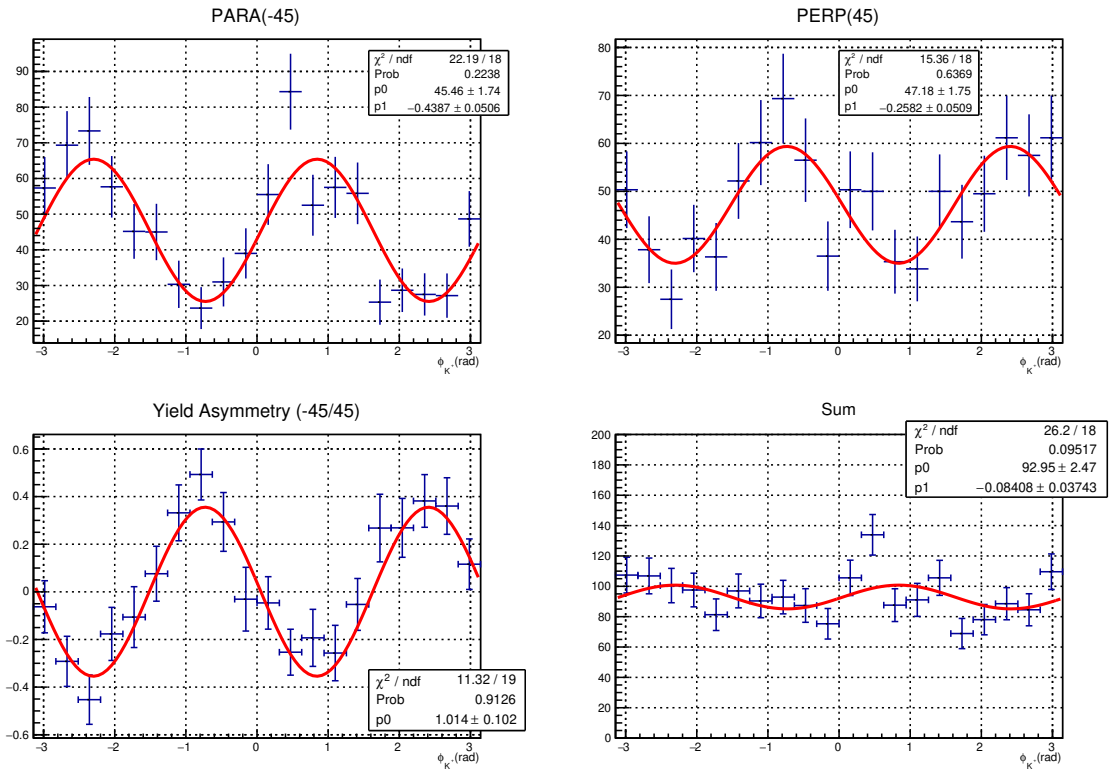

FIG. 100: Polarization direction set to -45/45. Fits to the ϕ distributions for 0.35 GeV^2 $< -t <$ 0.50 GeV^2. The orientation of the plots is the same as Fig. 58.

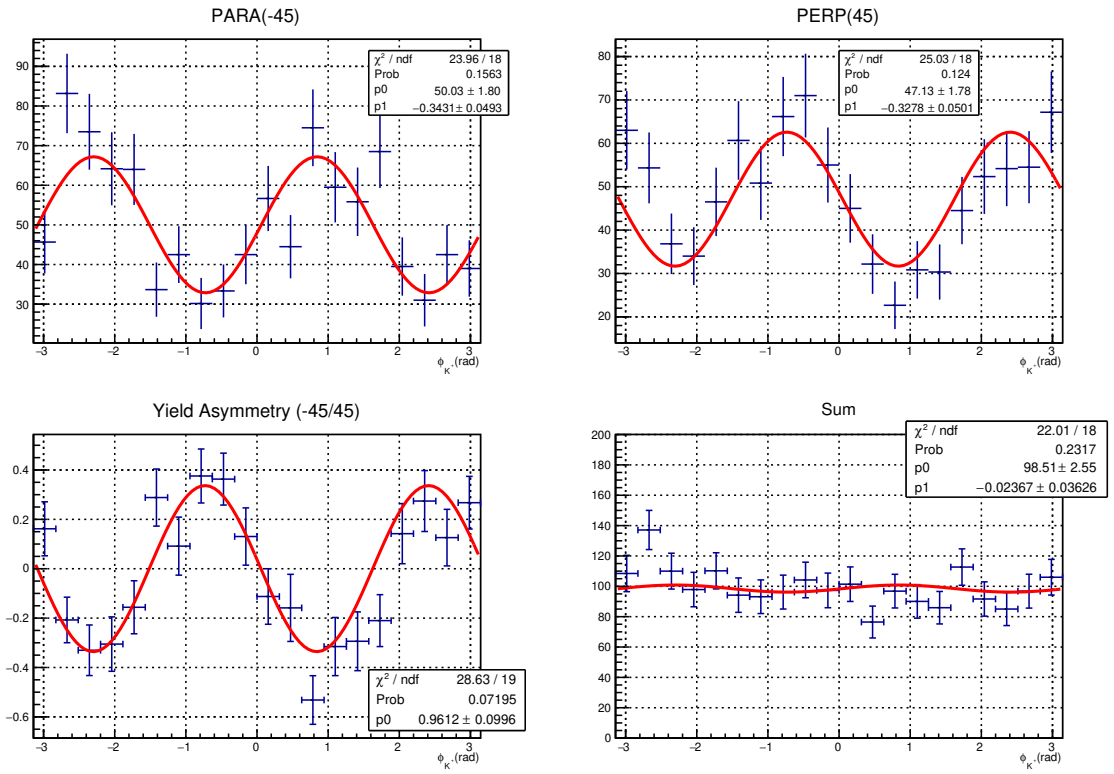

FIG. 101: Polarization direction set to -45/45. Fits to the ϕ distributions for 0.50 GeV^2 $< -t <$ 0.70 GeV^2. The orientation of the plots is the same as Fig. 58.

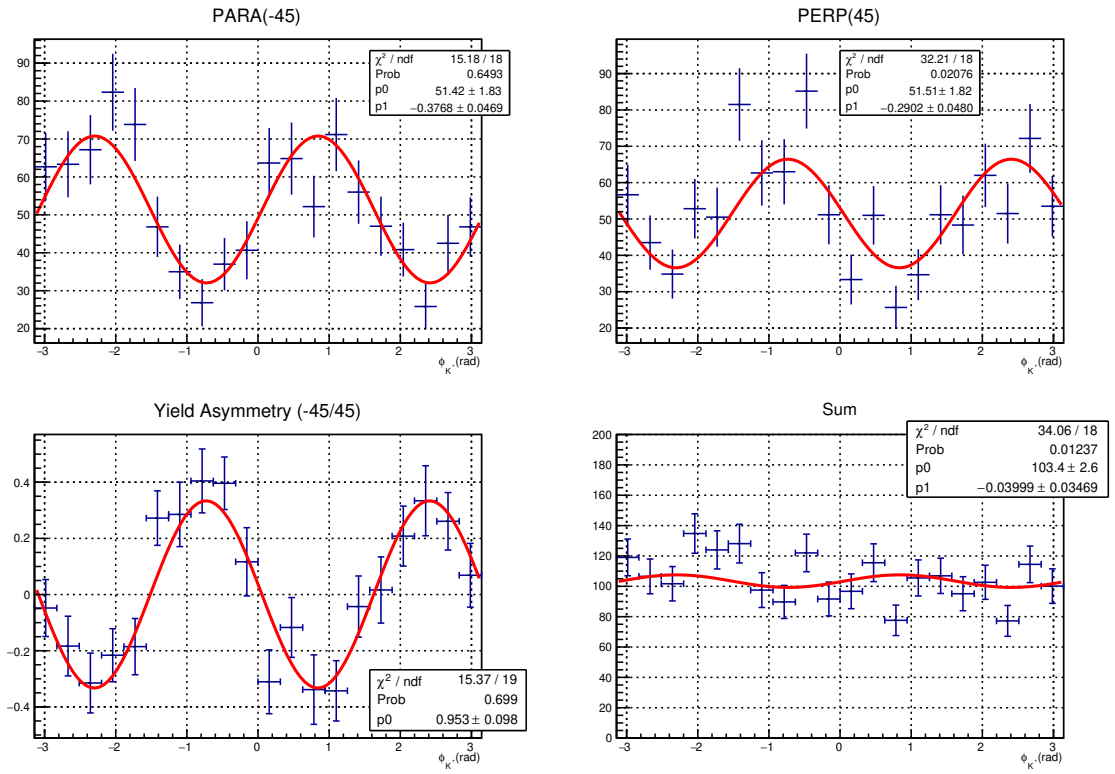

FIG. 102: Polarization direction set to -45/45. Fits to the ϕ distributions for 0.70 GeV^2 $< -t <$ 1.40 GeV^2. The orientation of the plots is the same as Fig. 58.

C.2 LINEAR FITS TO u-CHANNEL YIELD ASYMMETRY

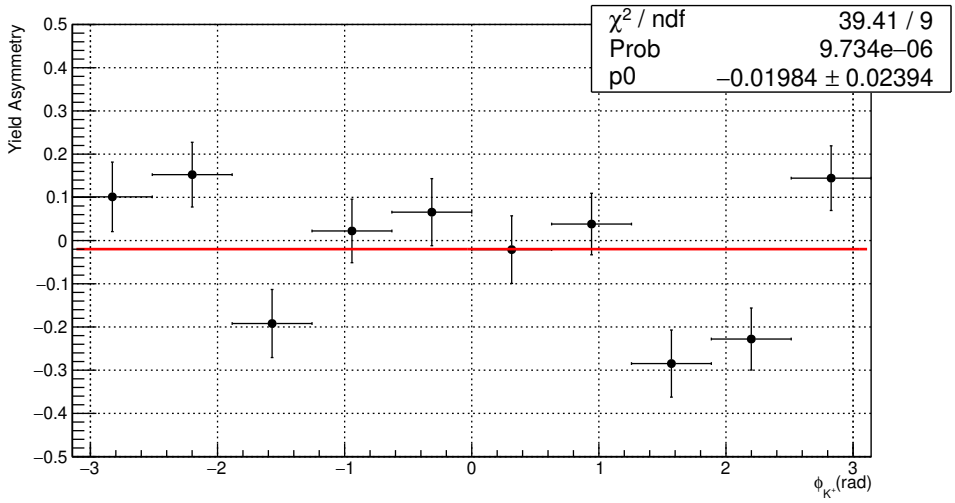

FIG. 103: Polarization direction set to 0/90. Linear fit to the yield asymmetry.

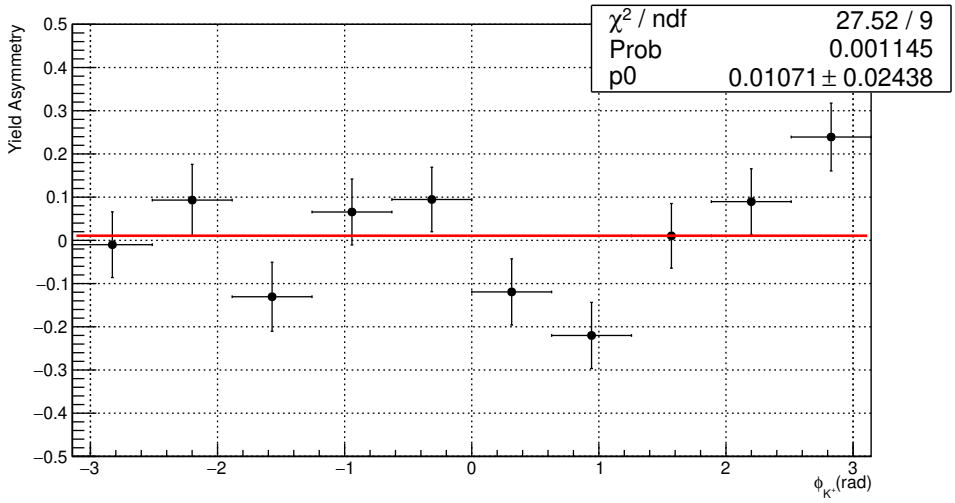

FIG. 104: Polarization direction set to -45/45. Linear fit to the yield asymmetry.

C.3 FITS TO YIELD ASYMMETRY FROM COMBINED DATA SET

In order to cross check the average beam asymmetry results obtained from the 0/90 and -45/45 sets we made an event sample combining the events from all 4 orientations. The following fits were done with Eqn. 46 for the $-t$ bins and the $-u$ bin in this event sample. Average values of polarization and flux ratio were used and they are,

$P_{\parallel} = 0.3525$

$P_{\perp} = 0.3478$

$F_R = 1.01689$

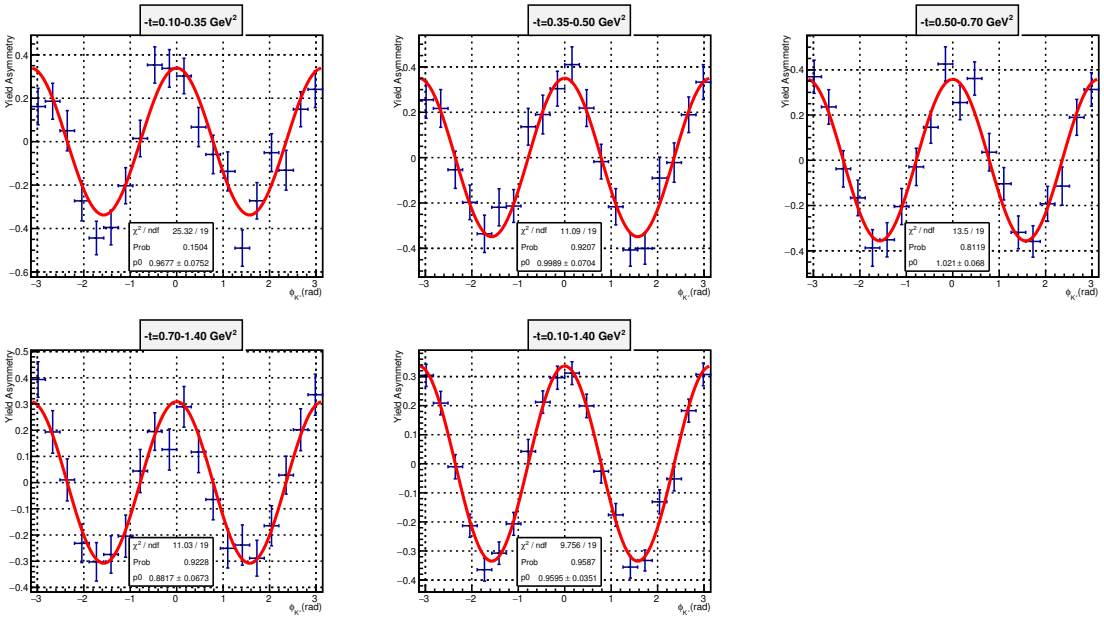

FIG. 105: Fits to yield asymmetry from combined data set from 0/90 and -45/45 for t-channel. Beam asymmetry values and statistical uncertainties are consistent with the average asymmetry results given in Table 33.

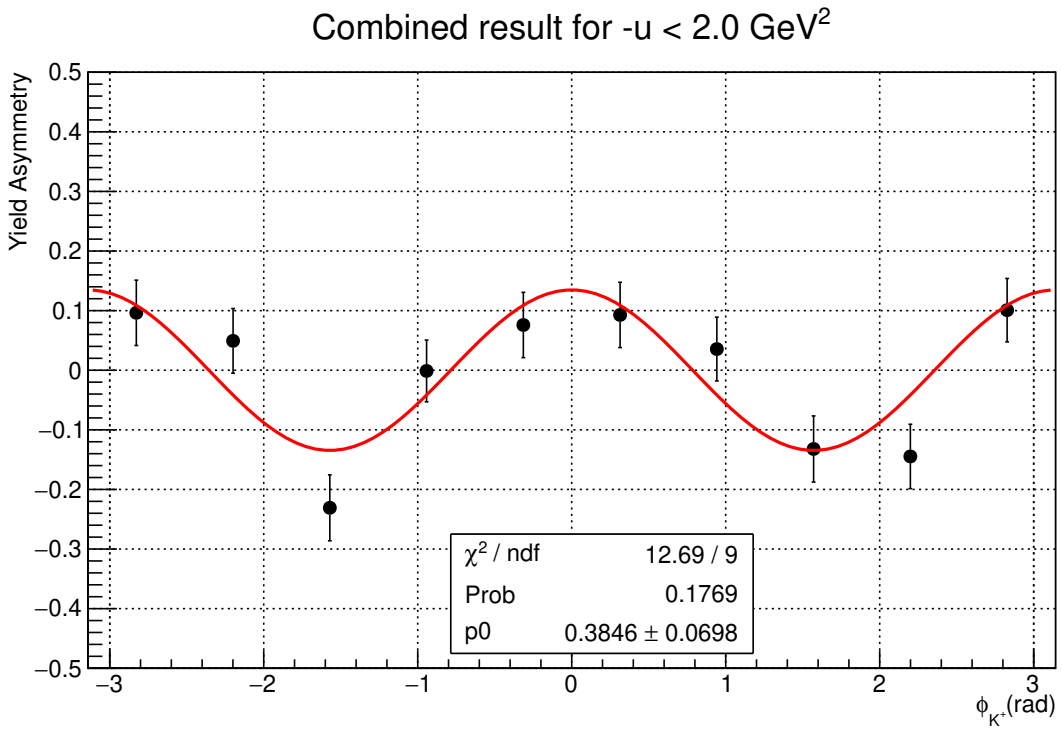

FIG. 106: Fit to the yield asymmetry from combined data set from 0/90 and -45/45 for u-channel. Beam asymmetry value and statistical uncertainty are consistent with the average asymmetry result given in Table 36.

APPENDIX D

ADDITIONAL PLOTS

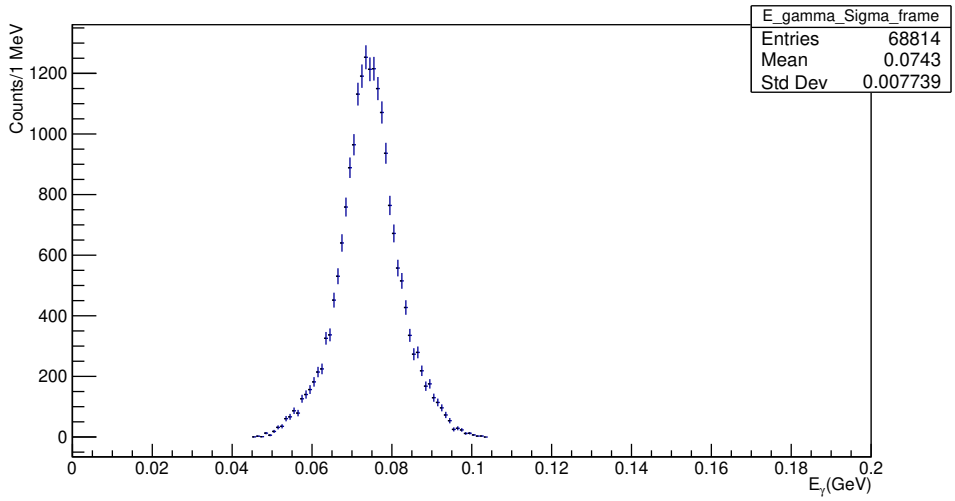

FIG. 107: Distribution of photon energy in the Σ^0 rest frame.

$\Sigma^0 \to \Lambda\gamma$

So, in the Σ^0 rest frame, $(p_\Sigma - p_\gamma)^2 = p_\Lambda^2$

$\implies M_\Sigma^2 - 2E_\gamma M_\Sigma = M_\Lambda^2$

$\implies E_\gamma = \frac{M_\Sigma^2 - M_\Lambda^2}{2M_\Sigma} = 74.5$ MeV

The mean value of distribution in Fig. 107 is consistent with the calculated value.

D.1 K^+ Z-VERTEX STUDY

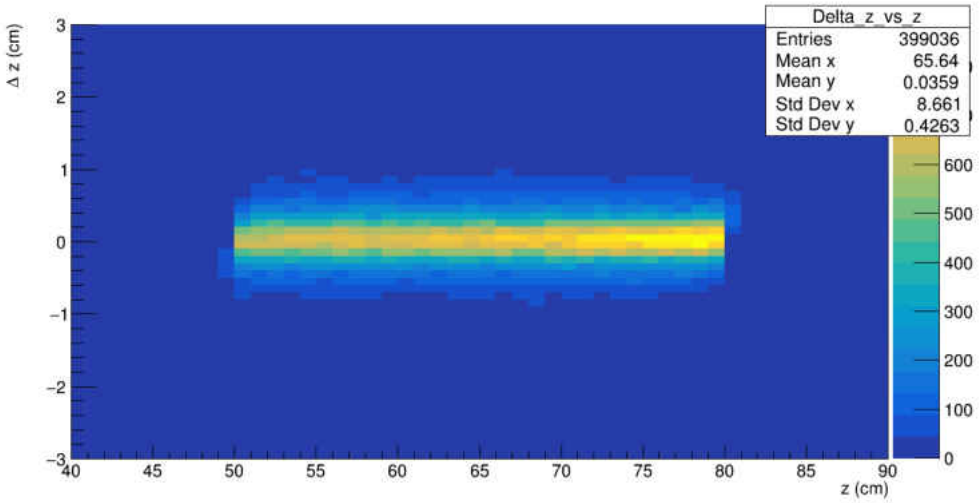

FIG. 108: $K^+\Delta z$ vs. z event by event, where $\Delta z = z_{recon} - z_{gen}$ is the difference between the thrown and reconstructed z positions.

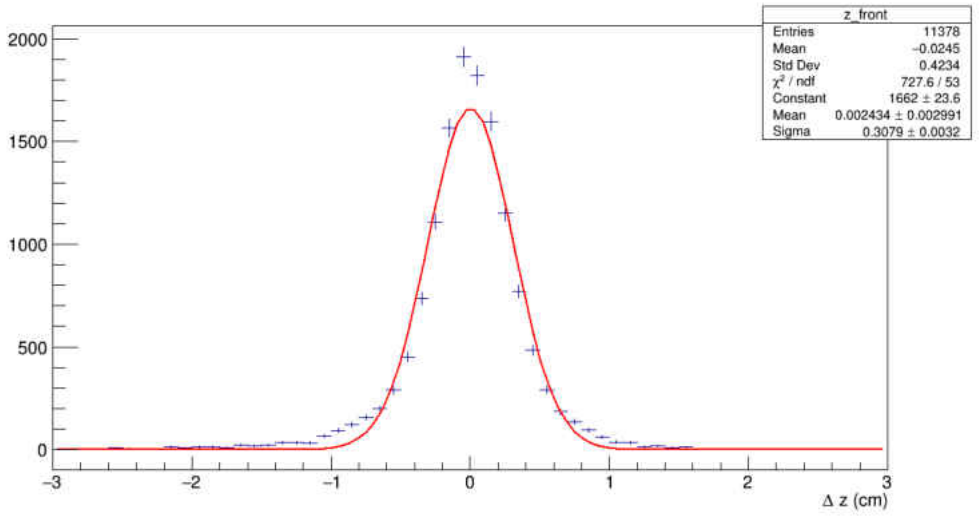

FIG. 109: A Gaussian fitted to the projection from $z = 48 - 52$ cm region. The resolution is σ=0.308±0.003 cm.

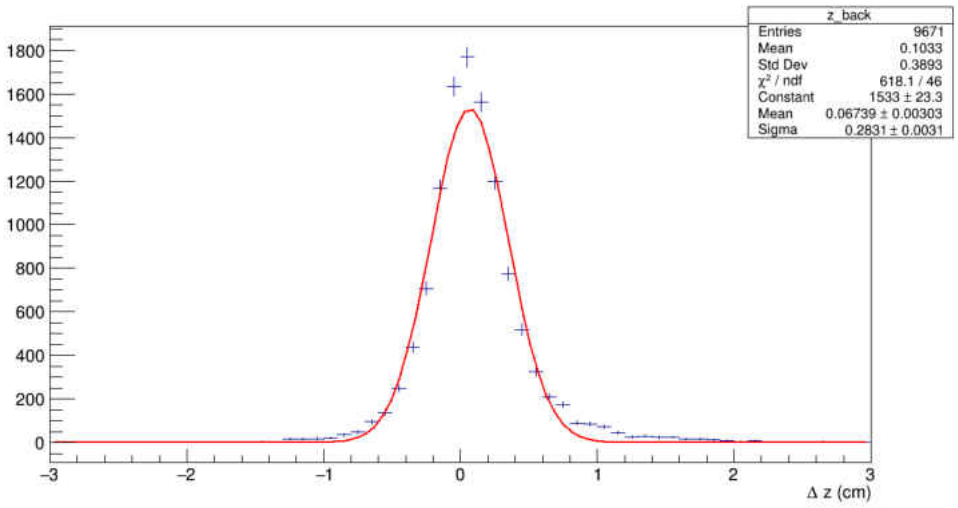

FIG. 110: A Gaussian fitted to the projection from $z = 78 - 82$ cm region. The resolution is σ=0.283±0.003 cm.

D.2 ACCEPTANCE FROM MC

Distributions for accepted events were made with the thrown P4 vectors. Geant4 shows a higher acceptance than Geant3 for both $K^+\Sigma^0$ and $K^+\Lambda$ reactions, in the entire $-t$ range (Fig. 112 and Fig. 116) for the t-channel. For u-channel, the higher acceptance in Geant4 is seen in the region $-u < 0.5$ (GeV/c)^2 (Fig. 114 and Fig. 118).

D.2.1 $K^+\Sigma^0$ t-CHANNEL

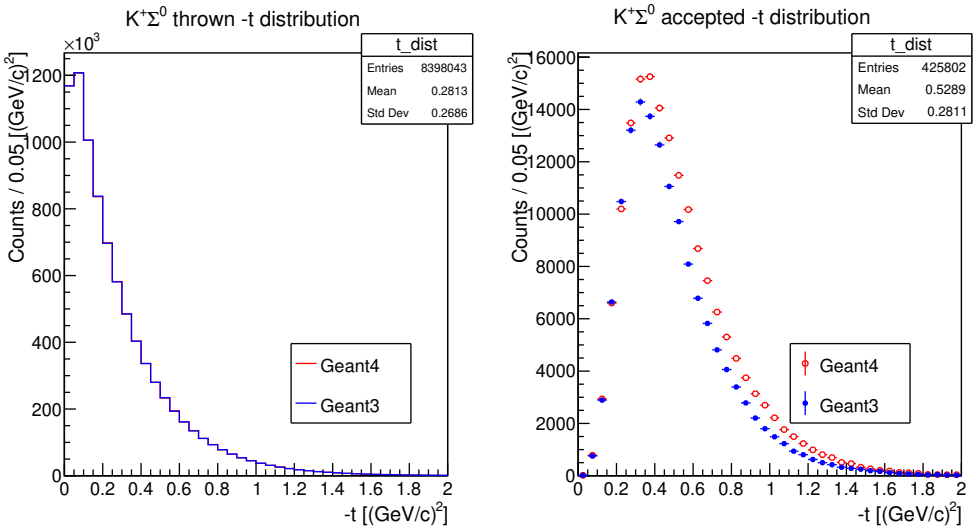

FIG. 111: $K^+\Sigma^0$ t-channel thrown (left) and accepted (right) -t distributions.

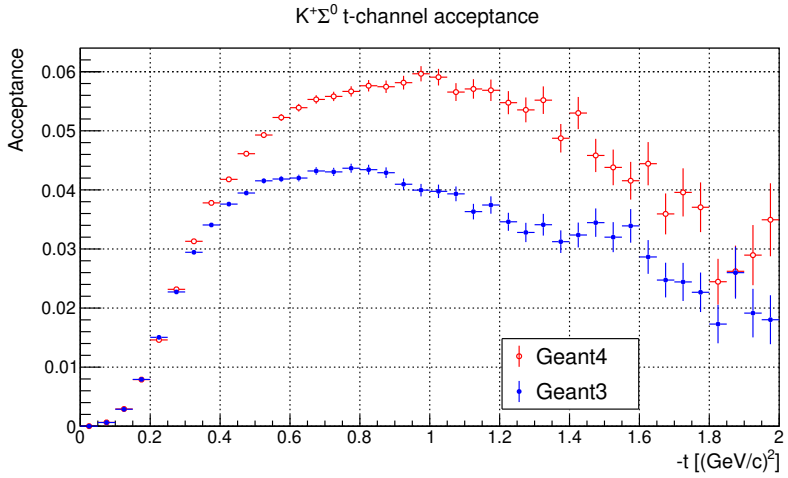

FIG. 112: Acceptance for $K^+\Sigma^0$ t-channel.

D.2.2 $K^+\Sigma^0$ u-CHANNEL

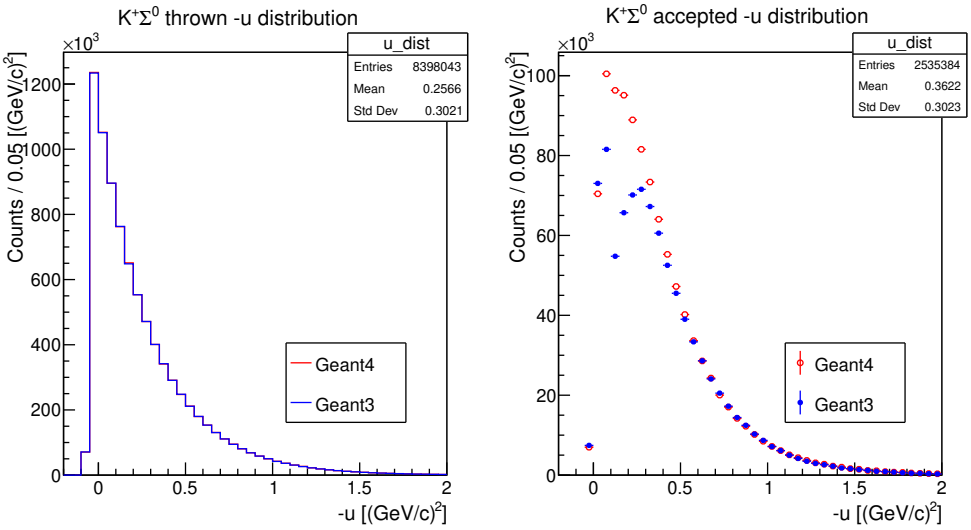

FIG. 113: $K^+\Sigma^0$ u-channel thrown (left) and accepted (right) -u distributions.

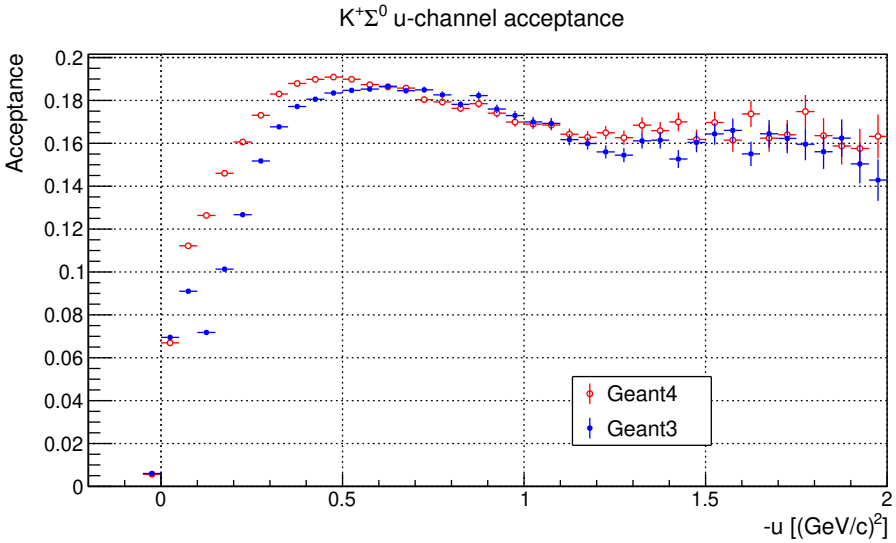

FIG. 114: Acceptance for $K^+\Sigma^0$ u-channel.

D.2.3 $K^+\Lambda$ t-CHANNEL

For $K^+\Lambda\gamma$ accepted $-t$ distribution plots of $K^+\Lambda$ reaction, cuts on $M_{\Lambda\gamma}$ and shower quality were not used as this is the background reaction for $K^+\Sigma^0$.

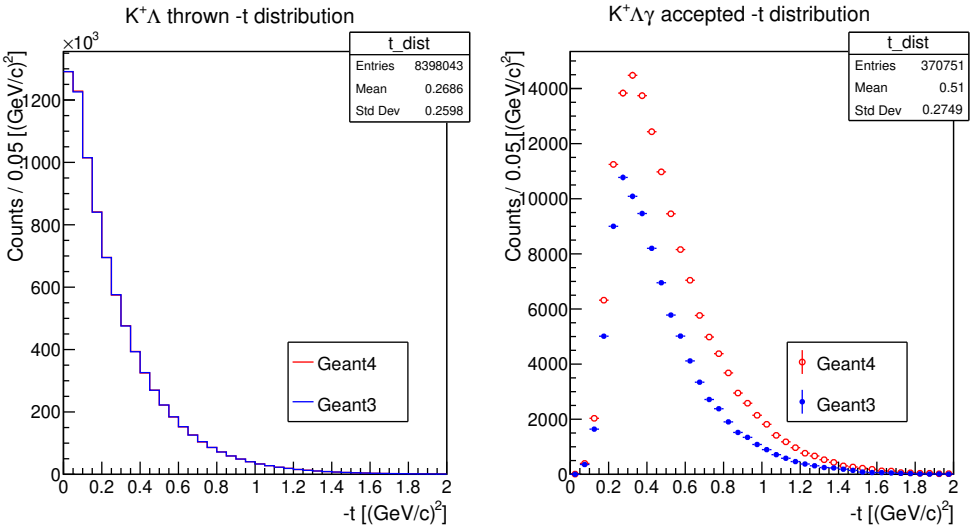

FIG. 115: $K^+\Lambda$ t-channel thrown (left) and $K^+\Lambda\gamma$ accepted (right) -t distributions.

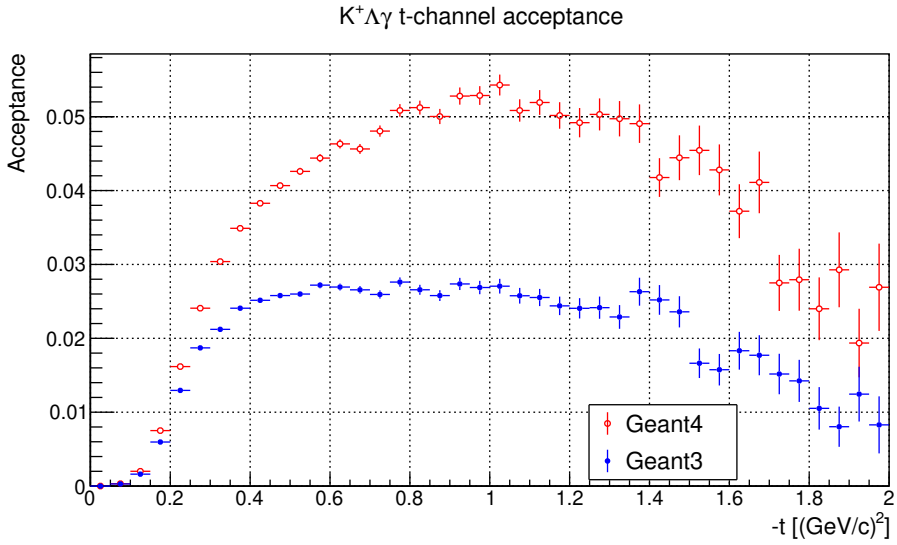

FIG. 116: Acceptance for $K^+\Lambda\gamma$ t-channel.

D.2.4 $K^+\Lambda$ u-CHANNEL

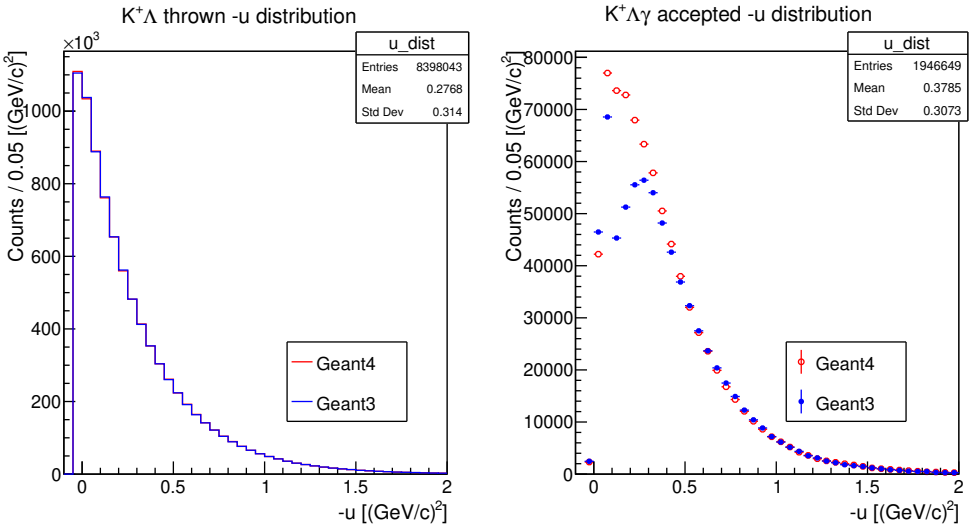

FIG. 117: $K^+\Lambda$ u-channel thrown (left) and $K^+\Lambda\gamma$ accepted (right) -u distributions.

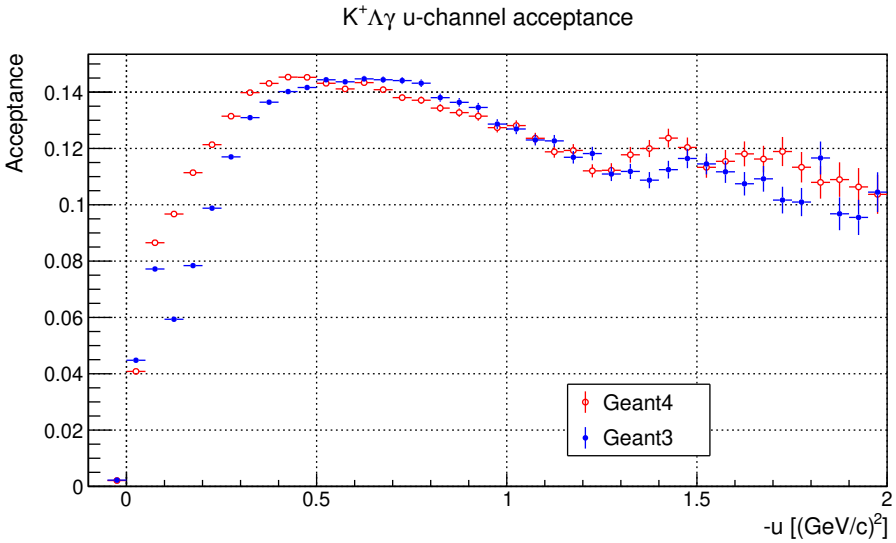

FIG. 118: Acceptance for $K^+\Lambda\gamma$ u-channel.

D.3 BACKGROUND UNDER THE Σ^0 PEAK FOR DIFFERENT BINS OF t AND u

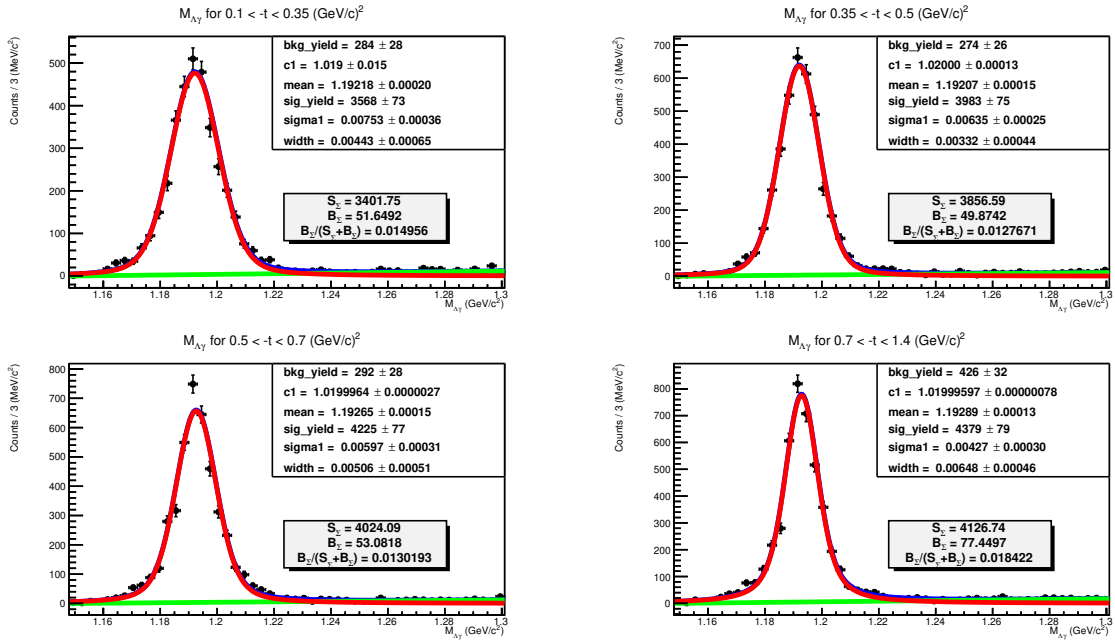

FIG. 119: The fraction of background under Σ^0 peak ($\frac{B_\Sigma}{S_\Sigma+B_\Sigma}$) for the $-t$ bins used in the analysis. B_Σ and S_Σ are background and signal yields within the range 1.169 GeV/c^2 $< M_{\Lambda\gamma} <$ 1.217 GeV/c^2 respectively.

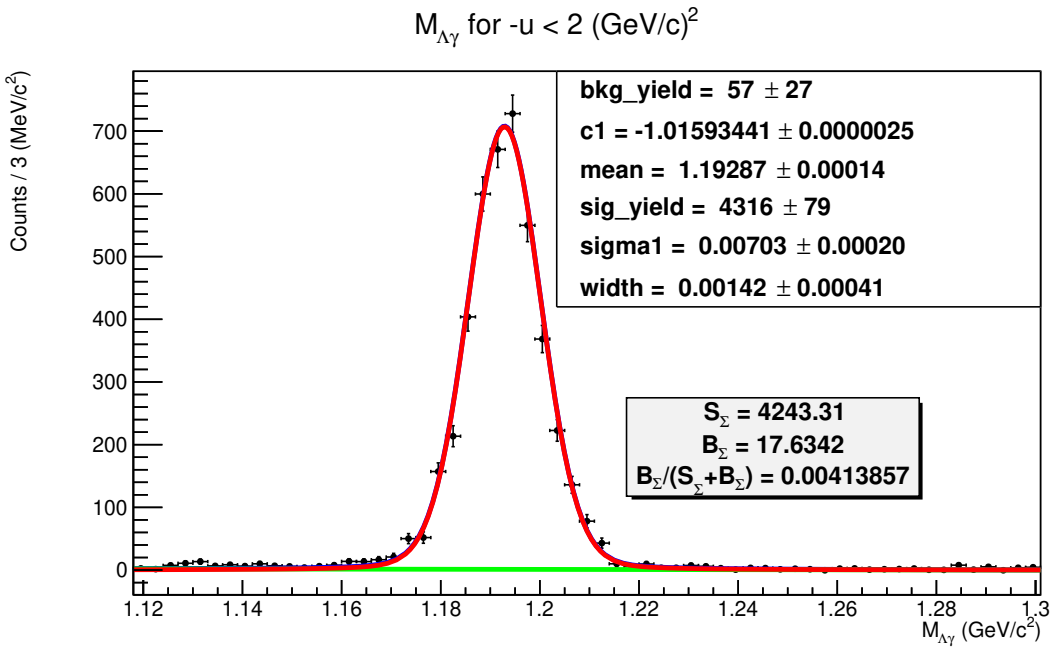

FIG. 120: The fraction of background under Σ^0 peak ($\frac{B_\Sigma}{S_\Sigma+B_\Sigma}$) for the $-u$ bin used in the analysis.

APPENDIX E

CUT STUDY

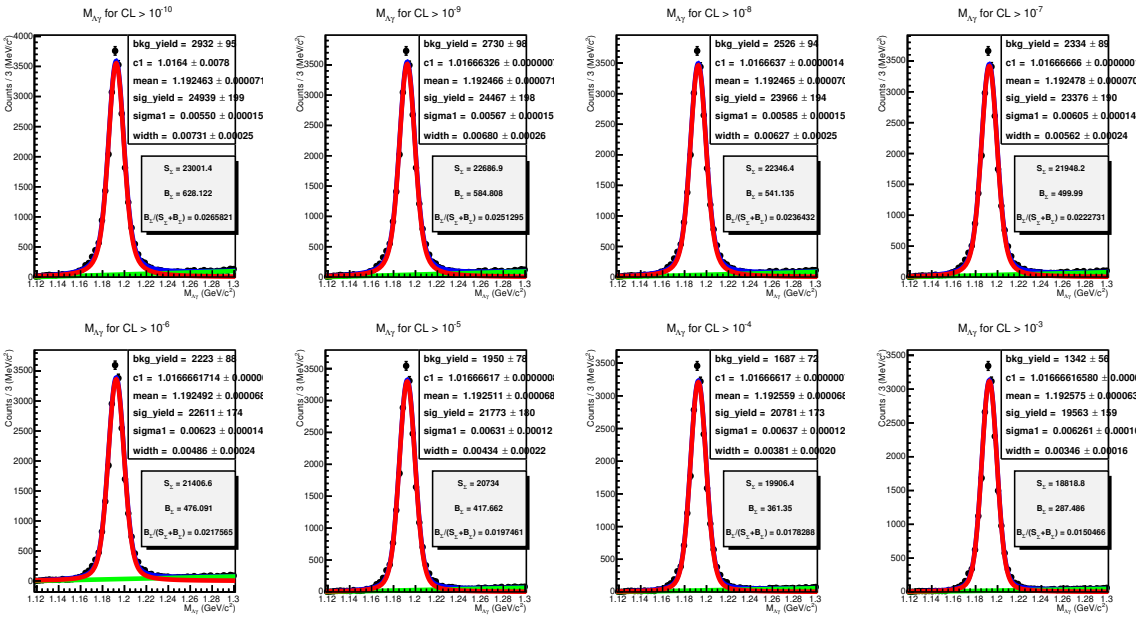

FIG. 121: Invariant mass of $\Lambda\gamma$ for different values of kinematic fit confidence level cut. S_Σ and B_Σ are signal and background yields within the range 1.169 GeV/c^2 $< M_{\Lambda\gamma} <$ 1.217 GeV/c^2.

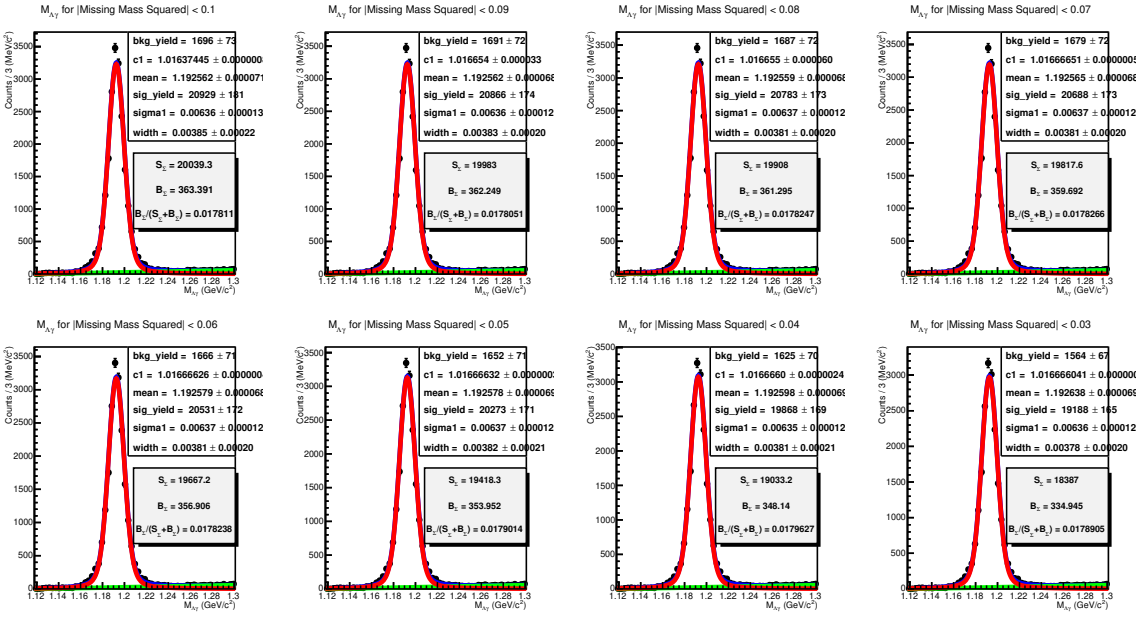

FIG. 122: Invariant mass of $\Lambda\gamma$ for different values of measured missing mass squared cut.

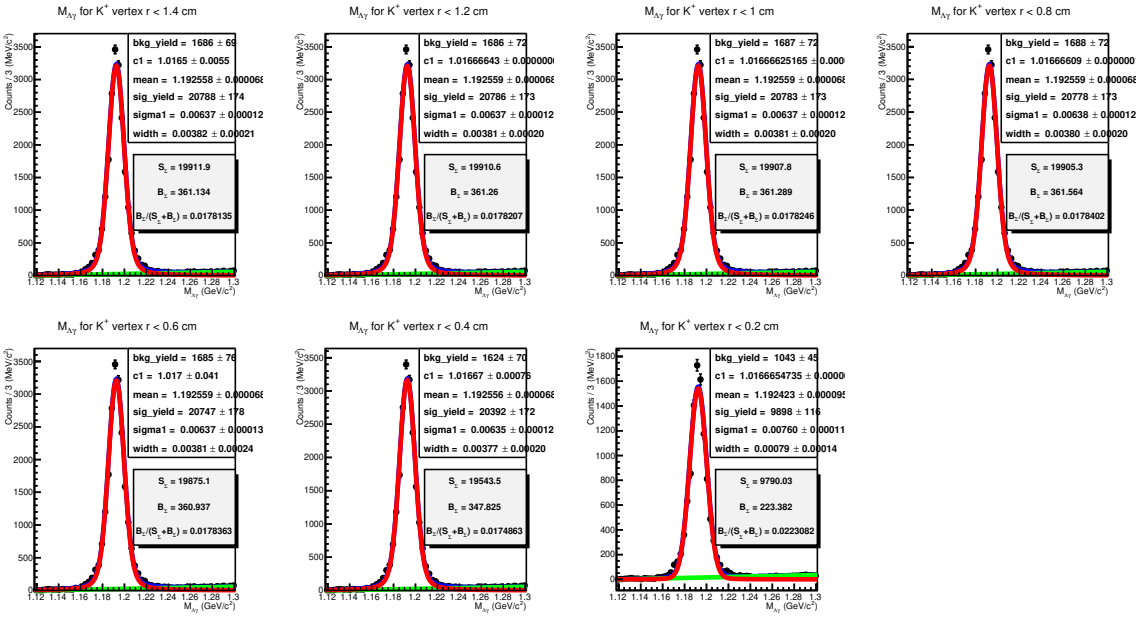

FIG. 123: Invariant mass of $\Lambda\gamma$ for different values of K^+ vertex radial position cut.

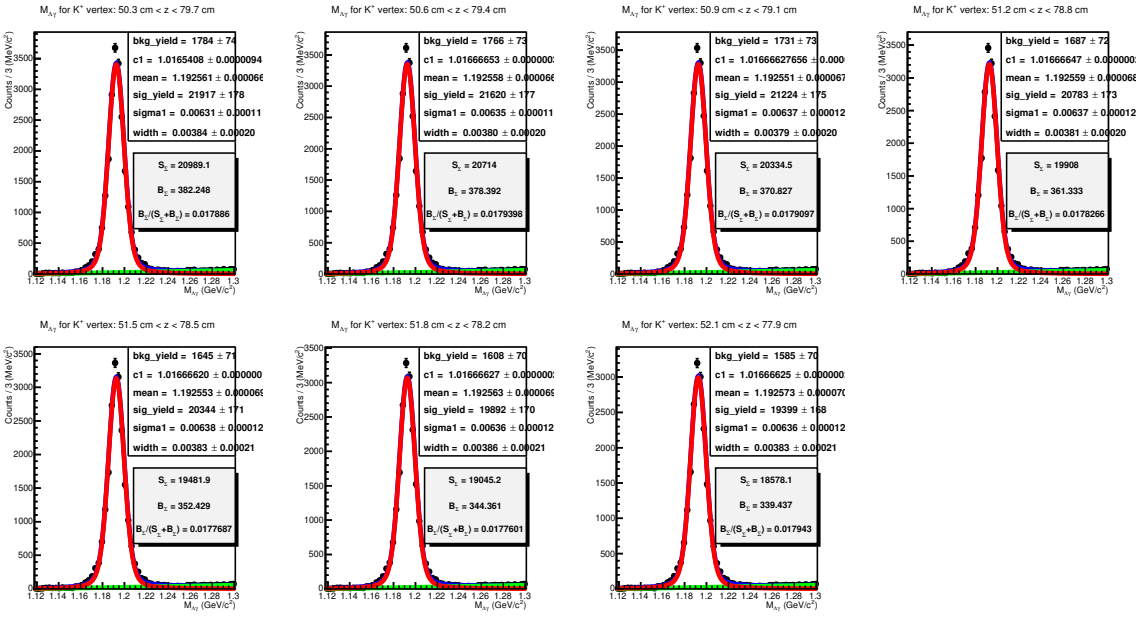

FIG. 124: Invariant mass of $\Lambda\gamma$ for different values of K^+ vertex z position cut.

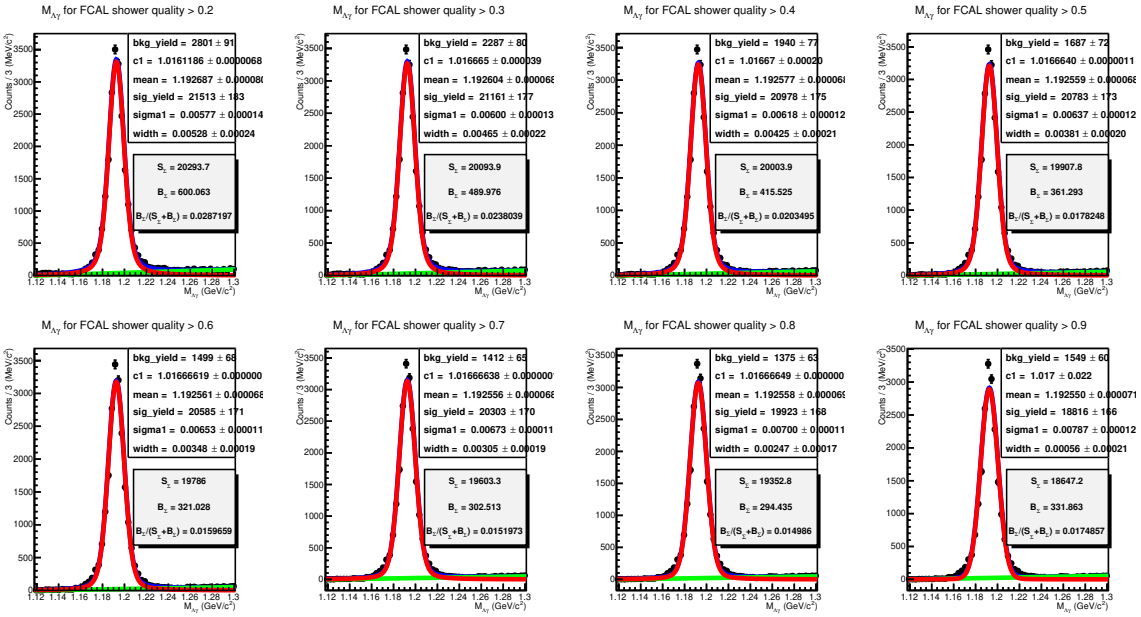

FIG. 125: Invariant mass of $\Lambda\gamma$ for different values of FCAL shower quality cut.

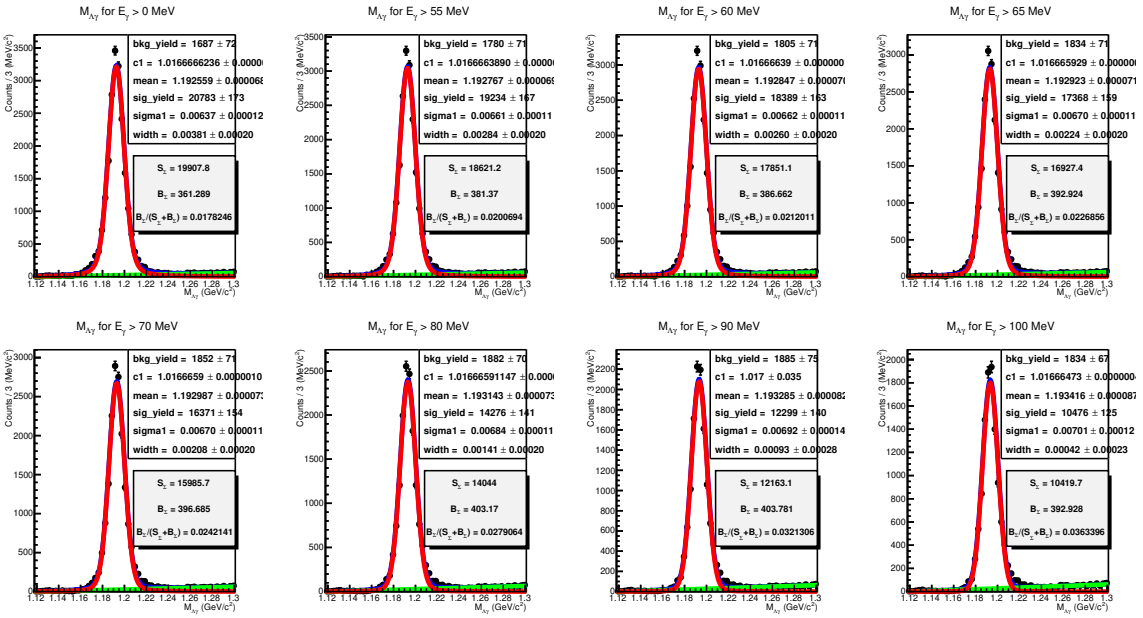

FIG. 126: Invariant mass of $\Lambda\gamma$ for different values of minimum photon energy cut.

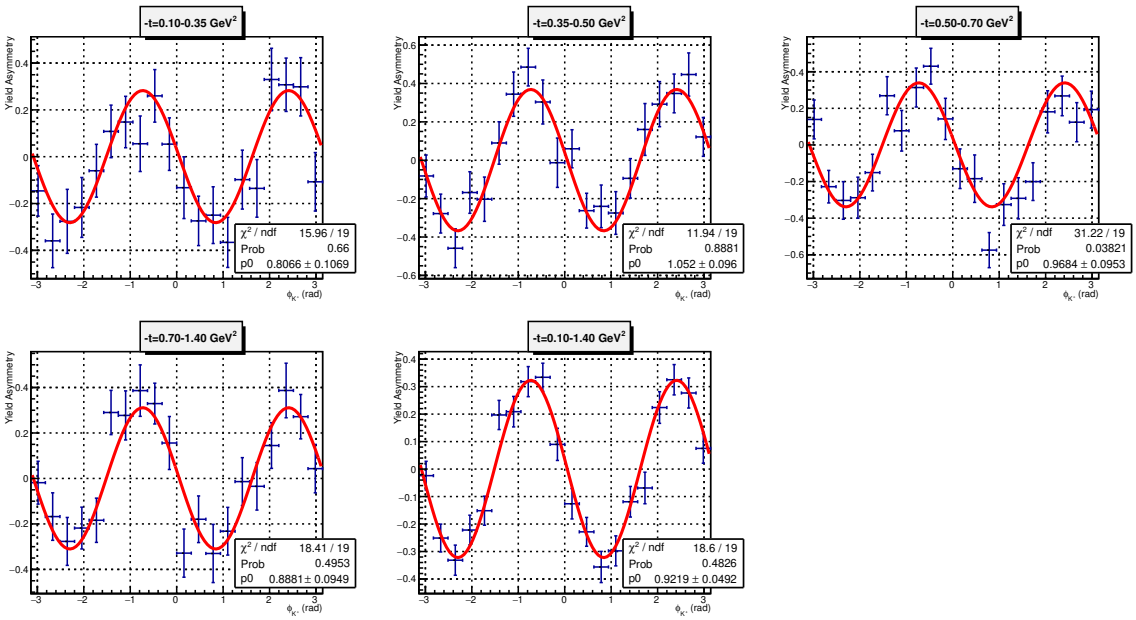

FIG. 127: Fits for yield asymmetry for -t bins for -45/45 orientation with kinematic fit confidence level $> 10^{-10}$ cut.

APPENDIX F

ACCEPTANCE OF RECOIL ANGLES

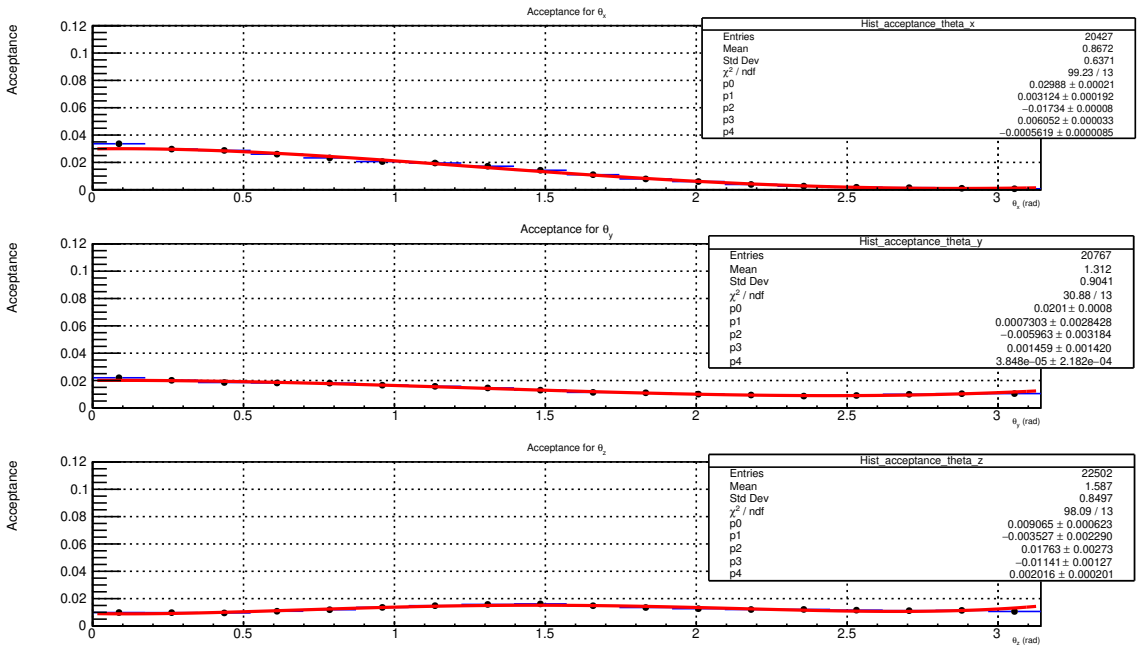

FIG. 128: Acceptance for angular distributions of the proton for 0.10 $(\mathrm{GeV}/c)^2 < -t < 0.35$ $(\mathrm{GeV}/c)^2$. Histograms are for three angles θ_x (top), θ_y (middle) and θ_z (bottom).

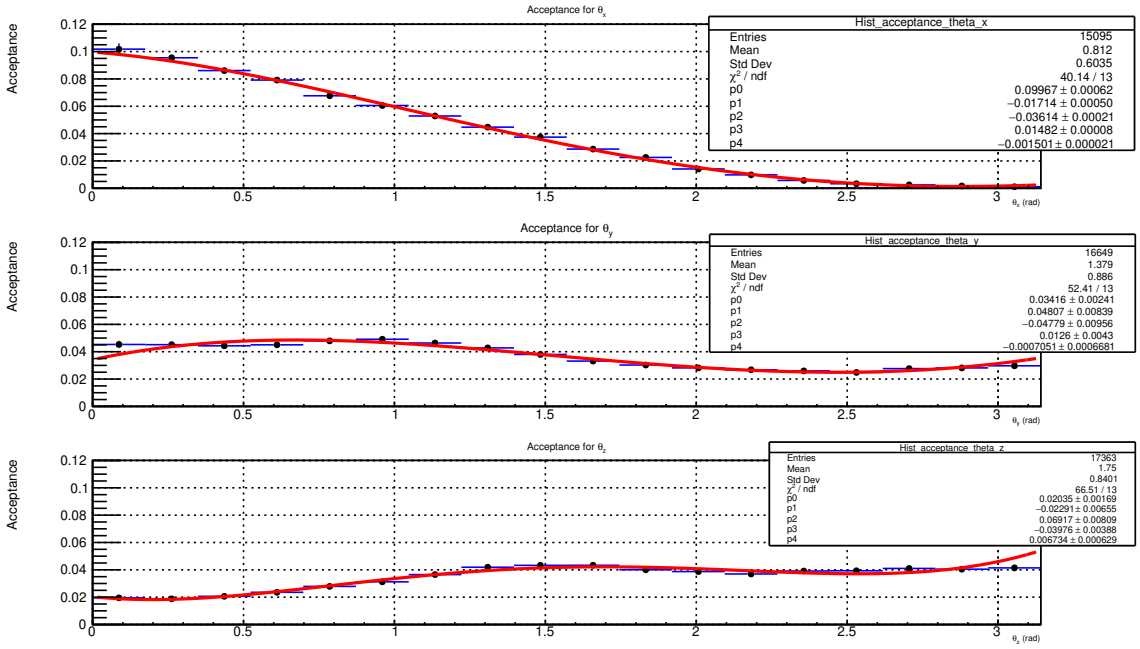

FIG. 129: Acceptance for angular distributions of the proton for 0.35 $(\mathrm{GeV}/c)^2 < -t < 0.50$ $(\mathrm{GeV}/c)^2$.

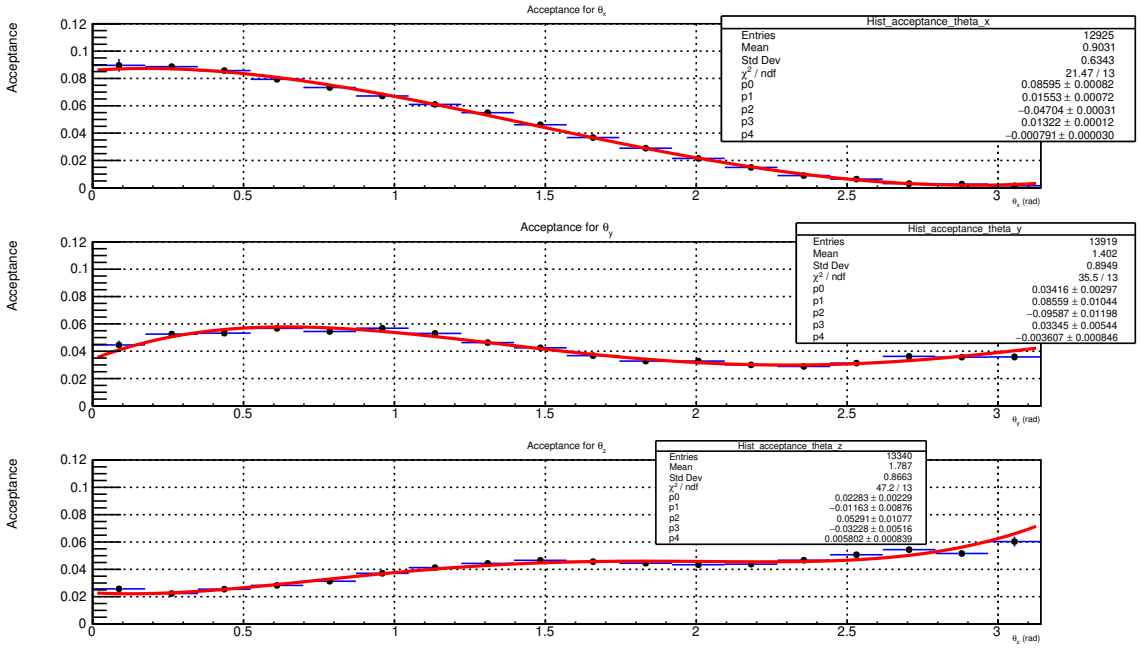

FIG. 130: Acceptance for angular distributions of the proton for 0.50 $(\mathrm{GeV}/c)^2 < -t < 0.70$ $(\mathrm{GeV}/c)^2$.

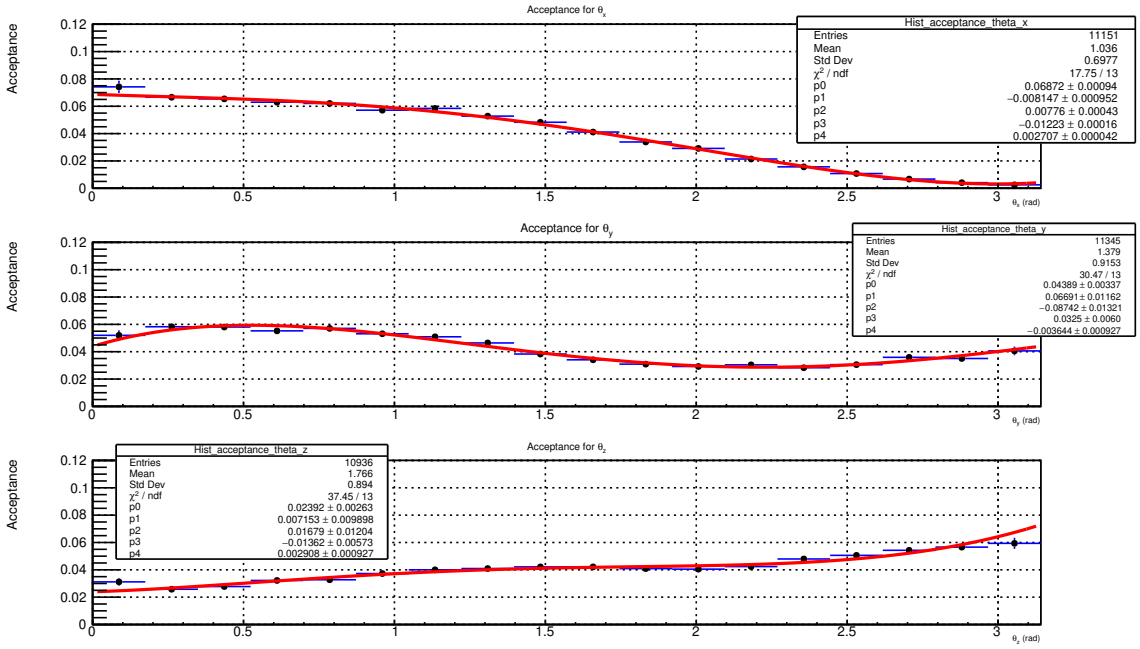

FIG. 131: Acceptance for angular distributions of the proton for 0.70 $(\mathrm{GeV}/c)^2 < -t < 1.40$ $(\mathrm{GeV}/c)^2$.

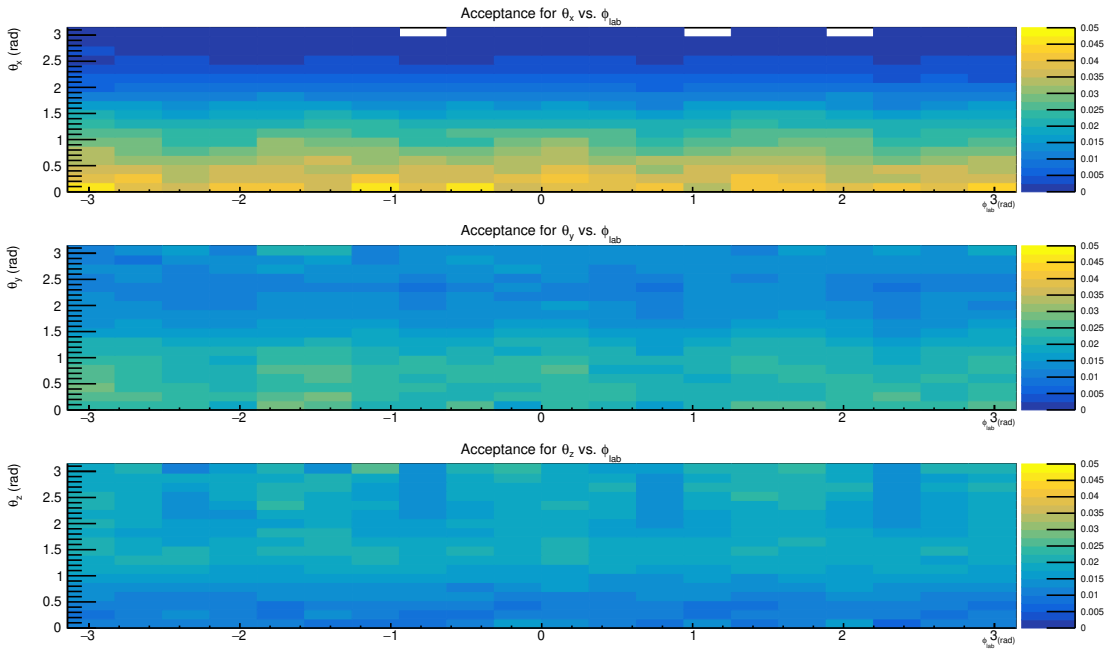

FIG. 132: Acceptances for decay angular distributions of the proton vs. ϕ lab angle of K^+ from t-channel MC.

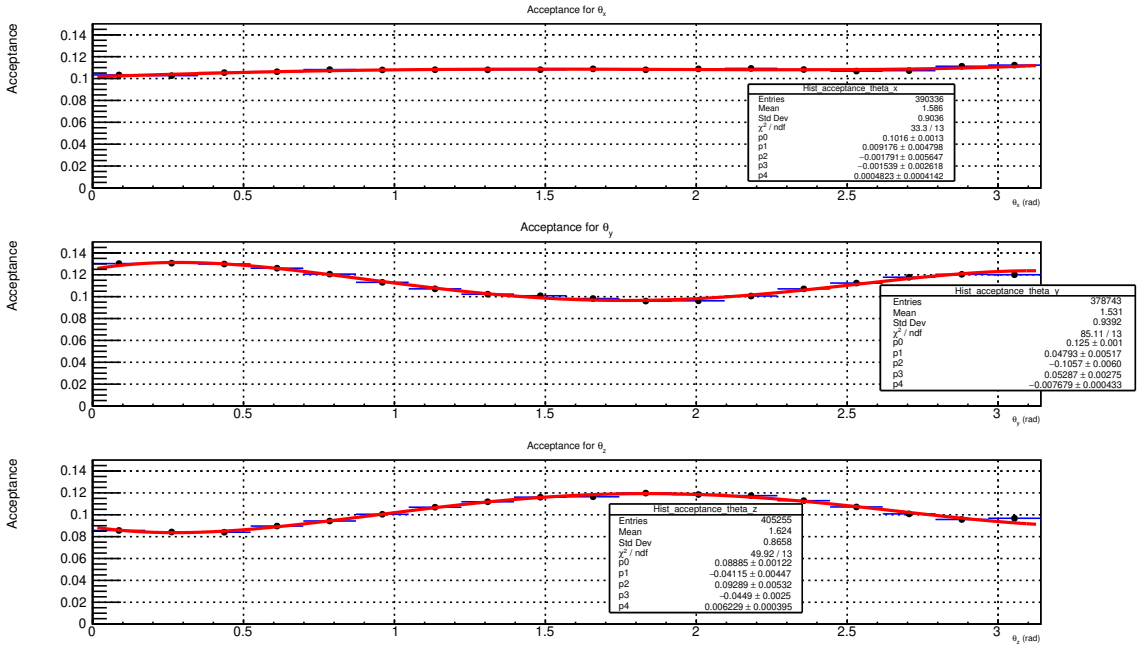

FIG. 133: Acceptance for angular distributions of the proton for $-u < 2.0$ (GeV/c)^2.

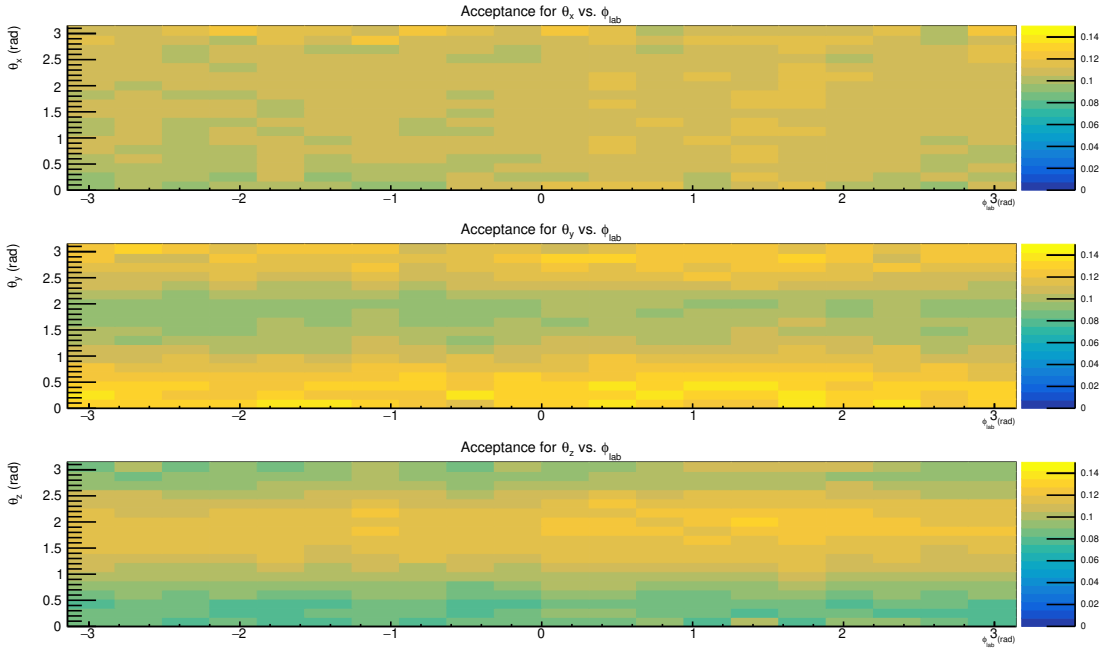

FIG. 134: Acceptances for decay angular distributions of the proton vs. ϕ lab angle of K^+ from u-channel MC.

VITA

Nilanga Indrajie Wickramaarachchi
Department of Physics
Old Dominion University
Norfolk, VA 23529

Education:

- Ph.D. in Physics, Old Dominion University, Norfolk, VA, USA, 2020
- M.S. in Physics, Old Dominion University, Norfolk, VA, USA, 2017
- B.Sc. in Physics, University of Peradeniya, Sri Lanka, 2014

Experience:

- 2017 - 2020 Research assistant, Old Dominion University
- 2015 - 2017 Teaching assistant, Old Dominion University
- 2014 Teaching assistant, University of Peradeniya, Sri Lanka

Computer skills:

- Experience with C++ programming
- Experience with ROOT and ROOFit
- Familiar with Linux and Windows

Typeset using LaTeX.